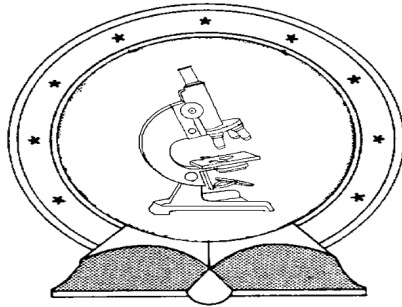


DE TTK



1949

Exploring Hot, Strongly Interacting Matter with the PHENIX Experiment at RHIC

Ph.D. THESIS

author: **Róbert Vértesi**

advisors: **Prof. Gábor Dávid, PhD.**
Prof. Tamás Csörgő, Dr.Sci.

UNIVERSITY OF DEBRECEN

Doctoral Council of Natural Sciences
D57i PhD School in Physics

Debrecen, December 31, 2010

Ezen értekezést a Debreceni Egyetem Természettudományi Doktori Tanács Fizika Doktori Iskola Részecskefizika programja keretében készítettem a Debreceni Egyetem természettudományi doktori (PhD) fokozatának elnyerése céljából.

Debrecen, 2010. december 20.

.....
(Vértesi Róbert jelölt)

Tanúsítom, hogy Vértesi Róbert doktorjelölt 2003–2008 között a fent megnevezett Doktori Iskola Részecskefizika programjának keretében irányításommal végezte munkáját. Az értekezésben foglalt eredményekhez a jelölt önálló alkotó tevékenységével meghatározóan hozzájárult. Az értekezés elfogadását javasolom.

Upton, 2010. december 20.

.....
(Dávid Gábor témavezető)

Tanúsítom, hogy Vértesi Róbert doktorjelölt 2006–2010 között a fent megnevezett Doktori Iskola Részecskefizika programjának keretében irányításommal végezte munkáját. Az értekezésben foglalt eredményekhez a jelölt önálló alkotó tevékenységével meghatározóan hozzájárult. Az értekezés elfogadását javasolom.

Budapest, 2010. december 20.

.....
(Csörgő Tamás témavezető)

Exploring Hot, Strongly Interacting Matter with the PHENIX Experiment at RHIC

Értekezés a doktori (Ph.D.) fokozat megszerzése érdekében
a fizika tudományágban

Írta: Vértesi Róbert okleveles mérnök-fizikus.

Készült a Debreceni Egyetem Fizikai tudományok doktori iskolája
(Részecskefizikai programja) keretében

Témavezetők: Dr. Dávid Gábor
Dr. Csörgő Tamás

A doktori szigorlati bizottság:

elnök: Dr.
tagok: Dr.
Dr.

A doktori szigorlat időpontja:

Az értekezés bírálói:

Dr.
Dr.
Dr.

A bírálóbizottság:

elnök: Dr.
tagok: Dr.
Dr.
Dr.
Dr.

Az értekezés védésének időpontja:

To my wife, Kata

Contents

1	Introduction	1
1.1	The strong force	2
1.1.1	Quantum chromodynamics	2
1.1.2	Quark matter	3
1.2	A short overview of RHIC physics	4
1.2.1	A new state of matter	4
1.2.2	A perfect fluid of quarks	8
1.2.3	sQGP – the hottest matter ever	9
1.2.4	The future of RHIC	11
2	Experiment	12
2.1	The Relativistic Heavy Ion Collider facility	12
2.1.1	The injection line	12
2.1.2	The RHIC experiments	13
2.2	The PHENIX experiment	15
2.2.1	Detectors for event characterization	16
2.2.2	Central tracking system	19
2.2.3	Particle identification detectors	20
2.2.4	The Electromagnetic Calorimeter	23
2.2.5	Data collection and processing	25
3	Reconstruction and calibration in the EMCal	28
3.1	Showers and clusters	28
3.1.1	Reconstruction	28
3.1.2	Description of the electromagnetic showers	30
3.1.3	Developments	33
3.2	Measuring the photon time of flight	34
3.2.1	Slewing (walk) effect	35
3.2.2	The photon timing offsets	38

3.2.3	Calibration results	40
4	Particle identification in the EMCal	42
4.1	Stochastic cuts	43
4.1.1	Method	43
4.1.2	Photon selection performance	44
4.1.3	Hadron selection	45
4.2	Neural network particle identification	46
4.2.1	Artificial neural networks	47
4.2.2	Photon selection results	49
4.3	Application: π^0 production	51
4.3.1	Analysis	52
4.3.2	Results	53
5	Shower simulation studies	55
5.1	Simulation verification	55
5.1.1	Method and sample	56
5.1.2	Conclusions	57
5.2	Fast hadron Monte Carlo	58
5.2.1	Model	60
5.2.2	Findings	61
5.3	Application: direct photons	63
5.3.1	Analysis	63
5.3.2	Results	65
6	Bose-Einstein correlations and PHENIX images	68
6.1	The HBT effect	68
6.1.1	The core-halo picture	69
6.1.2	Source imaging	71
6.2	Analysis of the heavy tail of particle emission in PHENIX	72
6.2.1	Hadron rescattering	72
6.2.2	Single freeze-out with THERMINATOR	74
6.3	Conclusions	77
7	A quest for the $U_A(1)$ symmetry restoration	79
7.1	The η' – a special choice	79
7.1.1	Quark model symmetries	80
7.1.2	Signatures	81
7.1.3	RHIC datasets	83
7.2	Modeling and simulation	85

7.2.1	Resonance models	88
7.3	Results	90
7.3.1	Reduction of the η' mass	90
7.3.2	The enhanced η' and η spectrum	96
7.3.3	System size, energy and centrality dependence	101
7.4	Conclusion	102
 Summary		 104
 Összegzés		 107
 Bibliography		 110
 Acronyms		 120

Chapter 1

Introduction

Mankind has always wondered what our world is made of, when and how did it come to existence, and what kind of rules govern the events that take place in it. Ancient peoples already carried out systematic investigations in order to understand the laws of the Universe. Stonehenge was most probably built for that purpose, and it needed an almost superhuman effort to build such a huge Stone Age observatory. Today's large particle accelerators can be considered as the modern Stonehenges. Many nations contribute to their creation, so that we can explore the ultimate structure of matter. These accelerators also function a bit like time machines. They take us to the early stages of the Universe when matter was extraordinary hot and dense.

The world is built up of matter, held together or driven apart by interactions. Newton introduced the concept of force, and the concept of fields was introduced by Faraday. The long-standing paradox whether light (or in general, the electromagnetic interaction between electromagnetically charged particles) is a particle or a wave, was resolved by quantum mechanics, which was later unified with special relativity (the kinematics of bodies for large velocities). In this *quantum field theory* (QFT) we describe both matter and interactions with quantum fields. Particles are elementary excitations of these fields. The main difference between particles of matter and those of interaction is that the formers carry half-integer spin (the so called *fermions*), and the latters carry integer spin (*bosons*). The Lagrangian formalism was reintroduced to QFT, and symmetry became a fundamental concept. According to Noether's theorem, any differentiable symmetry of the action corresponds to a conserved quantity. Quantum electrodynamics (QED), for

instance, has an intrinsic $U(1)$ symmetry which is associated with the conserved electric charge.

1.1 The strong force

It is the strong force that holds nuclei of atoms together. The quantum field theory of the strong force is called *quantum chromodynamics* (QCD). As far as we know, the basic elements of strongly interacting matter are the *quarks* (and the *antiquarks*, their antimatter counterparts). Experimental particle physics discovered a huge collection of particles with the help of bubble chambers from the 1950's on. It seemed that such a large number of particles, named as *hadrons*, could not all be fundamental. Wigner and Heisenberg classified the particles by charge and isospin, then Gell-Mann and Nishijima by strangeness. Gell-Mann and Ne'eman invented a kind of hadronic "periodic table" in 1961. The hadrons are sorted into multiplets by properties and masses in this *eightfold way* model. Gell-Mann and Zweig proposed in 1963 that the structure of the groups could be explained with the assumption that three flavors of fermions existed inside the hadrons: the quarks. A quark-antiquark pair is called a *meson*, while *baryons* (or antibaryons) are made of three quarks (antiquarks). In 1965 Han and Nambu, and independently Greenberg, pointed out that the Δ^{++} meson could not exist according to Pauli's exclusion principle, unless a new quantum number was introduced, which was later named the *color charge*. Thus was the QCD born.

1.1.1 Quantum chromodynamics

Color charge is the source of the strong force. It can have "red", "green" and "blue" values on the everyday analogy: Color-neutral states are composed from these three states similarly to the three basic colors that add up as white on the monitor. More mathematically, the color charge is defined as the Noether charge of the $SU(3)$ gauge symmetry. Quarks also carry electric charge, however, of non-integer values: They either have $+2/3$ or $-1/3$ part of the elementary charge. Antiquarks, with "anticolor" also exist and bear opposite electric charge.

QCD interactions are mediated by the so called *gluons* – gauge bosons that also carry color charge. This property makes QCD a non-Abelian theory, as opposed to QED, and it leads to a positive feedback

resulting in an interesting duality. At small distances (large interaction energies) the interaction between quarks is weak. This is the so called *asymptotic freedom*. At larger distances (or smaller interaction energies), however, the force gets very intense due to the cumulation of gluons, resulting in that quarks cannot go very far from each other, and they remain in color-neutral bound states instead – the *color confinement*¹. That is, quantum chromodynamics (QCD) can be described with a strongly momentum-transfer dependent, *running* coupling constant. In a simple model, hadrons can be treated as some kinds of sacks, inside of which quarks can move freely, but cannot break out.

Most QFT calculations use perturbation theory, meaning that a series expansion of interactions is done around the free solutions. In the particular case of the strong force, perturbative QCD (pQCD) calculations can be used when dealing with higher energy interactions. However, in the lower energy regime, the coupling is too strong to use this approach. In this case we are left with effective models, or numerical calculations on a discretized lattice space.

1.1.2 Quark matter

A new phase of strongly interacting matter was predicted both by early phenomenological considerations and lattice QCD calculations long time ago. In special circumstances where there is an enormous temperature and pressure, *deconfinement* would happen: hadrons would “melt up” in a large medium of interacting quarks and gluons. This supposed state of matter, first referred to as the quark–gluon plasma (QGP) by Shuryak [1], could have existed in the early stages of the universe. A schematic phase diagram of the strongly interacting matter is in Fig. 1.1.

This state of matter may be reproduced in ultra-relativistic heavy ion collisions. Finding the QGP and studying its properties are the most important goals that the large heavy ion colliders have been built for. The early states of the collisions can be studied through several experimental signatures like particle yields, spectra (momentum distributions), or particle correlations.

¹It is to be noted that color confinement is rather an experimental fact than a strict mathematical deduction.

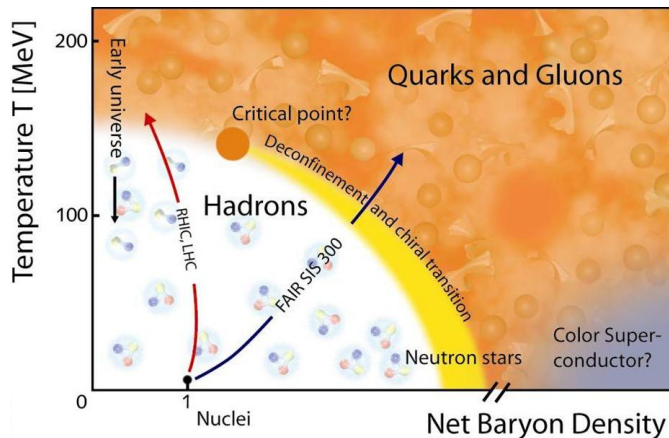


Figure 1.1. Schematic QCD phase diagram. Arrows resemble the region that is achievable for certain experiments, as well as the path the early universe has most probably followed. Net baryon density is the density baryons decreased by the density of antibaryons. Ordinary nuclei are at low temperature and low net baryon density. A phase transition is expected when going up to high temperatures or densities.

1.2 A short overview of RHIC physics

A strongly interacting matter of quarks has been found [2–5] in nucleus-nucleus collisions at the Relativistic Heavy Ion Collider (RHIC)². Initial temperature measurements have proved that this matter is a completely new phase, the strongly interacting quark–gluon plasma (sQGP) [6]. In the followings I overview the basic steps that led to this discovery, confirmed by the heavy ion measurements of the Large Hadron Collider (LHC) at the end of 2010.

1.2.1 A new state of matter

Considering asymptotic freedom, QCD problems can be solved quantitatively, using perturbation theory, when there is a large energy- and momentum transfer. In such cases we talk about *hard processes*. Partons (quarks and gluons) do not exist in free form due to color confinement. A parton that leaves the vicinity of the interaction will

²Although the focus of this thesis is on the heavy ion results, RHIC also has significant results in spin physics from polarized p+p.

fragment into hadrons before it can be directly detected, and forms a narrow cone of hadrons, called a *jet*. The original partons can only be studied through the jets measured in a particle detector. Most jets are produced in back-to-back pairs via elementary hard processes. Deconfinement implies that the QGP is more opaque for partons than a hadronic phase, causing at least one jet of most pairs to dissolve in the medium. This *jet quenching* effect is illustrated on Fig. 1.2.

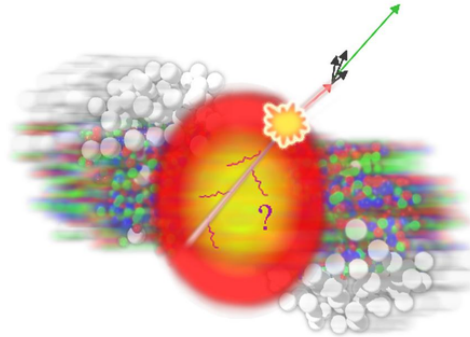


Figure 1.2. Illustration of jet quenching. A quark pair is created near the edge of the medium. The one towards the surface escapes and converts into a jet of hadrons, while the other is dissolved in the fireball.

Suppression of hadrons in heavy ion collisions

One of the first RHIC results of great importance was to observe the suppression of charged hadrons and neutral pions in central³ Au+Au collisions [7]. The PHENIX experiment measured spectra of the identified hadrons both for Au+Au collisions and for p+p collisions of the same energy. Then the p+p hadron spectra are scaled with the number of average binary (nucleon-nucleon) collisions in a Au+Au collision, N_{coll} , and the two are divided. Any deviation of this *nuclear modification factor* (R_{AA}) ratio from unity indicates a mechanism that is only

³ *Centrality* is a measure to classify heavy ion collisions. It expresses the extent to which the colliding nuclei overlap. Centrality is given in the percentage of event numbers, the smaller centrality value corresponding to the larger overlap, i.e. 0–10% centrality denoting the 10% most *central* (strongly overlapping) events, while *peripheral* (hardly overlapping) events correspond to a large, e.g. 70–92% centrality.

present in central heavy ion collisions. Generally, R_{AA} is defined as a function of transverse momentum⁴ and pseudorapidity⁵, e.g. the R_{AA} for a hadron is

$$R_{AA}^h(p_T, \eta) = \frac{1}{\langle N_{\text{coll}} \rangle} \left(\frac{d^2\sigma_{AA \rightarrow h}}{dp_T d\eta} \right) \left(\frac{d^2\sigma_{pp \rightarrow h}}{dp_T d\eta} \right)^{-1}, \quad (1.1)$$

where the σ -s are the production cross sections measured in the denoted processes⁶. Fig. 1.3 shows how the value of R_{AA} measured by PHENIX is significantly reduced from 1 to around 0.2 for both the charged and neutral hadrons in central Au+Au collisions at $\sqrt{s_{NN}} = 200$ GeV center-of-mass energy per nucleon.

The STAR experiment measured the angular correlation of the leading (most energetic) hadrons of jets at mid-rapidity. Fig. 1.4 shows that the back-to-back correlation peak is completely missing in the $\sqrt{s_{NN}} = 200$ GeV Au+Au collisions, confirming jet quenching on an event by event basis.

Absence of hadron suppression in d+Au

It is not self-evident whether the jet quenching is to be attributed to initial or final state effects. Therefore a counter-probe was initiated at RHIC with deuteron-gold collisions at the same energy. In this case the collisions showed the same binary scaling seen in peripheral Au+Au collisions [8], and no suppression was measured. This is clear evidence that the suppression is in the final state: a new state of matter is created, which is only present in high energy collisions of heavy ions, where the system has sufficient size.

⁴In mid-rapidity measurements it is common to use the transverse component of various experimental quantities. The *transverse momentum* is defined as $p_T^2 = p_x^2 + p_y^2$. *Transverse energy* and *transverse mass* can be defined too: $m_T^2 = m^2 + p_x^2 + p_y^2$ and $E_T = E \sin \theta$. Here m is the rest mass, p is the total momentum, p_x and p_y are its non-beam-direction components, θ is the polar angle, i.e. the inclination from the beam direction z .

⁵*Rapidity* is defined as $y = \text{arctanh} \frac{v}{c}$ for a velocity v , where c is the speed of light. It is the additive parameter of the Lorentz group, i.e. the rapidities corresponding to parallel velocities are simply additive. A related quantity is *pseudorapidity*, defined as $\eta = -\ln \left[\tan \left(\frac{\theta}{2} \right) \right]$. It is a commonly used spatial coordinate describing the angle of a particle relative to the beam axis. In the ultrarelativistic limit as well as in the massless limit, pseudo-rapidity equals to the rapidity.

⁶Note that most PHENIX measurements are carried out in the narrow mid-rapidity region of $|\eta| \leq 0.35$, where we integrate over rapidity.

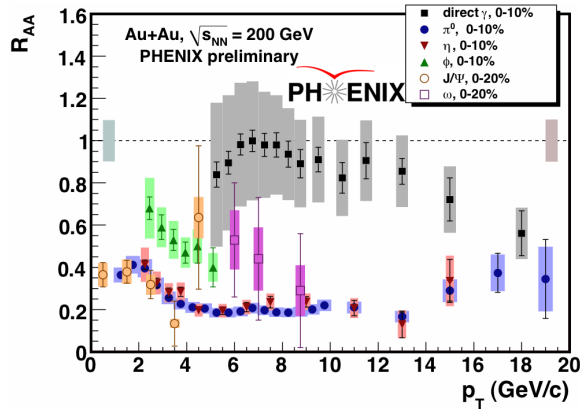


Figure 1.3. R_{AA} vs. p_T in $\sqrt{s_{NN}} = 200$ GeV central Au+Au collisions at RHIC. A suppression of neutral pions as well as of charged hadrons is clearly seen in the range relevant for pQCD, $p_T \gtrsim 4$ GeV/c. Thin error bars represent the statistical, colored bands the systematic uncertainties. Direct photons (solid black boxes) do not show suppression in the mid- p_T range.

Direct photons are not suppressed in Au+Au

While hadrons mostly carry information about the final state, quark matter is nearly transparent for the electromagnetic radiation. The production of *direct photons*, or photons arriving from sources other than hadronic decays, is sensitive to the dynamics of the early stages of the reaction. The direct photons carry information about multiple sources throughout the time development of the system, including hard processes, thermal radiation of the QGP, thermal radiation of the hadron gas present after the QCD phase transition, jet–plasma interaction, bremsstrahlung or hadron decays. The importance of direct photons is at least twofold: First, the direct photon spectrum accounts for hard processes, thus can be used as a control measurement for hadron suppression. On the other hand, thermal photons may inform us about the temperature of the quark matter itself.

The direct photon R_{AA}^γ measured by PHENIX in $\sqrt{s_{NN}} = 200$ GeV Au+Au collisions is also shown on Fig. 1.3. The spectrum is consistent with unity in the mid- p_T range, confirming that the hadron suppression

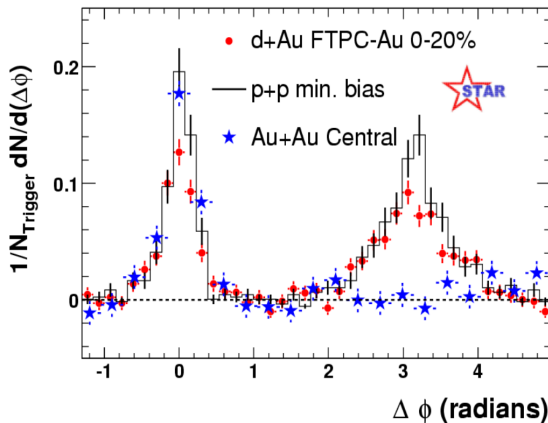


Figure 1.4. STAR $\sqrt{s_{NN}} = 200$ GeV angle correlation data of jets indicates that the suppression of the back-to-back correlation in central Au+Au is a final-state effect. While there are similar “near side” peaks (correlation of parallel jets, around 0 angle), the “away side” peak (back-to-back jets, around angle π) is completely missing in central Au+Au collisions, but present in p+p, d+Au and peripheral Au+Au collisions.

is caused by the strongly interacting matter⁷ [34].

1.2.2 A perfect fluid of quarks

The phenomenon of the jet suppression proved the existence of a new kind of matter in $\sqrt{s_{NN}} = 200$ GeV heavy ion collisions. However, it also became clear that the most important properties of this matter are only accessible via *soft processes*: processes that typically involve relatively small momenta, in which case pQCD cannot be used.

A significant observation, seen uniformly in measurements of several particle types, was the collective anisotropy, or elliptic flow, of the quark matter. The multiplicity of the particles’ bulk with lower momenta exhibits a dependency as $dN/d\phi \propto 1 + 2v_2(p_T) \cos 2\phi$ (ϕ being the angle with the *reaction plane*, defined by the (parallel) trajectories of the colliding nuclei, and v_2 being the so-called elliptic flow parameter). This is a direct hydrodynamical consequence of the elliptic shape of the nucleus overlap region during the collision, during

⁷The drop of R_{AA}^γ at high p_T is consistent with model calculations that attribute it to other reasons.

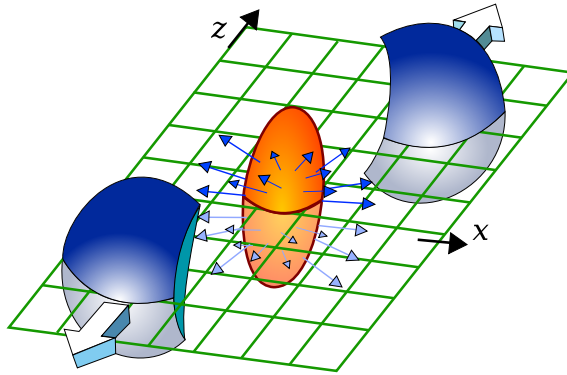


Figure 1.5. Cartoon of the elliptic flow. The pressure anisotropy of the initial state converts to momentum distribution anisotropy of the final state. The expanding ellipsoidal region of hot quark matter has a principal axis that is perpendicular to the $x - z$ reaction plane.

which the pressure-anisotropy of the initial state converts to momentum distribution anisotropy of the final state (See Fig. 1.5). This is straightforward if one assumes a strongly collective motion, or *flow*, of the created matter. This picture, however, contradicts our prior picture of a weakly interacting, gaseous QGP, and implies a strongly coupled fluid-like matter. Later measurements indicate that the viscosity over entropy ratio of this fluid is at least an order of magnitude less than that of superfluid helium, which makes it the most perfect fluid that man has ever encountered.

A stunning scaling property of the bulk matter is revealed with the measurement of the v_2 elliptic flow parameter vs. the transverse kinetic energy. Rescaled by the number of constituent quarks, all the hadrons lay on the same curve, including the Φ meson – clearly proving that we are dealing with a fluid of deconfined quarks. The quark scaling of hadron v_2 is shown on Fig. 1.6.

1.2.3 sQGP – the hottest matter ever

By 2005 the RHIC experiments found a new, dense state of matter, which is more like a liquid than a gaseous phase. However, the thermal properties of this matter had not been accessed directly. Although the observation of thermal photons in principle allows determination of the

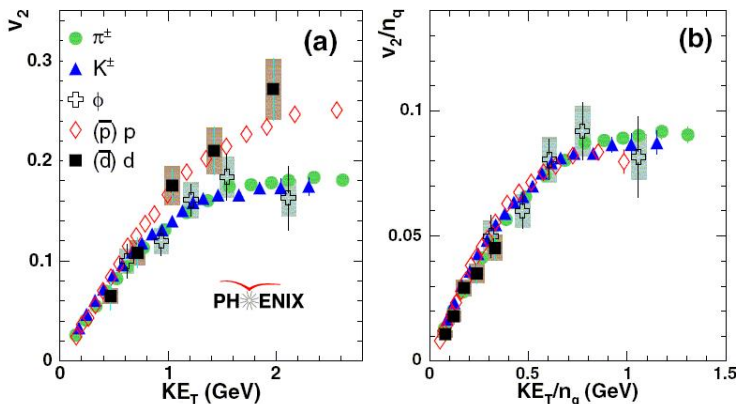


Figure 1.6. Scaling of hadron v_2 . (a) Elliptic flow parameter v_2 vs transverse kinetic energy $KE_T = m_T - m$ for several identified particle species obtained in $\sqrt{s_{NN}} = 200$ GeV RHIC Au+Au collisions. (b) The same, scaled by the number of constituent quarks n_q . Data for different types of hadrons exhibit a very good agreement.

initial temperature of the matter, the precision of low- p_T direct photon measurements is limited due to the large background from hadronic decay photons. Leptons are, however, excellent tools for studying collisions of heavy ions at ultra-relativistic energies. Since they are not affected by the strong interaction, and therefore can escape from the dense medium without final state interaction, dilepton spectra can probe the whole time evolution and dynamics of the collision. Moreover, any source of high energy photons emits virtual photons, which convert to low mass e^+e^- pairs. The virtual photon production can be related to the direct photon production, thus the direct photon yield can be reconstructed from dilepton measurements [6].

In central Au+Au collisions, the excess of the direct photon yield over the p+p is exponential in p_T , with an inverse slope $T = 221 \pm 19(stat) \pm 19(sys)$ MeV. The initial temperatures can be estimated using hydrodynamical models to fall between 300–600 MeV, corresponding to 2–4 trillion Kelvins. Considering that these temperatures are substantially higher than the Hagedorn temperature $T_H \approx 170$ MeV above which no hadronic phase is allowed, BNL announced the first observation of the strongly interacting Quark Gluon Plasma, the hottest matter ever produced, early in 2010 [11].

1.2.4 The future of RHIC

The past decade of RHIC operation has resulted in spectacular advances in our understanding of hot nuclear matter. The temperature of the sQGP, as well as investigations of the onset of several medium effects suggest that RHIC operates way above the energies of the phase transition. In the mean time LHC had its first heavy ion collisions reaching an even higher center of mass energy of $\sqrt{s_{NN}} = 3.5$ TeV. RHIC, however, still has a long way to go, since a fundamental understanding of the medium does not yet exist. A complex facility upgrade program, RHIC II has already started. It gradually implements improvements that allow RHIC to exploit its unique capabilities on several areas [9]. The low energy scan program between 5 and 50 GeV center of mass energies together with increased luminosity and detector capabilities will help us map the phase diagram in order to locate the critical point and to understand the QCD phase transition.

PHENIX found a significant excess in the dielectron invariant mass spectrum below the ρ mass when $\sqrt{s_{NN}} = 200$ GeV Au+Au collisions are compared to simulations, while in p+p collisions the models match the data. Also there is an additional thermal component with a slope of $T \sim 100$ MeV in the low- p_T part of the direct photon spectrum reconstructed from low invariant mass dilepton pairs [10]. These effects may indicate changes of the hadronic phase, such as modifications of meson properties (mass or width) in the medium, or the presence of a chiral condensate. With the newly installed Hadron Blind Detector, PHENIX has a large potential in exploring these effects.

In this thesis I present my research in the field of heavy ion physics. I detail the experimental facility in Chapter 2. Thereafter I present my studies connected to photon analyses: time of flight calibration of the PHENIX Calorimeter, photon identification for neutral pion measurements, and simulation studies for a $\sqrt{s_{NN}} = 200$ GeV direct photon analysis in Chapters 3, 4, and 5 respectively. An analysis of the heavy tails seen in PHENIX pion correlation data is detailed in Chapter 6. In Chapter 7, I report on an indirect observation of the in medium mass modification of the η' mass at RHIC, which may indicate the restoration of the $U_A(1)$ symmetry in a hot hadronic medium.

Chapter 2

Experiment

2.1 The Relativistic Heavy Ion Collider facility

The Relativistic Heavy Ion Collider (RHIC) is an accelerator of 3.8 km circumference, located in Brookhaven National Laboratory, Upton NY, USA. It is composed of two independent rings (arbitrarily denoted as "blue" and "yellow" rings) that allow for a virtually free choice of colliding projectiles from protons to gold nuclei on a wide range of energy up to 100 GeV/A in case of heavy ions and 250 GeV for protons, including strongly asymmetric setups¹. The RHIC is being continuously upgraded and it will be able to collide Uranium nuclei in the near future. Besides heavy ion physics and the investigation of quark matter, polarized protons allow spin physics to be done with the RHIC data.

2.1.1 The injection line

A particle passes through several stages of boosters before it reaches the RHIC storage ring. Heavy ion beams originate in a pulsed sputter source, and are accelerated successively by a tandem van de Graaff accelerator, the Booster Synchrotron, and the Alternating Gradient

¹Although RHIC can accelerate heavy ions in one direction and deuteron in the other at the same time, the comparable A/Z ratio, hence the similar applicable magnetic field is important in the final steering of the beam. This is the main reason why ^{197}Au projectiles are preferred over the more commonly used ^{208}Pb (and $d+^{197}\text{Au}$ collisions over $p+^{208}\text{Pb}$).

Run	Species	$\sqrt{s_{NN}}$ (GeV)	$\int Ldt$	$N_{tot} \times 10^6$	Year
01	Au + Au	130	$1 \mu\text{b}^{-1}$	10	2000
02	Au + Au	200	$1 \mu\text{b}^{-1}$	170	2001/2002
	p + p	200	0.15 pb^{-1}	3700	
03	d + Au	200	2.74 nb^{-1}	5500	2002/2003
	p + p	200	0.35 pb^{-1}	6600	
04	Au + Au	200	$241 \mu\text{b}^{-1}$	1500	2003/2004
	Au + Au	62.4	$9 \mu\text{b}^{-1}$	58	
	p + p	200	0.35 pb^{-1}	6600	
05	Cu + Cu	200	3 nb^{-1}	8600	2004/2005
	Cu + Cu	62.4	0.19 nb^{-1}	400	
	Cu + Cu	22.5	$2.7 \mu\text{b}^{-1}$	9	
	p + p	200	3.8 pb^{-1}	85000	
06	p + p	200	10.7 pb^{-1}	230000	2005/2006
	p + p	62.4	0.1 pb^{-1}	28000	
07	Au + Au	200	$813 \mu\text{b}^{-1}$	5100	2006/2007
08	d + Au	200	80 nb^{-1}	160000	2007/2008
	p + p	200	5.2 pb^{-1}	115000	
09	p + p	500	10 pb^{-1}	300000	2008/2009
	p + p	200	10.3 pb^{-1}	220000	
10	Au+Au	200	1.3 nb^{-1}	8200	2009/2010
	Au+Au	62.4	0.11 nb^{-1}	700	
	Au+Au	39	$40 \mu\text{b}^{-1}$	250	
	Au+Au	7.7	$0.26 \mu\text{b}^{-1}$	1.6	

Table 2.1. Experiment summary at RHIC. Number of events (N_{tot}) and integrated luminosity ($\int Ldt$) refers to the recorded data at PHENIX.

Synchrotron (AGS), where they reach the energy of 10.8 GeV/nucleon, fully stripped of their electrons, and injected into RHIC. Acceleration and storage in RHIC utilize two radio frequency (RF) systems, one at 28 MHz to capture AGS bunches and accelerate to top energy, the other at 197 MHz to provide a short collision diamond (of 25 cm length) for efficient utilization of luminosity by the experiments.

2.1.2 The RHIC experiments

RHIC is an intersecting storage ring particle accelerator. The RHIC double storage ring is itself hexagonally shaped and 3834 m long in cir-

cumference, with curved edges in which stored particles are deflected by 1,740 superconducting niobium-titanium magnets. The six interaction points are at the middle of the six relatively straight sections, where the two rings cross, allowing the particles to collide. The interaction points are enumerated by clock positions, with the injection point at 6 o'clock. Two interaction points are unused and left for further expansion (Fig. 2.1).

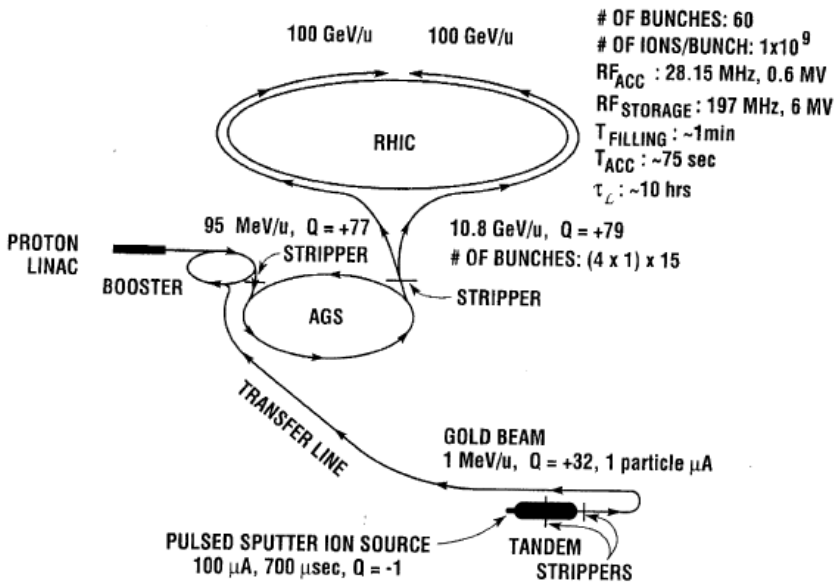


Figure 2.1. Schematic drawing of the RHIC-AGS complex.

The RHIC beams are brought into head-on collision at intersection regions. The final dipoles of the lattice are approximately 10 m from a collision diamond. Table 2.1 lists the beam species and energies for the RHIC runs to date, together with the integrated luminosity collected by PHENIX. For light ions ($A < 100$), the luminosity is limited by beam-beam hadronic interactions, whereas for heavier ions the luminosity lifetime is limited by intra-beam (intra-bunch) scattering.

The specific purpose and advantages of the dedicated RHIC experiments are listed below.

STAR

The Solenoid Tracker At RHIC (STAR) with its large acceptance Time Projection Chamber (TPC) covering the full azimuth and $|y| < 1.5$ is a multipurpose detector with focus on global event analyses, particle correlations and particle identification.

PHENIX

PHENIX is further specialized in detecting rare and electromagnetic particles than STAR, using a partial coverage detector system with an axial magnetic field. It also has a faster response time and therefore less dead time when operating on a high collision rate. Since all the topics of this work are PHENIX related, I introduce the experiment in details in Sec. 2.2.

PHOBOS

PHOBOS has the largest pseudo-rapidity coverage of all detectors, and it was equipped with subsystems to measure charge particle multiplicities over almost the entire solid angle, in addition with two magnetic spectrometers providing particle identification in a narrow aperture. The experiment completed its data taking program in 2005.

BRAHMS

The BRAHMS experiment was designed to measure charged hadrons over a wide range of rapidity and transverse momentum. It completed its data taking program in 2006.

2.2 The PHENIX experiment

PHENIX, short for Pioneering High Energy Nuclear Interaction eXperiment, is an exploratory experiment for the investigation of high energy collisions of heavy ions and protons. PHENIX is designed specifically to measure direct probes of the collisions such as electrons, muons, and photons. The primary goal of PHENIX was to discover the QGP, and it still is to study its properties. A schematic drawing of the PHENIX and its subdetectors is on Fig. 2.2. In the followings I will detail the

subsystems that are the most important for the usual analyses, including the ones detailed in this work. A detailed description of PHENIX is in Ref. [12]. The subsystems are summarized in Table 2.2.

2.2.1 Detectors for event characterization

Beam-Beam Counters

The major tasks of the Beam–Beam Counters (BBCs) [13] are to serve as a trigger for collisions at the interaction point and to provide time and vertex information of the collision. The BBC comprises two identical sets of 64 hexagonal shaped Cherenkov counters which are installed around the beam pipe at a distance of 144 cm on the north and south side of the interaction point. Measuring the time difference between the BBC North and the BBC South allows for the determination of the collision time as well as collision vertex:

$$t_{\text{BBC0}} = \frac{1}{2}(t_{\text{BBCS}} + t_{\text{BBCN}}) \quad (2.1)$$

$$z_{\text{vertex}} = \frac{c}{2}(t_{\text{BBCS}} - t_{\text{BBCN}}) \quad (2.2)$$

where t_{BBCS} and t_{BBCN} are the average arrival time of particles in the BBC South and BBC North, respectively. The time resolution of BBC is 52 ± 4 ps, corresponding to a vertex position resolution of 1.1 cm.

In p+p collisions, minimum bias (MinBias) trigger events are determined by a coincidence between north and south BBC signals, requiring at least one hit on both sides of BBCs and a collision vertex within 75 cm. In heavy ion collisions, the ZDC is also involved.

The Zero Degree Calorimeter

All four RHIC experiments are equipped with a pair of Zero Degree Calorimeters (ZDCs) [14] located at a distance of 18 m downstream of each interaction point behind the first accelerator dipole magnet. Their task is to measure the energy of spectator neutrons, which did not participate in the collision and therefore carry still a large fraction of the beam momentum. While spectator protons are charged, and therefore are deflected by the dipole magnet in front, spectator neutrons hit the ZDC and initiate a hadronic shower. Neutral particles created in the participant region of a heavy ion collision moving in

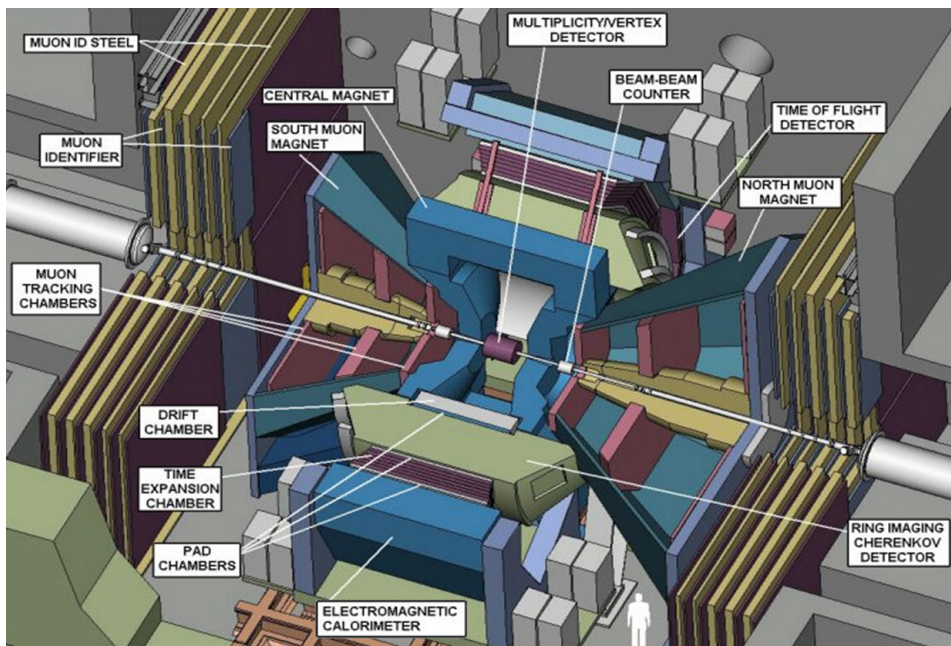


Figure 2.2. Cutaway view of the PHENIX Detector.

Component	$\Delta\eta$	$\Delta\varphi$	Purpose, special features
Central magnet (CM)	$ \eta < 0.35$	2π	Up to 1.15 Tm
Muon magnet (MMS)	-1.1 to -2.2	2π	0.72 Tm for $\eta = -2$
Muon magnet (MMN)	1.1 to 2.4	2π	0.72 Tm for $\eta = 2$
BBC	$3.0 < \eta < 3.9$	2π	start timing, fast vertex
ZDC	± 2 mrad	2π	Minimum bias trigger
DC	$ \eta < 0.35$	$2 \times \pi/2$	Good momentum resolution $\Delta p/p \approx 1\%$ at $p = 1$ GeV
PC	$ \eta < 0.35$	$2 \times \pi/2$	Pattern recognition, tracking for nonbend direction
RICH	$ \eta < 0.35$	$2 \times \pi/2$	Electron identification
TOF	$ \eta < 0.35$	$\pi/4$	Good hadron identification, $\sigma_{TOF} \sim 120$ ps
EMCal PbSc	$ \eta < 0.35$	$\pi/2 + \pi/4$	Photon and electron energy, ToF, PID
EMCal PbGl	$ \eta < 0.35$	$\pi/4$	Photon and electron energy
MUTR.South	-1.15 to -2.25	2π	Tracking for muons
MUTR.North	1.15 to 2.44	2π	
MUID.South	-1.15 to -2.25	2π	Steel absorbers and Iarocci tubes for muon/hadron separation
MUID.North	1.15 to 2.44	2π	
RxNP	$1.0 < \eta < 2.8$	2π	Good resolution for reaction plane

Table 2.2. Summary of the PHENIX detector subsystems.

forward direction typically have a much smaller energy. The ZDC is a Cherenkov sampling hadronic calorimeter made of a tungsten alloy with a conical coverage of 21 mrad around the beam direction. Its energy resolution is $\sigma_E/E = 85\%/\sqrt{E} \oplus 9.1\%$ ².

Measuring centrality

The total energy deposited by spectator neutrons can be used in anti-correlation with the total charge deposited in the BBC to determine the centrality of the collision as shown in Fig. 2.3. In addition to the centrality determination the ZDC also serves as part of the minimum bias trigger in heavy ion collisions and provides timing information, although less accurate than the BBC.

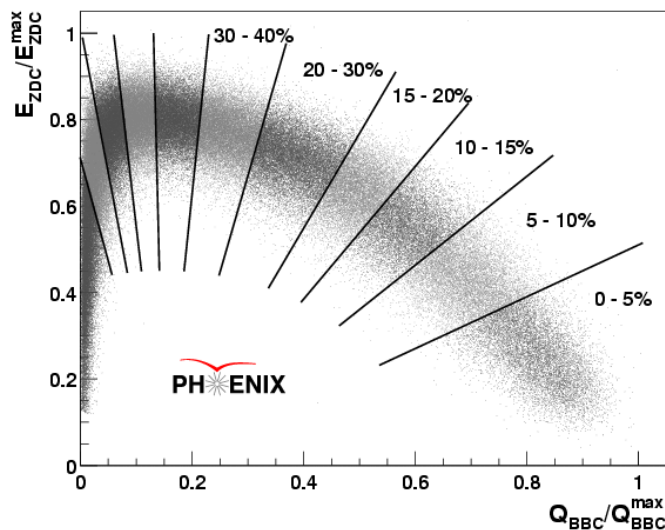


Figure 2.3. Correlation between the total energy deposited in the ZDC and the total charge measured in the BBC for Au + Au collisions at $\sqrt{s_{NN}} = 200$ GeV. The separate regions show the definition of centrality classes based on this correlation. Their boundaries are perpendicular to the centroid of the distribution.

² The \oplus sign here denotes the convolution of errors, i.e. the quadratic sum in the case of errors that can be considered independent.

2.2.2 Central tracking system

A charged particle which traverses a gas-filled detector randomly ionizes the gas. The electrons from the primary ionization process drift in an electrical field towards an anode wire after a time proportional to the distance of the track to the wire. Hits in subsequent anodes can be reconstructed to a track. PHENIX central tracking system consists of two gas detector subsystems, the Drift Chambers and the Pad Chambers.

Drift Chambers

The two Drift Chambers (DC) are multi-wire gas chambers, installed in both Central Arms as the main tracking device for charged particles in PHENIX. They are located at a distance of 2.02 m to 2.40 m from the interaction point outside the magnetic field of the Central Magnet. The DC reconstructs the curvature of charged particles in the $r - \varphi$ plane in order to determine their transverse momentum p_T .

Both chambers extend over 2 m along the beam direction corresponding to $\Delta\eta = \pm 0.35$ in pseudo-rapidity. The azimuth coverage of the chamber in the west and east central arms are $-\frac{3}{16}\pi < \varphi < \frac{5}{16}\pi$ and $\frac{11}{16}\pi < \varphi < \frac{19}{16}\pi$ respectively. The detectors are supported by a cylindrical shaped titanium frame. The active volume is confined by Mylar windows and it is filled with a gas mixture of 50% Argon and 50% Ethane. Each Drift Chamber consists of 20 identical sectors, or keystones, covering 4.5° each. Each sector contains six different wire modules stacked in radial direction. Every module contains, alternating in azimuth direction, four anode (sense) and four cathode planes. Each sense wire is split into two halves connected by a $100 \mu\text{m}$ thick Kapton insulator strip. In total the Drift Chamber contains 6500 wires read out by 13000 channels. Each DC wire has $150 \mu\text{m}$ $r - \varphi$ resolution and 1.5 mm track separation together with an efficiency better than 99%, while the spatial resolution in z direction is 2 mm.

Pad Chambers

The Pad Chambers are multi-wire cathode readout proportional chambers at mid-rapidity that cover a total area of 88 m^2 . Their main functions are to provide the track coordinate along the beam and to ensure reliable pattern recognition at very high particle multiplicity.

The electronics, mounted on the outer chamber face, together with the chamber itself amounts to 1.2% of a radiation length.

The Central Arms are equipped with three layers of Pad Chambers in the West Arm and two layers in the East Arm. The first layer of Pad Chambers (PC1) is installed just behind the Drift Chambers, while the third layer (PC3) is situated right in front of the Electromagnetic Calorimeter. The second layer of Pad Chambers (PC2) follows the Ring Imaging Cherenkov Counter in the West Arm.

Each PC contains a single layer of wires within a gas volume that is confined by two cathode planes. One cathode plane is solid copper, while the other one is segmented into a fine array of pixels. The basic unit is a pad formed by nine non-neighboring pixels, which are read out by a common channel. For a valid hit, three neighboring pads must sense the avalanche. The interleaved design allows a fine position resolution of 1.7 mm in z direction and 2.5 mm in x and y .

Track reconstruction

Associating hits in PC1 with tracks reconstructed in the DC is essential to determine the three dimensional momentum of a particle. Charged particle tracks are reconstructed in the DC based on a combinatorial Hough transform, which gives the angle of the track in the main bend plane. PC1 is used to measure the position of the hit in the longitudinal direction along the beam axis. The PC1 hit combined with the location of the collision vertex gives the polar angle of the track. In most analyses, only tracks with valid information from both DC and PC1 are used. Global tracking involves the projection of a track on the TOF and the Electromagnetic Calorimeter (EMCal), and associating with the there reconstructed hits (clusters). The flight path length is then calculated from a fit to the reconstructed track trajectory in the magnetic field.

2.2.3 Particle identification detectors

The Time of Flight detector

The TOF is located at a radial distance of 5.06 m from the interaction point in the east central arm, just in front of the PbGl sectors. This contains 960 scintillator slats oriented along the azimuthal direction. It is designed to cover $|\eta| < 0.35$ and $\Delta\phi = 45^\circ$ in azimuthal angle.

The intrinsic timing resolution is $\sigma \simeq 115$ ps, which allows for a 3σ π/K separation up to $p_T \simeq 2.5$ GeV/ c , and 3σ K/p separation up to $p_T \simeq 4$ GeV/ c .

Only a small portion of the mid-rapidity acceptance is covered by the TOF. In other regions, the Electromagnetic Calorimeter can be used for less precise time-of-flight measurements. A new TOF West detector was installed in the PHENIX west central arm before Run 5. Whereas it made only minor improvement to the acceptance, it allows for more precise flight time measurements of mid-rapidity back-to-back particles. Moreover, its improved time resolution significantly extends the p_T range where PHENIX can identify hadrons.

Charged hadron identification

Charged particle identification (PID) is performed by using the combination of three measurements: time-of-flight from the BBC and the TOF (or TOF West or EMCal), momentum from DC, and flight path length from the collision vertex point to the hit position on TOF. The square of mass is derived from the following formula,

$$m^2 = \frac{p^2}{c^2} \left[\left(\frac{t_{\text{TOF}}}{L/c} \right)^2 - 1 \right], \quad (2.3)$$

where p is the momentum, t_{TOF} is the time of flight, L is the flight path length, and c is the speed of light. The charged particle identification is performed using cuts in m^2 and momentum space. The PID cut is based on a parameterization of the measured m^2 width as a function of momentum. In Fig. 2.4, a plot of m^2 versus momentum multiplied by charge is shown together with a $2\text{-}\sigma$ standard deviation PID cut.

Ring Imaging Cherenkov Counter

A charged particle traveling in a medium with a velocity βc that is greater than the speed of light in this medium, $c_n = c/n$ for a medium with refractive index n , emits Cherenkov radiation under angle $\cos\vartheta_C = 1/(n\beta)$.

In each of the two central arms a Ring Imaging Cherenkov Counter (RICH) is installed between the inner and outer tracking detectors following the first layer of Pad Chambers [15]. Its main purpose is the separation of electrons from the large background of charged pions

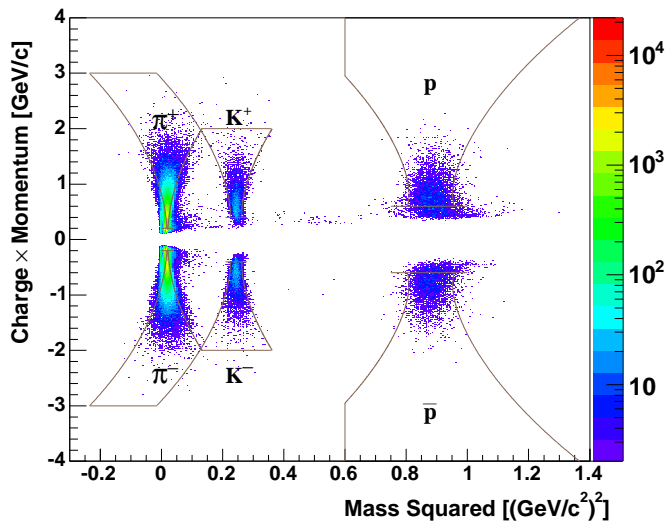


Figure 2.4. Mass squared versus momentum multiplied by charge distribution in $p + p$ collisions at $\sqrt{s} = 62.4$ GeV. The lines indicate the 2σ PID cut boundaries for pions, kaons, and protons (antiprotons) from left to right, respectively.

produced in heavy-ion collisions. In combination with the Electromagnetic Calorimeter it also provides information for an electron trigger in $p+p$ collisions. Behind the entrance window with an area of 8.9 m^2 a volume of 40 m^3 is filled with CO_2 as radiator gas, which has a refractive index of $n - 1 = 4.115 \times 10^{-3}$ [16], corresponding to a threshold velocity $\beta_t = 1/n = 0.9959$ and a Cherenkov threshold of $p_T = \frac{m_\pi \beta_t}{\sqrt{1 - \beta_t^2}} = 4.87 \text{ GeV}/c$ for charged pions ($m_\pi = 139.570 \text{ MeV}/c^2$), while electrons ($m_e = 0.511 \text{ MeV}/c^2$) exceed the Cherenkov threshold already with a momentum of $p_T = 0.018 \text{ GeV}/c$. Below the pion threshold the RICH has a hadron rejection of 104 to 1.

The Cherenkov light is focused by two intersecting spherical mirrors with a total area of 20 m^2 onto two arrays of 1280 photomultiplier tubes (PMTs) each which are located on either side of the entrance window. An average number of 10 photons per $\beta \approx 1$ particle are emitted under the angle of $\vartheta_c \approx 9 \text{ mrad}$. They are focused to a ring on the PMT array with an asymptotic radius of approximately 11.8 cm. The glass in front of the photo tube absorbs light with wave lengths below 200 nm.

2.2.4 The Electromagnetic Calorimeter

High-energy electrons and photons lose energy in matter predominantly via Bremsstrahlung, and to a somewhat less extent via e^+e^- pair production. The amount of energy loss is defined by the radiation length X_0 , the mean length of traversed matter after which an electron has lost all but $1/e$ of its energy, equaling to the $7/9$ th part of the mean free path for e^+e^- pair production by a photon. The Electromagnetic Calorimeter (EMCal) measures the energy and position of photons and electrons. Furthermore, it serves as trigger on rare events with high momentum photons. It comprises eight sectors, each covering 22.5° in azimuth and $\Delta\eta = \pm 0.35$ in pseudo-rapidity. All four sectors of the West Arm and the two top sectors in the East Arm are layered lead scintillator (PbSc) sampling calorimeters. The two bottom sectors are lead glass (PbGl) Cherenkov calorimeters, which had been used previously in the CERN experiment WA98 at the SPS.

The PbSc detector

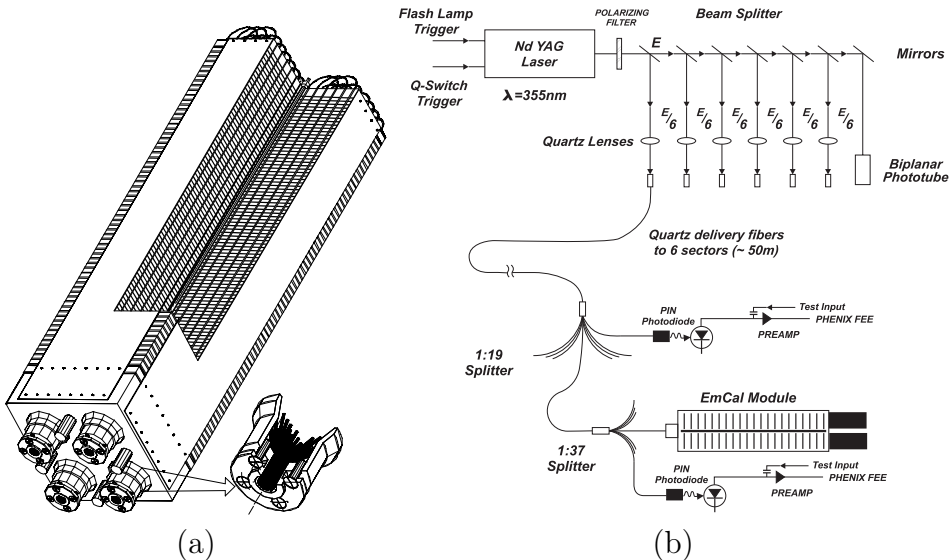


Figure 2.5. (a) Interior view of the PbSc calorimeter module showing a stack of scintillator and lead plates, wavelength shifting fiber readout, and leaky fiber inserted in central hole. (b) Laser light distribution and monitoring system.

The PbSc calorimeter contains a total of 15,552 individual towers, or basic units, which are made of 66 sampling cells with alternating layers of 1.5 mm Pb and 4 mm scintillator (1.5%PT/0.01%POPOP) [18]. A module as shown in Fig. 2.5 (a) comprises four optically isolated towers which are read out individually. Each tower has measures $5.535 \times 5.535 \text{ cm}^2$ across and has a length of 37.5 cm, which corresponds to $18X_0$. A supermodule consists of by 36 modules that are held by a common support structure, and 18 supermodules form a sector. The energy resolution of the PbSc calorimeter is

$$\frac{\sigma_E}{E} = \frac{8.1\%}{\sqrt{E}} \oplus 2.1\% . \quad (2.4)$$

The calibration and monitoring system is based on an YAG (yttrium aluminum garnet) UV laser which supplies light to the calorimeter through a series of optical splitters that distribute the light to the individual calorimeter modules. At each splitting stage, the laser intensity is monitored by PMTs at the so-called reference channels. At the last stage the light is injected into a 38 cm long, 2 mm diameter plastic fiber that penetrates the center of the module. This “leaky fiber” is grated such that light exits along its length simulating the depth profile of a 1 GeV electromagnetic shower in the four surrounding towers. The structure of the PbSc laser monitoring and calibration system is shown on Fig. 2.5 (b).

The PbGl detector

In contrary to the sampling PbSc calorimeter, the PbGl detects the electromagnetic showers via Cherenkov light radiated by the shower electrons. The PbGl sectors consists of 192 supermodules (SM) each, the latter containing 24 modules as shown in Fig. 2.6. The modules are $4 \times 4 \text{ cm}^2$ across, with a depth of 40 cm, corresponding to 14.3 radiation lengths. The refractive index of PbGl is $n = 1.648$. The readout is done by a photomultiplier at its end. The energy resolution of the PbGl calorimeter is

$$\frac{\sigma_E}{E} = \frac{5.9\%}{\sqrt{E}} \oplus 0.76\% . \quad (2.5)$$

Each lead-glass supermodule has its own gain monitoring system based on a set of 3 LED’s. The light from the LED’s are refracted by

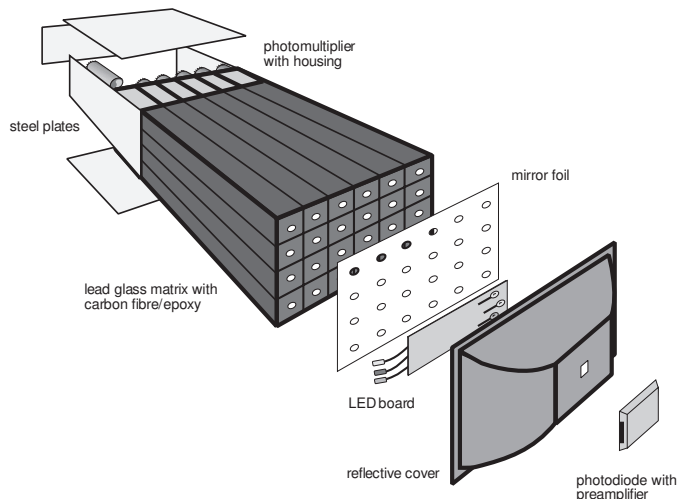


Figure 2.6. Exploded view of a PbGl detector supermodule.

a dome and detected at the same time by all 24 lead-glass modules within the supermodule.

The EMCal-RICH Trigger

The EMCal serves as Level-1 trigger for events with high momentum photons, triggering when the energy deposited in an area of 4×4 overlapping towers surpasses a defined threshold. In addition the energy in an area of 2×2 overlapping towers can be used in coincidence with the RICH trigger to trigger on events with electron candidates. This is called the EMCal-RICH Trigger (or the ERT for short).

2.2.5 Data collection and processing

Data collection and processing in PHENIX consists of several steps, divided into two main parts. The way of raw data out of the detectors, through preprocessing, trigger selection to the storage system is called *online computing*, while the *offline computing* is responsible for the storage, retrieval and processing of all event data as they are received from the online data acquisition system.

Data acquisition

A detected collision is called an *event*. The subdetectors measure the event properties, and the signals read out from the front-end electronics (FEM's) are processed by a following chain of electronics and computing.

When RHIC accelerates heavy ions, bunch crossings occur at a frequency of 9.6 MHz, while collisions occur at about 10kHz. The *trigger system* uses simple information to identify, in real time, the interesting physics events which are to retain for detailed analysis. There are two trigger levels in PHENIX. The Level-1 trigger is more hardware-oriented, based on detector electronics. The MinBias and the ERT triggers are described in sections 2.2.1 and 2.2.4 respectively. Other triggers include the muon trigger (by the muon arms) and the high- p_T trigger which fires (accepts the event) when there is a high momentum leading particle.

Once a trigger fires, the data gets assembled by the *event builder* system. A software based Level-2 trigger looks for special physics. PHENIX has the remarkably high MinBias trigger rate of 5 kHz, corresponding to a 350 MByte/s data throughput.

The basic unit of data, called a *run*, holds events collected usually within 1/2 to 1 hour. It is assumed that detector conditions do not change during a run. One run can consist of several million events. A data taking year between two maintenance periods is often called a *Run* (note the capital 'R').

Monitoring and calibration

The process of data taking is supervised by shift personnel, whose task, among others, is to monitor the status of each subsystem, the process of data acquisition as well as to verify the quality of the collected data. The primary calibrations are carried out regularly on each subsystem, using either the newly collected physics data (as for the TOF), or dedicated cosmic events (as for the MuID). Many calibrations, however, can be done only later, either on raw, or on reconstructed data. The latter is called *recalibration*. The calibration results are stored as a set of constants in a unified PHENIX database.

Storage and production

Events are stored in different files according to which trigger fired. During data taking, raw data are continuously saved to the High Performance Storage System (HPSS) that is capable of storing large amounts of data with a relatively high write and access speed. Having the most important calibrations ready (out of those that are usually done on raw data, either on- or off-line), the data is *reconstructed*: physical quantities such as charged particle tracks (Sec. 2.2.2), flight times and masses (Sec. 2.2.3) or calorimeter clusters (Sec. 3.1) are computed and stored in specific objects. The reconstructed data are then saved in data storage files, and go back to the HPSS. This process is called the data *production*. Productions are always tagged (numbered) together with the whole software environment used for the same particular production. This is important so that reconstructed data is reproducible.

Recalibration and analysis. Trains and taxis

Some calibrations cannot be done after production. These include, for example, Drift Chamber drift velocity, since keeping the individual hits would cost an unacceptable amount of storage space. Other calibrations, like the time of flight (ToF) calibration of the EMCal, are left for post production, because only when the full body of data is available can we get the constants tuned to their optimum. Some constants fall in-between, meaning that they need to be good to a minimum standard, but not absolutely final. Examples of the last category are alignment and EMCal gains.

Data is analyzed in a ROOT [19] based framework that handles all the I/O, (re)calibration, database access, quality data selection, and data processing. It consists of module prototypes for each purpose with a set of standard methods. The user needs to compose their own module for specific analyses.

The *Analysis Train*, or Analysis Taxi, is a method for running multiple analysis code on the same set of data so that it needs to be accessed only once. Data input requests are organized and directed to worker computers that have access to the particular file, including downloading the data from HPSS to disks if needed. This method allows for the most efficient use of PHENIX resources since I/O is minimized. A general selection of good quality runs (with certain selection criteria) is also performed.

Chapter 3

Reconstruction and calibration in the EMCal

In this section I describe the chain of EMCal data reconstruction code, from raw to reconstructed, calibrated data. In the first part I detail the process of going from raw front-end electronics module (FEM) packets to reconstructed EMCal clusters, followed by the introduction of the time of flight calibration in the EMCal. A detailed documentation of the PHENIX Electromagnetic Calorimeter software is in Ref. [20].

3.1 Showers and clusters

Similarly to other subsystems, the reconstruction of EMCal data is driven by a standard analysis module that is called automatically by the framework. The user does not need to have special knowledge about the EMCal data reconstruction: the module is only an interface that forwards the work to one or other implementation depending on the actual data set (or simulations) to be processed.

3.1.1 Reconstruction

Raw data comes in packets: a series of data readout, with analog-digital converter (ADC) and time-digital converter (TDC) levels for each channel. This is a very simple way of storing data, but it is ineffective at the same time, and it is a waste of I/O and CPU time to access it and convert the voltage levels into physical quantities. Therefore we convert (reconstruct) data to higher level, less resource-needy

format. The EMCal reconstruction is conceptually a two-step process: In the *phase of applying the calibrations* the raw packets are converted into calibrated tower-level information, then the adjacent groups of calibrated towers are grouped together in the *clustering phase*. The first step is more online-oriented than the second, meaning that the corresponding code is a more low level one than the clustering code. For instance in the calibration code one has to deal with FEM's and FEM channels, while the clustering works on the level of towers. Both steps make use of various databases to retrieve information (for instance the values of the gains in the calibration phase, or the geometry for the clustering phase). The two phases are realized by two independent submodules called in order by the reconstruction module. In case of simulation there can be an additional submodule for *embedding* a simulated event into an underlying event of real data. These elements of the reconstruction are briefly described below.

Applying the calibrations to tower-level data

The energy signal is measured in units of voltages. Then it is converted into digital signals with an ADC. In order to convert the signal levels into physical units, they need to be compared to references that correspond to known energies. The conversion units applied here are called the *gains*. Energy signals are measured parallelly in two ranges: the so called low gain has a lower accuracy but a higher energy span, while the high gain is more accurate, but saturates at higher ranges¹. The appropriate one is selected during higher level signal processing.

It is also to be noted that the signals are read out before and after the signal of a particle arrives (called the *pre* and the *post* gains), although in most cases only the difference (post-pre) is taken into account. The details of the energy calibration process are beyond the scope of this work, but they are extensively discussed in [21]. The time signal is produced by the TDC. The counts to time conversion constants are called *least counts*. Time-of-flight calibration is detailed in Sec. 3.2.

Tower information is still low-level (and large size) reconstructed

¹High gain is typically around 1.3–1.5 MeV/counts, corresponding to a saturation of the low-range signal around 1.5 to 2 GeV, while the low gain is 6–8 MeV/counts, meaning that the high-range ADC can measure energies up to above 25 GeV.

data which is not used directly in physics analyses. However, it is needed for special purposes such as detector studies and calibration.

Clusterization

Once the towers are calibrated, adjacent ones are grouped together to form *clusters*, defined as a contiguous set of towers, all above a given energy threshold. Then a number of characteristics of the resulting clusters are computed. These cluster descriptors are detailed in Sec. 3.1.2.

Reconstructed clusters occupy a considerable amount of storage space, but the low level information is needed for most photon-related analyses since the complex behavior of the calorimeter cannot be taken into account without it².

3.1.2 Description of the electromagnetic showers

The PHENIX Electromagnetic Calorimeter serves for identification of both electromagnetic particles and hadrons. This is not a trivial task, since PbSc has a nuclear interaction length $\lambda_I = 0.85$ and PbGl has $\lambda_I = 1.05$, hence only few hadrons will interact strongly and deposit a significant fraction of their energy. In contrast to electrons and photons, the energy loss of hadrons in matter occurs primarily through ionization and atomic excitations. For typical hadron momenta ($0.1 \leq p \leq 10$ GeV) most of the hadrons are minimum ionizing particles (MIPs), meaning that they deposit a well-determined amount of energy which is nearly independent of the incident momentum. Fig. 3.1 shows the energy deposit distributions for different particles and momenta. The minimum ionizing peaks of hadrons are clearly seen. In the followings I overview the shower characteristics that are reconstructed by the clustering algorithm and typically used in analyses involving the EMCal³.

²E.g. the adjacent showers produced by higher p_T decay photons tend to merge into one cluster after reconstruction. This effect may seriously affect the measurements of pion yields, and one has to understand it in order to correct for.

³Although “shower” is the actual energy deposit from a particle, and “cluster” is what we reconstruct, in this section the two words are used as synonyms unless stated otherwise.

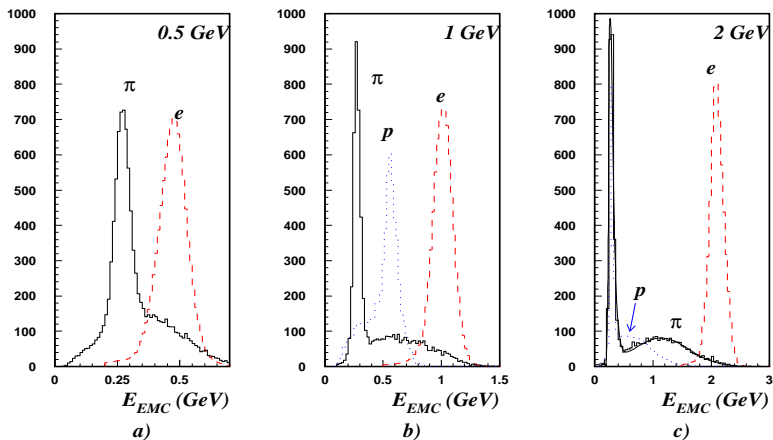


Figure 3.1. Energy spectrum measured with the PbSc calorimeter, when exposed to pions, protons and electrons for incident momenta of 0.5, 1, and 2 GeV [18]. The y-axis shows counts in arbitrary units.

Photon hypothesis test

Second moments of the measured showers are often used to differentiate between electromagnetic and hadronic showers. For each cluster the energy deposit pattern (energy in each tower included) is tested against the known energy deposit pattern of an electromagnetic shower and $\chi^2 = \sum_i \frac{(E_i^{pred} - E_i^{meas})^2}{\sigma_i^2}$ is calculated, where E_i^{meas} is the energy measured in tower i and E_i^{pred} is the predicted energy for an electromagnetic particle of total energy $E_{tot} = \sum_i E_i^{meas}$. This χ^2 value characterizes how “electromagnetic” a particular shower is⁴. The χ^2 distributions for 2 GeV/c electrons and pions (with energy deposit above the minimum ionization) are shown in Fig. 3.2. A typical cut, used in most π^0 and photon analyses to enhance photons (electrons) in a sample, is to require $\chi^2 < 3$.

⁴The deposit pattern parametrization has been established in test-beam measurements, and depends on the incident energy and the impact point. An important feature of the model is that the fluctuations are also parameterized. Therefore, the resulting χ^2 distribution is close to the theoretical one and it is nearly independent of the energy or the impact angle of the electron.

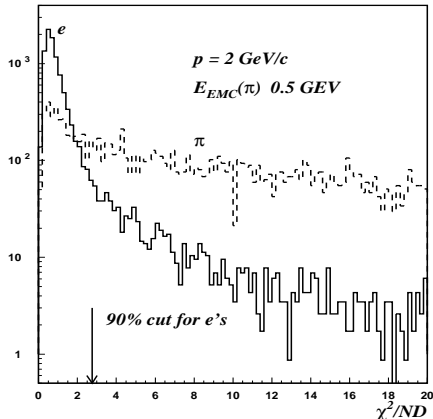


Figure 3.2. χ^2 distribution for showers induced by 2 GeV/c electrons and showering pions in PbSc calorimeter. The arrow marks the χ^2 cut corresponding to 90% electron efficiency. The y-axis shows counts in arbitrary units.

Core energy

The core energy (E_{core}) is a corrected energy of the shower under the assumption that it is electromagnetic. For each shower the expected energy deposit pattern is compared to the actual energy deposit in the towers, and those towers in which the energy differs significantly from the one based upon the “electromagnetic” hypothesis are eliminated - then the energy is re-summed⁵. This cut is intended to mitigate the effect from accidental, low-energy overlaps.

Number of towers

Cluster size is defined by the number of towers included in the cluster (N_{twr}). Electromagnetic showers are slightly more compact than hadronic showers of the same energy, and stopped baryons are considerably larger.

⁵In this step an empirical correction is applied, which is necessary since the E_{core} algorithm always reduces the energy of the cluster.

Energy in the central tower & compactness

The tower with the highest energy deposit is the central tower. The energy deposited in this tower (E_{cent}) is a measure of shower *compactness* when compared to the total energy (E_{tot}) of the cluster. On the average the ratio $E_{\text{cent}}/E_{\text{tot}}$ is smaller for hadrons than for photons and electrons.

Dispersion & eccentricity

Since the calorimeter is not projective, and charged particles are bent in the magnetic field, most particles have a non-orthogonal impact angle to the surface of the calorimeter, and the resulting clusters are elliptic rather than circular. The two values of D_0 and D_1 are the *dispersions* calculated along the major and minor axes of this ellipse respectively. The *eccentricity*, independent of size, is best quantified with D_1/D_0 .

Time of flight

Time of flight (t_{TOF}) information from the calorimeter is used both for particle identification and in the pattern recognition to find overlapping showers. In particular, timing is the main tool to reject neutral baryons, and interacting antineutrons are a major contributor to clusters up to 2 GeV. However, it is to be noted that the observed timing is not fully understood in the PbSc. The next section presents a detailed description of the time-of-flight measurements.

3.1.3 Developments

I have implemented, or contributed to, several developments to the structure of the EMCal data storage. From the Run-5 p+p period on we also store the raw ADC and, from Run-6, TDC values of the central towers of each cluster. Thus it is possible to reconstruct tower level data from the clusters, although with some loss of data. This implies that individual tower data need not be stored for the purposes of later calibration, which significantly reduces resource needs. We also reduced the storage needs by not saving all the dependent quantities of the cluster contents but calculating them on demand. In Run-7 we made changes to the data structure: MinBias data from all central

detectors are stored in a common data structure with less redundancy, and split up into clusters, central track object etc. in analysis time. High- p_T photon candidate clusters, on the other hand, are stored separately, with keeping only the relevant fields. These developments are transparent to the user, but significantly reduce storage needs.

3.2 Measuring the photon time of flight

It is often essential to reconstruct the flight time of a particle to make a good particle identification. Reconstructing the time of flight (t_{TOF}) requires precise knowledge of the behavior of most detector elements. As a first step, the measured time is compared to the time of the collision provided by the BBC. The detector response time is measured and corrected for on a channel-by-channel base. Timing offsets depend on energy, and they are not even stable in time. The timing offsets are determined so that the distribution of photon t_{TOF} values arriving from the primary vertex is zero-centered⁶. In the EMCal the t_{TOF} of a particle is usually expressed in ns, and it is reconstructed as

$$t_{\text{TOF}} = -t_{\text{BBC0}} - t_0 - \text{LC}(\text{TDC} - \text{walk}) - t_{\text{flash}} , \quad (3.1)$$

where t_0 is the sum of tower t_0 and sector t_0 values for the corresponding tower and run, determined so that the average t_{TOF} for the photons is 0 by definition (as detailed in Sec. 3.2.2). LC is the least count (calibration constant for the TDC to ns conversion units), TDC is baseline-subtracted, walk is the correction factor for the ADC dependency of the TDC value (slewing), t_{BBC0} is the time of the collision determined by the BBC and t_{flash} is the ideal photon flight time from the vertex to the detector (i.e. the distance in ns).

Although the t_{TOF} reconstruction principle is quite simple, dependence on other (known and unknown) issues e.g. the constantly improving other calibrations, the amount and diversity of data to be handled, and the complexity of the electromagnetic reconstruction code make t_{TOF} calibration a time-consuming task that is somewhat different for every Run and species. I have carried out Run-5 Cu+Cu, Run-6 p+p and Run-7 Au+Au photon t_{TOF} calibration. This summary is based on the more detailed Ref. [22].

⁶This arbitrary choice is practical since the photon selection cut can have the most simplistic $t_{\text{TOF}} < t_{\text{threshold}}$ form.

3.2.1 Slewing (walk) effect

Slewing, or walk, is the energy-dependent part of the measured photon flight time. It is usually expressed in terms of TDC(ADC) instead of $t_{\text{TOF}}(E)$. Slewing originates in two main reasons. One is *electronics*: in case of signals of the same shape but different energy, the discriminator level is reached at different times; the other is purely *geometrical*: hits of particles with different energies induce a shower at different depths in the tower, so that the signal reaches the PMT at different times. There can also be other, unresolved reasons.

Slewing is usually assumed to follow a reverse power-law shape and is required to saturate:

$$\text{walk} = \frac{k}{(E - E_0)^\alpha}, \quad (3.2)$$

where k , E_0 and α are fit parameters. E is transformed into ADC units. The E_0 term is usually neglected for practical reasons⁷. As a matter of fact, slewing directly depends on the analog signal level, therefore it changes with the experiment setup, and it has to be determined every time a new data taking period starts. Timing calibration relies to a great extent on the slewing correction. In order to achieve a good timing, the correction has to be made for each individual channel, which requires a high number of photon hits. In the followings I describe two ways that I used to determine the slewing.

Extracting the Slewing from Laser

In the case of the PbSc detector, the standard way prior to Run-7 was to obtain the slewing coefficients with the YAG laser events. Every year at least one run has been taken while there are no collisions, while the laser fires with varied intensity of its whole range, simulating photon hits with different energies and so generating ADC and corresponding TDC levels. Extracting the slewing from laser events has significant flaws:

⁷ It is crucial to find a function form that can be responsibly fitted on the vast majority of the towers, including those that collected lower amount of statistics. Introducing any new parameter makes the fit less stable. However, statistics should be less of a problem in data from later runs, thus this may be a way of future improvement in timing measurements.

1. The signal from a laser “hit” is not necessarily similar to a real photon hit;
2. When a laser event occurs, all towers fire at the same time, which is a radically different situation for the electronics than a usual, low-multiplicity physics event;
3. The laser intensity is limited in several channels. (In some cases, the high-range ADC can go up no higher than to 300 counts, corresponding to $E \lesssim 2$ GeV energies).

However, it definitely has the huge advantage that one can collect plenty of statistics within a very short time.

For small energies, the best fit is given by a logarithmic shape, and it is used in the case of the PbGl detector. On the other hand, the log shape is less adequate for the PbSc at higher energies. Prior to Run-6, the walk definition of $walk = wk * 4000/ADC$ was used for PbSc because of its relatively simplistic form. In Run-6 I carried out statistical investigations considering many numerical forms, and we decided to use the functional form of $walk = wk * 1000/\sqrt[3]{ADC}$ that describes the lower-ADC part of the curve in an acceptable manner (Fig. 3.3).

Extracting the Slewing from Data

The main advantage of slewing from laser was an easy access to large enough statistics. Collecting similarly good statistics in real data is more problematic: The photon timing distributions are fitted in several energy bins. Since the photon spectrum falls exponentially, a huge amount of events has to be processed to collect enough photon hits even in the highest energy bins for each of the ~ 16000 channels. In case of heavy ion collisions, data of several days is needed, while in case of p+p, a significant part of the whole period. In the case of Run-7 we indeed had enough data to move from laser to data-based slewing coefficients, thus we could improve on the reliability of the t_{TOF} measurements. The algorithm that I implemented is applicable on both raw and reconstructed data, and data processing can be parallelized. The photon hits are separately recorded for each tower. The $TDC+t_{BBC0}/LC$ value is filled into a histogram (unevenly binned in the ADC value) after a loose photon selection cut. These aggregated walk

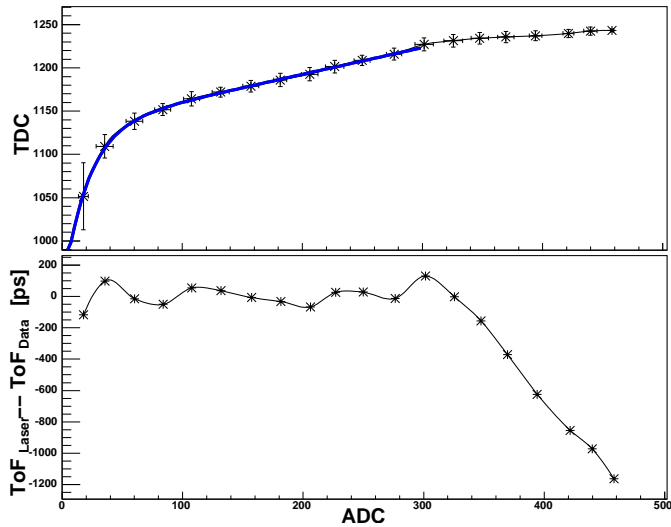


Figure 3.3. An example of slewing histograms from laser. *Top:* Black crosses are TDC vs. ADC for laser hits. The fitted walk curves (blue) are of the shape of $c_0 + wk * 1000 / \sqrt[3]{ADC}$. *Bottom:* Difference of the laser hits and the fitted curve in the units of ps. The fit is limited to $ADC < 300$, since there are no laser hits in the higher range for many towers (not like here). It is obvious that the extrapolation is problematic.

histograms are normalized with the number of hits in each bin, and the $TDC + t_{BBC0}/LC$ vs. ADC (walk) curve of the assumed shape is fitted with only one walk parameter (not counting the overall time shift, which is incorporated in the t_0). In some channels a reliable fit is not possible due to the lack of statistics. The contribution of these towers to the acceptance and statistics are, however, still valuable when the EMCal is involved in a physics analysis. Therefore, instead of marking these towers as bad towers, the corresponding walk parameters are set to the computed average of the walk parameter values from other towers.

Comparison and conclusions

The distribution of the slewing coefficients from the laser clearly shows a non-physical tail, while the coefficients from the data follow an approximate Gaussian distribution, proving that the walks from data are much more reliable (See Fig. 3.4 and Fig. 3.5). A comparative look at

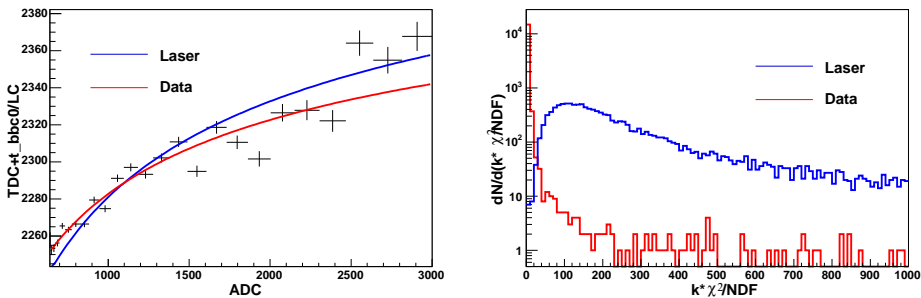


Figure 3.4. Left: An example of slewing histograms from data. (The black crosses are $TDC + t_{\text{BBC0}}/LC$ vs. ADC for selected photons. The red line is the fitted walk curve of the shape of $c_0 + wk * 1000 / \sqrt[3]{ADC}$. The blue line is the laser slewing correction determined previously for the same tower. Right: The χ^2 distribution of the laser (blue) and data (red) fits for all the PbSc towers. Note that the absolute scale of the χ^2 is arbitrary: Error bars on the measured points are computed from the number of hits in each ADC bin and do not represent propagated errors.

the timing peaks from both sets of walk in Run-7 (Fig. 3.6) suggests that, while the peak widths do not differ significantly, the data walks give us a better shaped distribution with more photons timed well. We can conclude that walks extracted from data provides us with more reliable time-of-flight measurements, and definitely this is the method that is more applicable for particle identification purposes.

Investigations of the geometrical distribution of the laser walk constants in the PbSc sectors clearly showed a spatial pattern of the erroneous laser walk constants corresponding to certain physical units of the calorimeter electronics (FEMs and ASICs). This indicates a problem of the laser distribution system, on which repairation works are not likely to be carried out, meaning that in the future we need to rely on the slewing extracted from data.

3.2.2 The photon timing offsets

As a base for a good calibration, most of the other EMCAL-measured quantities have to be calibrated for the data collection period and for the species that need to be calibrated. The actual timing values are calculated from raw ADC and TDC using the gain, least count and walk (slewing) calibration constants. Once the TDC(ADC) dependence is

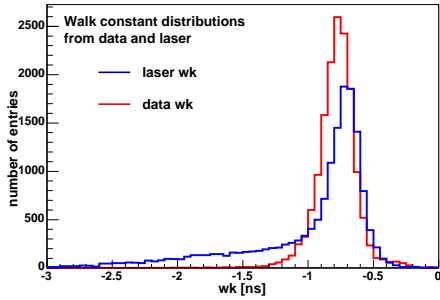


Figure 3.5. Distribution of slewing coefficients from laser (wk_{LASER} , blue) and data (wk_{DATA} , red), for all the PbSc towers.

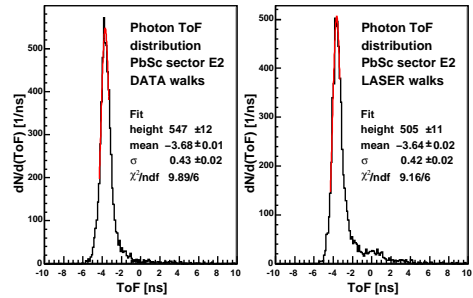


Figure 3.6. Reconstructed Run-7 ToF peaks before sector- t_0 subtraction for sector E2 with DATA (*left*) and LASER (*right*) constants for the exact same events.

known, the next step is to determine the response time of every single tower. Experience shows that, although the timing is not stable on the scale of the full data-taking period, the timing of the towers in each sector move collectively. In other words, a global correction for the towers and the correction for instability can be separated, at least within a sector.

Tower t_0 offsets

In order to compute the tower- t_0 offsets, photon hits have to be identified in each tower (25535 in PbSc and PbGl altogether), then the peak of the flight time distribution has to be fitted. On one hand, the dataset has to be collected within a short time frame since the timing is not necessarily stable on a longer term. On the other hand, enough photon hits are needed in each channel in order to carry out a good fit. In the case of high energy Au+Au collisions, these two requirements can be met with taking a long, event-rich run. However, in p+p, usually more runs are needed, even if it means a wider timing distribution.

The selection criteria for the photon candidate clusters was $\text{TDC} > 50$ and $\text{ADC} > 20$ (in terms of low gain). The t_{TOF} was computed without any t_0 correction, then the peaks were fitted with an asymmetric Gaussian of flexible range to determine the tower- t_0 constants. Noisy and bad towers were filtered out, and the result was tested in the re-

construction before I updated the final PHENIX calibration databases.

Sector t_0 tracing

Collision time signal, provided by the BBC, is synchronized with the the FEMs and the trigger electronics by the granule time modules (GTMs). The delay of the time signal depends on the actual trigger setup, and therefore it may change between runs. Hence the next step of the timing calibration is to trace the movement of the (tower- t_0 aligned) sector time peaks from run to run and to compute the so called run-by-run sector- t_0 offsets. In Run-5 Cu+Cu I determined the run-by-run sector- t_0 values offline, from reconstructed data. In Run-6 and Run-7 I carried out a preliminary timing calibration online: After I produced the tower- t_0 sets, I carried out an online calibration for each run right before the raw data files would go to the HPSS storage system. This method had the advantage that it was done before full data reconstruction, and the disadvantage that it relied on the early calibrations. The online calibration is a coarse first iteration that provided us with ~ 1 ns wide peaks. This is useful for most of the analyses, but the lower energy photon measurements required a more precise calibration later, when all the other calibrations were already settled.

Timing and walk recalibration

As a replacement for several previous EMCal t_{TOF} recalibrator classes from Run-7 on, I wrote a unified recalibrator module based on the standard calibration methods overviewed above. The recalibrator is automatically invoked for those Run-7 analyses which require recalibration. The time of flight is recomputed using Eq. 3.1, and then the new value is passed to the later analysis modules instead of the t_{TOF} value that was read from the data file. The Run-7 final timing uses this recalibrator as an *afterburner*, i.e. the preliminary calibrations are taken as a base to start from, and the t_{TOF} values are adjusted with the difference of the new and the old corrections.

3.2.3 Calibration results

The theoretical t_{TOF} resolution of ≈ 550 ns of the PbGl electronics can be reached with the calibrations. However, the ~ 150 ns resolu-

tion measured with test beams on individual PbSc channels, has never been approximated. The periods with the best resolutions, measuring around 400 ps, were reached in gold-gold collisions. In Run-5 Cu+Cu a somewhat larger resolution could be achieved. For Run-6 p+p I applied an online calibration that provided us with about 550 – 600 ns for the PbGl, however, only 800 – 1000 ns for the PbSc because of laser problems that were discovered only later. Run-5 and Run-6 p+p final calibrations were implemented by others as a separate recalibrator. In Run-7 Au+Au I carried out a preliminary calibration with the tower t_0 sets using a laser run, and online sector-by-sector calibration. Thus I was able to achieve a significantly improved timing resolution and reliability. The results are summarized year by year in Table 3.1.

Year/Species	PbSc Δt (ns)	PbGl Δt (ns)
Run-1 Au+Au	≈ 700	550 – 600
Run-4 Au+Au	350 – 450	550 – 600
Run-5 Cu+Cu	500 – 600	550 – 600
Run-5-6 p+p	≈ 800 (recalibrator)	550 – 600
Run-7 Au+Au	400 – 500 (single run offline)	550 – 600

Table 3.1. Resolutions for different periods of operation.

Chapter 4

Particle identification in the EMCal

Selection of events or particles based on probability is a recurring task in high energy physics, and it is essential that this task be solved efficiently. There might be a couple of physical (kinematical and other) quantities that indicate whether our candidate is “signal” or “background”. One often considers these quantities as probability variables that are assumed to have some kind of bell-shape or falling distribution around some “ideal” signal. The usually applied cut-based methods require these variables to remain within the boundaries of certain thresholds. This can be considered as a selection of a multi-dimensional cube around the ideal point in the space of these quantities¹, and the rejection of the rest of this space. Likelihood methods select the multi-dimensional unit sphere, and therefore they are the perfect solutions for Gaussian, or otherwise symmetric and identical distributions of uncorrelated probability variables. In reality, however, the quantities are usually correlated up to a certain degree. When the correlations are strong, and the type of the distributions are unknown and irregular, the usual approach can be extremely inefficient.

In PHENIX the default cut (used in most analyses) to identify photons is the $\chi^2 < 3$ cut described in Sec. 3.1.2. The χ^2 cut, however, is not very efficient in discriminating between photons and hadrons (Fig. 3.2). Although in case of the PbSc calorimeter the time-of-flight was expected to be another powerful tool to reject hadrons along with part of the background from off-vertex photons, the design resolution

¹Supposing that the variables are appropriately transformed and normalized.

was never reached in practice (as detailed in Sec. 3.2).

In this chapter I will show two methods for particle identification (PID) that proved to be significantly more efficient than the ones used before. Both are based on the *fuzzy logic* idea: there is no such thing as passing or failing a cut, but passing it up to a certain level. The idea is realized with combining the different variables into a discriminative function, on which a single cut is made. In this sense these methods are similar to a likelihood cut – however, the way of composing this function mentioned above is nontrivial. The last section of this chapter overviews the PHENIX Run-4 π^0 measurement as an application.

4.1 Stochastic cuts

I established stochastic cuts for selection of photons and hadron rejection in the Pioneering High Energy Nuclear Interaction eXperiment (PHENIX) EMCal. These cuts have a high γ PID efficiency along with high hadron background rejection, which makes them more powerful tools for γ PID than the previously used χ^2 or dispersion cuts. The new cuts – extensively verified with real data, see Sec. 5.1 – proved to be useful for the Run-4 π^0 and direct photon analyses as well as other analyses involving reconstruction from photons, in reducing systematic errors mainly at lower transverse momenta.

4.1.1 Method

The basic idea behind the stochastic cuts is that we characterize the shower-shape with more than one quantity (e.g. the χ^2 , the compactness, the ellipticity of the shower, etc.). Whereas these quantities are not independent of each other, they are not perfectly correlated either. Each highlights a somewhat different aspect of the shower. A small χ^2 value is already an indication that the shower is a photon, but if in addition most of its energy is in the center, this is an even stronger indication.

To quantify this, we establish the signal over background ratio curve of the cuts on individual shower shape variables (or combinations of them) vs. the actual value of the cut, defined as $SBR(x) = \frac{N_{\text{signal}}}{N_{\text{background}}}$. Here x_i is the actual threshold value applied to the shower shape quantity, and signal/background refer to photons (electrons)/hadrons that

pass the cut, respectively. In other words the method is geared towards maximizing the cleanliness of the sample rather than towards high photon efficiency. Next each $SBR(x_i)$ curve is fitted by a function $f_i(x_i)$ up to its highest value (plateau), then it is weighted with the fraction of photons that survive the cut when it reaches its plateau. This way the overall photon efficiency still remains relatively high. In the actual analysis for each cluster we calculate the product $\prod_i f_i(x_i)$ and if it is above a certain threshold, the cluster is accepted as a photon. The cluster descriptors incorporated into $f_i(x_i)$ functions have to be selected by educated guesses, then its constants have to be tuned so that all saturate on similar ranges of x_i .

In this analysis I used Run-2 Au+Au data. The signal sample was required to fulfill the RICH electron identification signal. The background sample consisted of particles that passed a $3\text{-}\sigma$ pion cut while failed both the $2\text{-}\sigma$ kaon and proton cuts. From the several cuts I developed for stochastic photon selection, the following two (named PID2 and PID4) are used in PHENIX analyses.

$$\left(0.3 + 4e^{-\frac{E_{\text{core}}}{E_{\text{cent}}}}\right) \times (1.9 - 0.67\chi^2) > 1.4 \quad (\text{PID2})$$

$$\left(0.3 + 4e^{-\frac{E_{\text{core}}}{E_{\text{cent}}}}\right) \times \left(1.9 - 0.67\frac{\chi^2}{N_{\text{twr}}}\right) \times \left(1.0 - e^{-8\frac{D_1}{D_0}}\right) > 1.4 \quad (\text{PID4})$$

4.1.2 Photon selection performance

I illustrate the effect of these cuts (and the range of possibilities) on Figure 4.1. The horizontal scale stands for deposited energy. Since the cuts are introduced in the context of a photon analysis, the relevant quantity is the deposited energy, not only for photons, but also for hadrons that we want to reject. Both electron cuts give relatively stable efficiencies above 1 GeV, varying only slowly with energy which is advantageous in a photon analysis. Also, PID2 means a compromise where a much cleaner sample is present at the expense of lower electron efficiency, whereas PID4 provides a higher hadron contamination together with a higher electron efficiency too.

For PID2 the simulated efficiencies for different particles (e, π^+ , K^+ , p, \bar{p}) are shown on Figure 4.2 as a function of deposited energy. The figure is made using flat input p_T distributions and without smearing. It illustrates how different hadrons are rejected, but does not translate

trivially into the final PID efficiency where the distributions are influenced with detector effects: it has to be folded first with the energy deposit distributions of hadrons with given momenta.

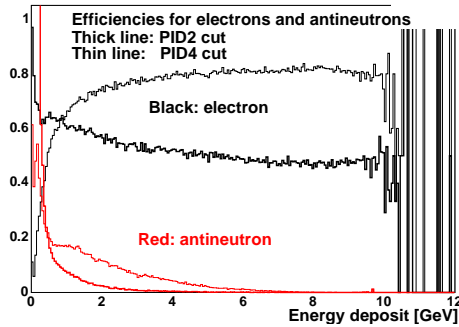


Figure 4.1. Simulated efficiencies of two stochastic cuts for electrons and antineutrons as a function of deposited energy. Thick lines: PID2, thin lines: PID4. Black curves are efficiencies for electrons, red for antineutrons.

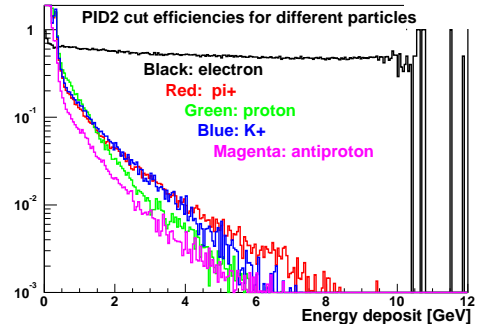


Figure 4.2. Simulated efficiencies of the PID2 stochastic cut for different particles as a function of energy actually deposited by the particle.

The stochastic cuts were systematically checked in order to test their reliability. The fact that if one starts out with raw spectra that are a factor of 10 different, still after the proper corrections the results overlap within $\sim 10\%$ gives some confidence that the effect of these cuts are reasonably well understood. Nevertheless in the low p_T region simulations were cross-checked with well-identified hadrons and electrons too (See Sec. 5.1).

4.1.3 Hadron selection

The main principle of photon selection can be reversed, and used to select hadrons as well. It is usually a less crucial question for charged hadrons, since we can use tracking information and ToF for their selection. However, an interesting side-track is to demonstrate the power of the stochastic cuts is the selection of heavier neutral particles, neutrons and antineutrons. For instance, due to their annihilation, antibaryons often produce a distinctive, “chunky” shower in the calorimeter, different from that of ordinary baryons. Time of flight measurements

can usually select baryons and antibaryons coming from the primary vertex with a relatively high momentum. However, this is not always enough: a high efficiency is needed in cases when particles emerge from decays of some exotic baryonic resonances, or, perhaps, pentaquarks (hypothetical bound states of five quarks-antiquarks). An antibaryonic stochastic cut² is compared to a combination of single-quantity cuts on Fig. 4.3 [25].

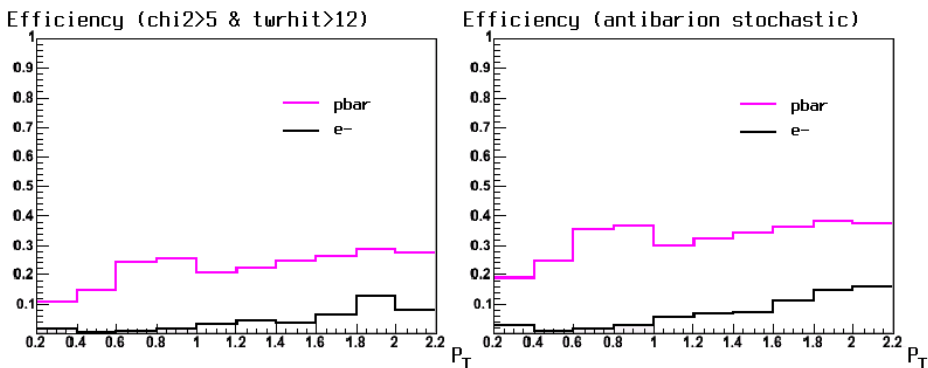


Figure 4.3. Efficiency of a “traditional” (*Left*) and a stochastic (*Right*) antibaryon cut, applied to antiprotons (magenta) and electrons (black), for illustrative purposes. The stochastic cut clearly has a larger separation power in the $p_T < 1$ GeV range.

4.2 Neural network particle identification

Although stochastic cuts exploit fuzzy logics, they have the disadvantage that they have to be (and in fact, were) tuned by hand. One may wonder whether it is possible to develop more effective cuts on the same basic principle, though with an automated, self-learning process. Artificial neural networks may be a good choice since they excel in classification, so that they are often applied in high energy physics instead of ordinary cut-based or likelihood techniques.

²Although the stochastic cuts are developed for antiprotons and not for antineutrons, it is assumed that they behave similarly. This implication, supported by simulations, is based on the universality of the energy loss processes in matter that are the most important in the discussed momentum range.

4.2.1 Artificial neural networks

An artificial neural network (ANN) is an information processing paradigm that is inspired by the way biological nervous systems, such as the brain, process information [26]. Its key element is the novel structure of the information processing system. An ANN is composed of a large number of highly interconnected processing elements (neurons) working together to solve specific problems. ANNs learn by example, just like people do. Learning is also based on the analogy with biological systems, where it involves adjustments to the synaptic connections that exist between the neurons. An ANN is configured for a specific application, such as pattern recognition or data classification, through a learning process.

Artificial Neurons

The basic computational element of an ANN is a model neuron, often called a node or unit. It receives input from some other units, or perhaps from an external source. Each input has an associated weight w , which can be modified so as to model synaptic learning. The unit computes some function f of the weighted sum of its inputs. Its output, in turn, can serve as input to other units. The function f is the unit's activation function. In the simplest case of a linear unit, f is the identity function, and the unit's output is just its net input. Another common function is the sigmoid: generally any "mild step function", a continuous function that has some finite limits in $+\infty$ and $-\infty$, and go from one to the other with exactly one inflection point. In particular, it is often represented with $f(x) = \frac{1}{1+e^{-x}}$. Neurons are interconnected with weighted links, the so called synapses. A drawing of a simple artificial neuron is on Fig. 4.4 (a).

Multilayer perceptrons

The most influential work on neural networks from the 60's is going on under the heading of "perceptrons", models of neurons with weighted inputs and with some additional, fixed, preprocessing. Perceptrons mimic the basic idea behind the mammalian visual system. They are mainly used in pattern recognition even though their capabilities extended a lot more.

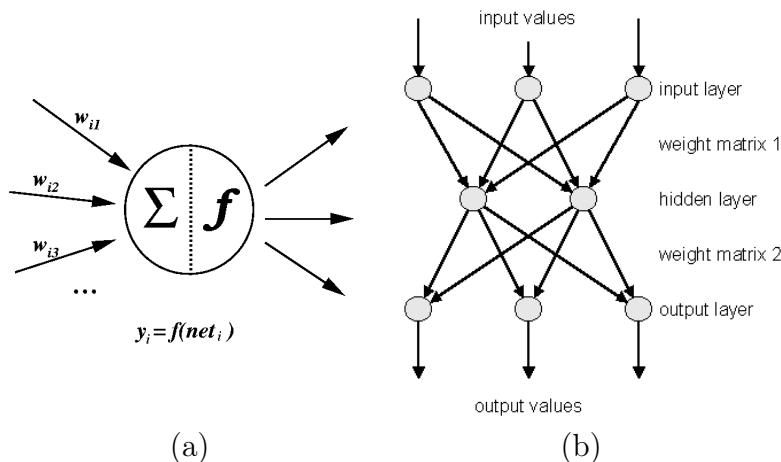


Figure 4.4. (a) An artificial neuron. The weighted sum $net_i = \sum_j w_{ij} * y_j$ is called the net input to unit i . (b) Structure of the multilayer perceptron feed-forward network.

The multilayer perceptron is a simple feed-forward network, consisting of multiple (at least three) layers: a layer of “input” units is connected to one or more layers of “hidden” units, which are connected to a layer of “output” units. This simple type of network is interesting because the hidden units are free to construct their own representations of the input. Neurons are characterized by a bias and synapses. The input neurons receive the inputs, normalize them and forward them to the first hidden layer. Each neuron in any subsequent layer first computes a linear combination of the outputs of the previous layer. The output of the neuron is then function of that combination with f being linear for output neurons or a sigmoid for hidden layers³. The basic structure of a multilayer perceptron is shown on Fig. 4.4 (b).

Learning methods

The aim of all learning methods is to minimize the total error on a set of weighted examples. The error is defined as the quadratic sum of the error on each individual output neuron. Backwards propagation

³Note that a linear combination of sigmoids can approximate any continuous function. Trained with output = 1 for the signal and 0 for the background, the approximated function of inputs X is the probability of signal, knowing X .

of errors is a supervised learning method, that requires a teacher that knows, or can calculate, the desired output for any given input. It is most useful for feed-forward networks. Back-propagation requires that the activation function used by the artificial neurons is differentiable.

4.2.2 Photon selection results

I used `TMultiLayerPerceptron` [19], a multilayer perceptron class [27] provided by the ROOT object-oriented physics analysis package. I used the stochastic minimization [28], where the weights are updated after each example according to the formula

$$w_{ij}(t+1) = w_{ij}(t) + \Delta w_{ij}(t) \quad (4.1)$$

with

$$\Delta w_{ij}(t) = -\eta(\text{de}_p/\text{dw}_{ij} + \delta) + \epsilon \Delta w_{ij}(t-1), \quad (4.2)$$

where t is the “time” indexing the steps passed, e_p is the squared deviation on a particular set of inputs, η , ϵ and δ are parameters.

The signal and background samples were the same as in Section 4.1. Different cluster variables were used as inputs. I trained the network with approximately 80000 hits for the signal and 1000000 for the background. I repeated the process with different input setups. In one setup, referred to as the “6-variable” case, basically all cluster descriptor variables were fed into the network independently: t_{TOF} , E_{cent} , E_{core} , D_1/D_0 , χ^2 , and N_{twr} . Results are shown on Fig. 4.5. In another setup (the “4-variable” case) I tried to simplify the input and made compound quantities from those that are related the most: The $E_{\text{cent}}/E_{\text{core}}$ and the χ^2/N_{twr} ratios were taken, and I kept χ^2 and t_{TOF} . I left out the t_{TOF} from the 3rd setup (the “3-variable” case), for the reasons described in 4.1. It obviously means a compromise and results in somewhat lower effectiveness, although the timing cut can be applied independently later.

As a result one will have a distribution (in principle a “photonness” probability if normalized) which is intended to use as a cut variable. The cutoff value is freely adjustable to get any efficiency one wishes. The separation power of the cut is determined by the hadron contamination left intact by the cut.

Electromagnetic particle selection efficiencies and hadron contaminations are summarized in Table 4.1. Although those are “raw” p_{T} -averaged efficiencies defined on the input samples of selected clean

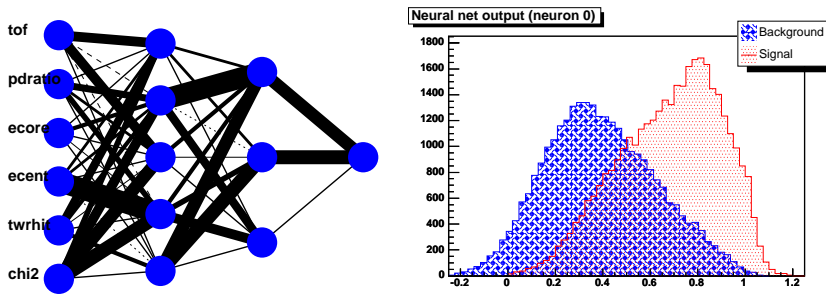


Figure 4.5. Multilayer perceptron analysis for 6 cluster shape descriptors as input variables: t_{TOF} , E_{cent} , E_{core} , D_1/D_0 , χ^2 , N_{twr} . *Left:* Structure of the perceptron network after the learning process. Line thickness represents the weight of a synapsis. *Right:* Distribution of outputs for pions (background) and for electrons (signal).

particles, they are comparable to other PID methods such as the χ^2 cut or the stochastic cuts (Fig. 4.1).

I repeated the teaching process with the same setup several times in order to test its stability. I found that, although the shape of the output distributions can vary from time to time due to the stochastic element of the process, a cut that yields the same efficiency corresponds to approximately the same contamination percentage. Cross-checks with parts of the sample were also done to prevent overtraining.

Neural network	cut on output	Efficiency	Contamination
3-variable	> 0.44	80%	52%
$E_{\text{cent}}/E_{\text{core}}$, D_1/D_0 , χ^2/N_{twr}	> 0.64	50%	24%
4-variable	> 0.46	80%	41%
t_{TOF} , $E_{\text{cent}}/E_{\text{core}}$, D_1/D_0 , χ^2/N_{twr}	> 0.66	50%	14%
6-variable	> 0.48	80%	32%
t_{TOF} , E_{cent} , E_{core} , D_1/D_0 , χ^2 , N_{twr}	> 0.70	50%	10%

Table 4.1. Electromagnetic particle selection. Hadron contaminations for MultiLayerPerceptron cuts are shown by efficiencies fixed to 50% and 80%. Note that the input samples are biased in p_T as a result of a strict PID selection of particles.

Conclusions

- It is possible to develop effective photon/hadron separation with a multilayer perceptron ANN model.
- The selective power of this ANN is higher if we feed in the different shower shape variables individually than if we use compound variables.
- Results achieved with the ANN method are neither significantly better, nor significantly worse than results from stochastic cuts.

Despite its high usability and effectiveness, an ANN cut is much more complicated than a stochastic cut, which is no more than a closed, one-line formula. Therefore the stochastic cut method is still far more transparent. There is no strong reason to give up stochastic cuts for multilayer perceptron cuts in PHENIX analysis photon selections. Anyway, the ANN analysis serves as a proof of principle for the stochastic cuts: We have one more good reason to believe that stochastic cuts are near to the optimal solutions that one can achieve in photon PID with cluster-shape analysis in the Electromagnetic Calorimeter.

4.3 Application: π^0 production

In the heavy ion collisions of RHIC, a suppression of hadrons were observed (Sec. 1.2.1). It has been shown that this suppression is a property of the final state, which suggests that a (strongly interacting) QGP is created in $\sqrt{s_{NN}} = 200$ GeV Au+Au collisions at RHIC. Since one of the most abundantly produced neutral mesons, the π^0 decays to two photons with a very high branching ratio, its production can be measured with the means of photon identification in the PHENIX Electromagnetic Calorimeter. PHENIX has shown neutral pion suppression for the first time in $\sqrt{s_{NN}} = 130$ GeV Au+Au collisions [7]. In later PHENIX measurements the experiments were repeated with different colliding systems and at different energies in order to study the onset of the effect and map the QCD phase diagram [2, 29, 30]. The analysis based on Run-2 $\sqrt{s_{NN}} = 200$ GeV Au+Au collision data is detailed in Ref. [21].

Our precision measurement of neutral pion suppression at mid-rapidity with high statistics up to $p_T < 20$ GeV in Run-4 Au+Au

collisions, using stochastic cuts for photon selection, was published in 2008 [31]. The main steps and results of this analysis will be overviewed in this section. It is to be noted that a similar stochastic cut based method was used in PHENIX to reconstruct η mesons from decay photons, where a common suppression pattern of η and π^0 was found [32]. Spectra of neutral mesons, besides their importance as physics results on their own, serve as background for direct photon measurements (Sec. 5.3).

4.3.1 Analysis

The Run-4 Au+Au neutral pion analysis has been done separately for the PbSc and the PbGl. Here I briefly summarize the PbSc analysis. The analysis in PbGl is essentially the same.

- Minimum bias and high p_T triggered events are processed from quality assured, selected runs. Events are grouped into centrality classes using the BBC and the ZDC, as described in Sec. 2.2.1. Noisy and bad towers are excluded from the analysis, as well as the ones at the edge of sectors. A cluster energy threshold of $E \equiv E_{\text{core}} > 0.2$ GeV was applied. Then the photons are selected using different PID cuts: 1) no PID, 2) $\chi^2 < 3$ and the 3) PID2 stochastic cut. Pion candidates are reconstructed by pairing photons and applying an energy asymmetry cut of $\alpha \equiv \frac{|E_1 - E_2|}{E_1 + E_2} < 0.8$ on the two paired photons.
- The raw π^0 yield in a given p_T bin is determined by mixed-event background subtraction. Photons from independent events of identical event classes are paired to give a “false” invariant mass ($m_{\gamma\gamma}$) distribution without a π^0 peak. Then this is appropriately normalized and subtracted from the actual $m_{\gamma\gamma}$ distribution. The remainder is fitted in order to determine the peak area.
- The geometrical *acceptance* is calculated by a fast Monte Carlo producing pions with a flat p_T spectrum. The (p_T -dependent) selection *efficiency* is computed by processing the simulated clusters with GEANT, and embedding the result into real event data. Then the reconstructed π^0 p_T -spectrum is divided by the simulated one to get the efficiency.

The raw results have to be corrected for several effects. With increasing π^0 momentum the effect of *cluster merging* also increases: the minimum opening angle of the two decay photons decreases, and eventually they will be reconstructed as a single cluster. Reconstructed off-vertex π^0 s, photon conversion, feed-down from K_S^0 decays also have to be taken into account. The main sources of systematic uncertainties are yield extraction, efficiency corrections, and energy scale. The hadron contamination contributes to the error on the selection efficiency, which is determined by comparing the results of the three different selection criteria. The total errors are substantially reduced when PbSc and PbGl results are combined as a weighted average.

4.3.2 Results

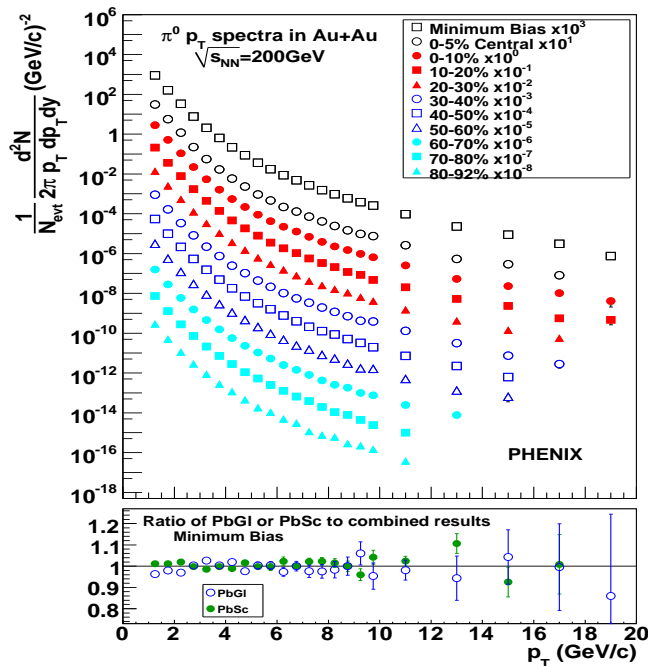


Figure 4.6. *Top:* π^0 invariant yields for different centralities (PbSc and PbGl combined) [31]. The exponents vary from 8.00 ± 0.12 in most central to 8.06 ± 0.08 in the most peripheral bin. *Bottom:* consistency between the results obtained separately from PbSc and PbGl.

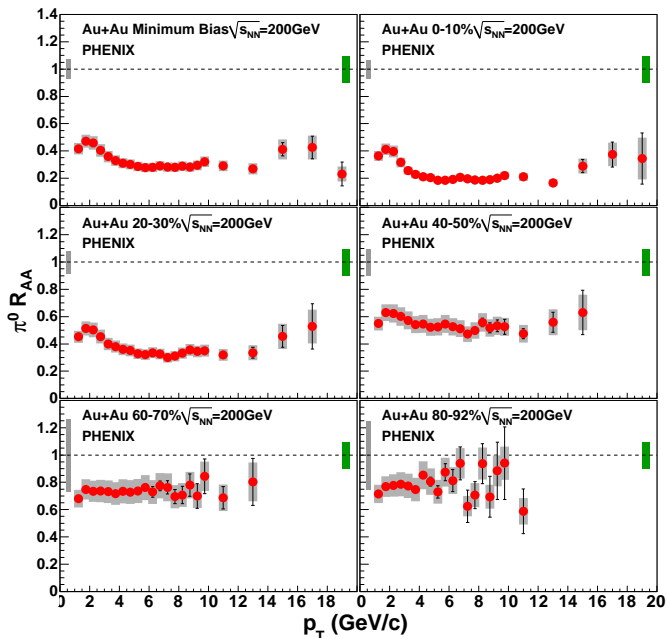


Figure 4.7. Nuclear modification factor (R_{AA}) for π^0 s [31]. Error bars are statistical and p_T -uncorrelated errors, boxes around the points indicate p_T -correlated errors. Single box around $R_{AA} = 1$ on the left is the error due to N_{coll} , whereas the single box on the right is the overall normalization error of the p+p reference spectrum.

I contributed to the determination of the p_T spectrum of π^0 invariant yield, shown in Fig. 4.6 for minimum bias as well as for the particular centrality classes. In the overlap region the results are consistent with the earlier measurements of Ref. [29], while the errors are reduced by a factor of 2–2.5. The lower panel shows the consistency of the PbSc and the PbGl measurements. The total combined error is 7%–7.6% for the $p_T < 10$ GeV region, whereas it grows to 14% for $p_T = 16$ GeV. The shape of the spectrum is similar for all centralities: the fitted exponents agree within error. Figure 4.7 shows the nuclear modification factor for π^0 at different centralities. In the case of the the most central collisions, the R_{AA} reaches ~ 0.2 at $p_T > 5$ GeV/c with very little p_T dependence. For more peripheral collisions the R_{AA} is generally higher, however, the shape is similar. It is to be noted that the R_{AA} does not saturate with centrality (Fig. 4 of Ref. [31]).

Chapter 5

Shower simulation studies

All analyses rely on simulations at least to some extent - and sometimes do so quite heavily. A typical example is particle detection and particle identification efficiency: the detector response to well-known single particles is simulated then these particles are *embedded* in real events, the event is analyzed with the normal analysis chain, using the same cuts which were applied in analysis of the actual physics events. The efficiency with which the embedded particles are identified is assumed to be the efficiency to find similar real particles in the physics event. This method assumes that the simulated response of the detector to a particle of given identity and momentum is on the average the same as the true response would be – at least for those quantities that are relevant for a particular analysis. Verification is therefore essential for the detector simulations used in hadron or photon analyses.

5.1 Simulation verification

In this study I examined how simulations match real data for different shower characteristics individually. The EMCal is used both in electromagnetic particle (photon and electron) analyses and for identification of hadrons. The deposited energy of an electromagnetic particle is equivalent to the momentum. Therefore in this case a good match of shower characteristics is needed between simulations and data at a particular deposited energy both for photon/electron identification and hadron rejection, while the true momentum of hadrons is irrelevant. Photon/electron analyses therefore need comparisons of shower characteristics as a function of deposited energy.

In hadron analyses, however, the true energy deposit of hadrons with the same momentum can differ significantly, therefore the important variable is momentum (or p_T). While the primary tool of identification (in the EMCal) is timing, often some confirmation by the shower shape is required (e.g. in the \bar{p} , \bar{n} analyses). Therefore a good match (on the average) of simulated and real shower characteristics is needed at a given momentum.

In addition to comparing shower characteristics in bins of particle momentum as well as in bins of energy a third test is needed: to compare (in bins of momentum) the total energy deposit in simulations and data. As we will see these comparisons are not always satisfactory. We attribute the differences partly to the known shortcomings of hadron simulation codes and partly to the bias introduced by the selection procedure of well-identified hadrons from data (as opposed to the simulation where all generated particles are considered). Once the energy deposit distributions of different hadrons as a function of their momentum is known, they can be folded with the hadron momentum spectra, and – based fully upon measured data – we can predict the cluster energy distribution in the calorimeter due to particles coming from the collision. In other words, both the non-vertex background and the hadron contamination of photon/electron spectra can be estimated even without any particle identification applied¹.

Finally, detailed studies of energy deposit distributions and shower characteristics provide sufficient information to attempt to parameterize hadronic showers similar to the already existing and successful parameterization of electromagnetic showers. This in turn makes a *fast hadron Monte Carlo* (Sec. 5.2) possible.

5.1.1 Method and sample

I compared the standard PHENIX GEANT simulations to selected clean hadron samples from Run-3 d+Au collisions. A clean sample of hadrons was obtained by requiring a $3\text{-}\sigma$ matching for the particular hadron types, and a $2\text{-}\sigma$ rejection for the other hadron types at the same time². Electromagnetic particles were represented by an electron sample selected by the RICH.

¹Note that results will be valid only in the p_T range where particles can actually be “well-identified” in the EMCal, which is a serious limitation

²The hadron PID cut σ boundaries are defined in Sec. 2.2.3.

A cluster is a 2-dimensional projection of the real 3-dimensional energy deposit pattern. To understand this structure I studied particles orthogonally hitting the center of the sectors separately from those that fall at the edge regions in an angle. The orthogonal samples consisted of hits with a corresponding cluster center-of-weight that was less than 20 cm away from the main vertex point along the axis direction, i.e. $|z| < 20$ cm, while a large angle impact was defined by $|z| > 160$ cm – particles being otherwise approximately uniformly distributed on the (r, ϕ) barrel. In all cases, the fiducial cut has been applied, eliminating the last 12cm around the sector edges. I analyzed the π^\pm , K^\pm , p and \bar{p} simulations w.r.t. data in 0.2 GeV energy as well as p_T bins starting from at 0.3 GeV in each case.

5.1.2 Conclusions

Three regions – minimum ionizing, partial shower containment and full shower containment – were evaluated separately, by particle types. Not only the general behavior of the shower descriptor distributions were investigated in momentum and energy bins, but the momentum and energy dependent efficiency of typical particle identification cuts were compared in simulations to data.

In the followings I recapitulate the most important findings of our simulation verification analysis, detailed in Ref. [33]. These points call attention to the areas where care should be taken when the simulation results are applied to physics analyses.

- **Simulation of the total deposited energy** is only acceptable for pions and it is worst for the important case of \bar{p} . Furthermore it is remarkable that even the minimum ionizing region is unsatisfactory for K^\pm , p , \bar{p} either because GEANT didn't get the fraction of MIPs right or because the minimum ionizing peak itself was at the wrong place. The goodness of energy deposit appears to be independent of the impact angle. The low-momentum discrepancies indicate a problem, while the description is robust at high momenta. Fig. 5.1 shows the energy distribution for antiprotons with 1 GeV/c momentum.
- **Comparison of shower descriptors** in energy binning, compactness ($E_{\text{cent}}/E_{\text{core}}$) clearly stands out in quality, and cluster size (N_{tvr}) description is the worst. Generally, pions show the

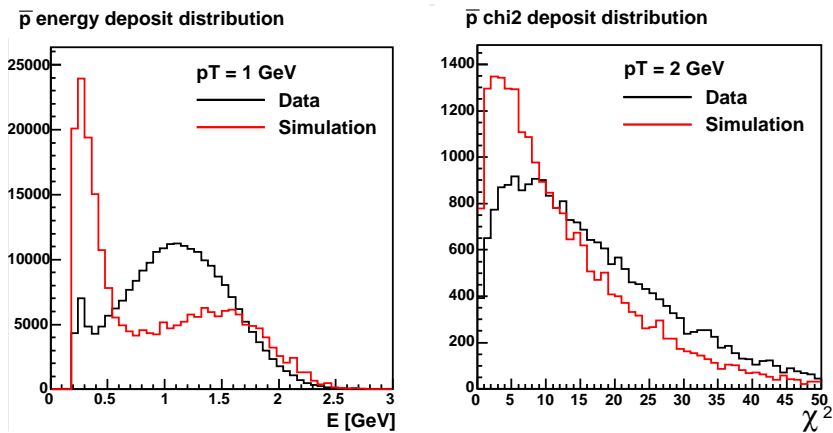


Figure 5.1. *Left:* Energy deposit of antiprotons with a momentum of 0.9 to 1.1 GeV/c. *Right:* χ^2 distribution of antiprotons deponating energy between 1.9 and 2.1 GeV. Solid (black) line is real data, light (red) line is simulation on both plots.

best agreements, kaons and protons are mediocre, while antiprotons are once again the worst. Fig. 5.1 shows a large discrepancy in the χ^2 distribution for antiprotons that deponate 2 GeV energy in the calorimeter. The picture is more balanced when we look in bins of original momentum.

- **The dependence on impact angle** leads to a counter-intuitive conclusion: Showers are somewhat better described at large impact angles than at orthogonal impact. This surprising observation is prevalent when the comparisons are made in bins of energy. It is also present in momentum binning, although to a somewhat lesser extent. Fig. 5.2 illustrates this observation on the antiproton selection efficiency of the usual $\chi^2 < 3$ photon selection cut.

5.2 Fast hadron Monte Carlo

A short detour from the main stream of this thesis is a straightforward application of the simulation verification studies – a Fast Hadron Monte Carlo code. The aim was to create a program that both runs faster than GEANT and provides a more reliable output, that could be

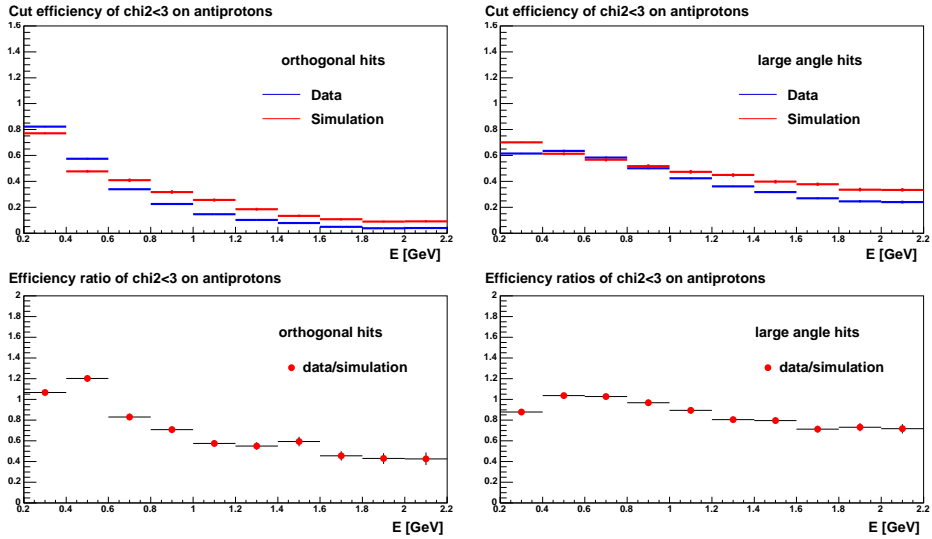


Figure 5.2. Efficiency vs. deponated energy of a $\chi^2 < 3$ cut for \bar{p} at orthogonal impact (*left*) and at large impact angles (*right*). On the upper panels, efficiencies of real data are shown as dark (blue) histograms, while the light (red) ones are simulation. The lower panels show the data to simulation efficiency ratios.

used for instance to study embedding. We supposed that the detailed studies of energy deposit distributions and shower characteristics provided sufficient information to simulate hadronic showers in the EMCal detector heuristically, using a parametric description of the hadronic showers with actual predicted energy deposits in towers. We simulated a hadron hit through the following process:

- As a first step, the energy deposit distribution for a given momentum is modeled in three dimensions.
- The energy deposit distribution is then virtually placed into the detector with the selected impact angle, and the deposit in each tower is determined. (Since the energy deposit from a hadron is usually not fully contained in the detector, only the portion inside the detector boundaries is considered.)
- Lastly, the tower by tower deposits are clusterized using the very same reconstruction algorithm that is used for real data.

5.2.1 Model

While an electromagnetic shower is well approximated with a 3D bell-shape energy distribution with uniform density, the energy deponating mechanism of hadrons is more complicated, consisting of (at least) two components: one from the electromagnetic shower started by the hadron, and the other from the actual hadron shower. The first attempt to model this duality was a sum of two Gaussian components. However, this simple picture does not reflect that many hadrons do not even start a hadronic shower in the calorimeter, and therefore the distribution of the deponated fraction of the hadron energy (or: E_{tot} vs. p_{T}) cannot be modeled correctly. It became clear that some random elements would have to be introduced. In the followings I describe two approaches of this problem.

Randomized shape simulation

This model approximates the showers with a simple geometrical shape. A relatively few number of points (five to twenty) are randomly chosen within the envelope of this shape, and the total energy is evenly distributed among them. The most refined shape that we used was the already mentioned 3D double Gaussian form (a narrow and tall one representing the electromagnetic part of the hadron shower, and a wider but shorter one representing the actual hadronic part of the showers, the latter shifted along the symmetry axis so that the baselines of the two distributions are common). Parameters of the model, apart from the incident particle mass, momentum and impact angle, are the number of points, the widths and the amplitudes of the two bell shaped distributions, as well as the relative weight of the two Gaussians. Simple 3D Gaussian and ellipsoidal shapes were also implemented.

“Fractal” shower simulation

This approach is based on a concept of modeling the essence of a hadron shower without going into the details too deeply. Here, the incident hadrons deponate energy along their track as they propagate, and split up randomly with certain probability, getting an inclination angle and sharing their momentum according to simple (also randomized) rules. The energy loss is determined by a simplified Bethe-Bloch formula with

experimentally determined parameters. Particles having an energy less than a certain threshold are considered stopped and deponate all their energy at the spot³. Some examples are visualized on Fig. 5.3.

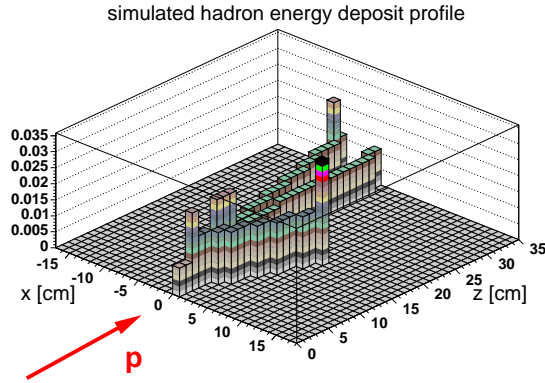


Figure 5.3. Energy deposit of a π^+ shower profile simulated with the “fractal” model. The arriving particle is indicated with the red arrow, and initially carries 1 GeV energy. (Compare the spatial dimensions to the $5.5 \times 5.5 \times 37.5 \text{ cm}^3$ size of a PbSc tower.)

5.2.2 Findings

It became clear that the hadron showers show more variation than the electromagnetic ones, therefore it is not possible to model them with a simple geometrical shape described with a couple of parameters, but random effects have to be involved. We have developed two models, which have proven that, with appropriate tuning, the shower shape describer quantities can be modeled. Verification of the Fast hadron MC simulations shows that the orthogonal-peripheral dependence is better described than that of GEANT. We have also tested that these descriptors can be simulated successfully in different energy bins as well as at orthogonal and peripheral impacts. In the case of the example

³The name of the model is inspired by the observation that if $dE/dx = \text{constant}$ and there is no energy threshold (letting particles split forever), then the particle tracks of the shower draw a fractal image. Since in fact the energy loss is not constant but higher for small momenta and also there is a finite threshold, slower particles will dissipate their energy quickly, producing a “chunkier” energy deposit structure.

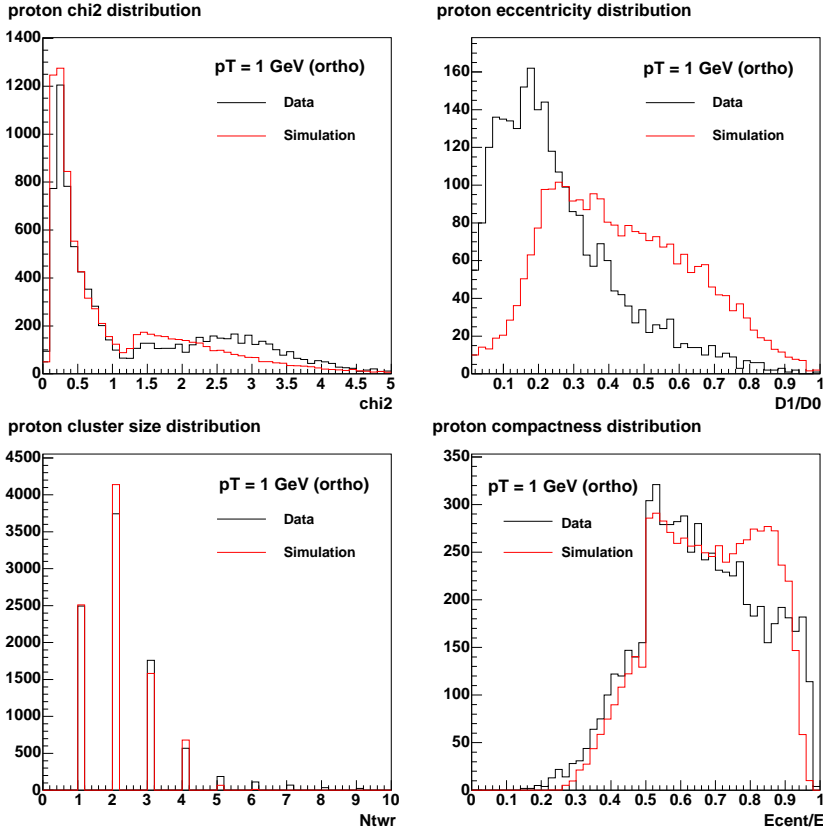


Figure 5.4. Verification plots of the fractal simulation of protons, for several shower descriptors for $0.9 \text{ GeV} \leq E < 1.1 \text{ GeV}$ orthogonal hits. From left to right, top to bottom: χ^2 , eccentricity, cluster size and compactness distributions are shown.

(with 1 GeV protons using the Fractal model) shown on Fig. 5.4, we describe N_{twr} and χ^2 better than GEANT does, while there is a serious discrepancy with the eccentricity, and compactness is also problematic (although it is in GEANT too).

This, in turn, provides us with the feeling that we can describe the essence of a hadronic shower with this top-to-bottom approach. However, comparing simulations to data is a complicated and not an exactly quantifiable process, therefore there seems to be no golden way, such as some multi-parameter fit, to find the appropriate setup for the Monte Carlo.

5.3 Application: direct photons

Due to the fact that photons, once produced, are essentially unaffected by the surrounding matter, measurement of direct photon production allows the most definitive discrimination between initial- and final-state suppression effects in heavy ion collisions at RHIC.

The first measurements of PHENIX direct photons on $\sqrt{s_{NN}} = 200$ GeV Au+Au data from Run-2 showed that there was additional direct photon yield in nucleus-nucleus collisions [34], in accordance with the theoretical calculations that attribute it to various processes such as momentum broadening of the incoming partons, additional fragmentation contributions, or additional scattering in the thermalizing dense matter of the final state [35]. The Run-2 measurement was later repeated on Run-4 data with higher precision. The two results were found to be consistent [36].

Moreover, the low- p_T direct photon enhancement provides the clearest proof so far that a strongly interacting quark-gluon plasma is created in high energy heavy ion collisions at RHIC: the initial temperature of the quark matter is $300 \text{ MeV} < T_{\text{init}} < 600 \text{ MeV}$, significantly higher than the Hagedorn temperature $T_H \approx 170 \text{ MeV}$ above which no hadronic matter can exist [6].

5.3.1 Analysis

I used stochastic cuts and simulation verification for particle identification purposes and systematic checks that contributed to the photon production measurements in both the Run-2 and Run-4 $\sqrt{s_{NN}} = 200$ GeV Au+Au collisions [37]. Both the Run-2 and Run-4 PHENIX direct photon measurements follow the background subtraction method⁴, where the direct photon signal is extracted from the inclusive photon spectrum measured in PHENIX by subtracting the decay photon contribution from hadrons. This section tersely recapitulates the main steps of the Run-4 direct photon analysis in the PbSc, detailed in Ref. [37], and summarizes some of the main results.

⁴As discussed in Sec. 1.2.3, the low- p_T part of the direct photon spectrum was computed differently, using the virtual photon yield reconstructed from electron pairs.

Measuring the inclusive photon spectrum

A photon selection identical to that described in Sec. 4.3 was applied as a first step in order to reduce non-photonic background to its minimum. Then the following (mostly p_T -dependent) corrections are applied:

- Geometrical acceptance (a_γ) is calculated using single photon simulation. The photon acceptance is $a_\gamma \approx 0.23$ in the PbSc, virtually independently of p_T .
- Photon detection efficiency (ϵ_γ) and hadron contamination (X_{had}) is computed for the selected PID cut (no PID, $\chi^2 < 3$ or PID2) as described in 4.1. This step strongly relies on simulation verification (Section 5.1). Decay photons from π^0 -s above $p_T \approx 12$ GeV in the PbSc and $p_T \approx 16$ GeV in the PbGl tend to merge into a single cluster, thus creating fake photons that have to be corrected for. In case of the $\chi^2 < 3$ the number of fake clusters below $p_T = 15$ GeV is less than 2%, but it rises to $\approx 20\%$ at $p_T = 25$ GeV. However, then merging has a negligible effect below 20 GeV when the PID2 cut is applied.
- Because the spectrum is smeared by the energy resolution, an unfolding correction (c_{fold}) is applied.
- Loss of photons due to their conversion probability into electrons within the detector material (p_{conv}) was taken into account.
- Due to the steep exponential shape of the spectrum, the finite size of the bins cause the measured points to be shifted upwards from the ideal curve. Therefore a bin shift correction (c_{bin}) has to be applied.

With all the above corrections, the inclusive photon yield per event can be computed from the measured number of photon clusters N_{clus} in the bin centered around p_T with a width Δp_T as

$$\frac{1}{N_{evt} 2\pi p_T} \frac{d^2 N_{incl}^\gamma}{dp_T dy} = \frac{1}{N_{evt} 2\pi p_T} \frac{N_{clus}}{\Delta p_T \Delta y} \frac{(1 - X_{had}) c_{fold}}{c_{bin} (1 - p_{conv}) \epsilon_\gamma a_\gamma}, \quad (5.1)$$

where N_{evt} is the number of events used in the analysis and Δy is the rapidity span.

Extracting the direct photon yield

The overwhelming part of the photons emerge from hadronic decays. These background processes need to be understood and analyzed. The spectra of the main background sources are π^0 , η , ω , η' (in this order), which have to be reconstructed and then subtracted⁵. The main factor of the systematic uncertainties comes from this step, basically limiting the reconstruction of direct photon spectrum at low momenta⁶.

The so called *double ratio* is computed as a first step. In this case the measured inclusive γ/π^0 ratio is divided by the γ/π^0 ratio of the computed background. This has the advantage that uncertainties from the energy scale, efficiency calculation and conversion correction (partially or totally) cancel. Since the π^0 spectra are the same in the two cases, any significant deviation of the double ratio above unity indicates a direct photon excess. The direct photon spectrum is expressed from the inclusive photon spectrum using the double ratio⁷ as

$$\frac{1}{N_{evt}2\pi p_T} \frac{d^2 N_{direct}^\gamma}{dp_T dy} = \left(1 - \frac{(N^\gamma/N^{\pi^0})_{meas}}{(N^\gamma/N^{\pi^0})_{bkgrd}} \right) \frac{1}{N_{evt}2\pi p_T} \frac{d^2 N_{incl}^\gamma}{dp_T dy}. \quad (5.2)$$

5.3.2 Results

The corrected double ratios are compared to the expected yields of background photons from hadronic decays in Fig. 5.5 for minimum bias Au+Au collisions (0%–92% centrality) and for eight centrality classes, separately for PbSc and PbGl. An excess is observed at high p_T with a magnitude that increases with increasing centrality of the collision. The lowest p_T points suggest a trend of thermal photon excess, although this observation is not significant⁸.

The extracted direct photon spectrum is shown in Fig. 5.6. The main sources of systematics are summarized in Table 5.1. The result is consistent with pQCD calculations. However, an excess of direct

⁵The frequent resonances are reconstructed in separate analyses, while the less abundant resonances are taken into account assuming m_T -scaling. Section 4.3 overviews such a π^0 reconstruction analysis.

⁶In fact the factor of ~ 5 suppression of hadrons is a fortunate circumstance that allowed for a relatively good quality photon measurement in PHENIX.

⁷Note that the double ratio $\frac{(N^\gamma/N^{\pi^0})_{meas}}{(N^\gamma/N^{\pi^0})_{bkgrd}} \equiv \frac{N_{meas}^\gamma}{N_{bkgrd}^\gamma}$.

⁸A significant excess of thermal photons is measured, however, using the virtual photon method and it is shown on the left panel of Fig. 5.6).

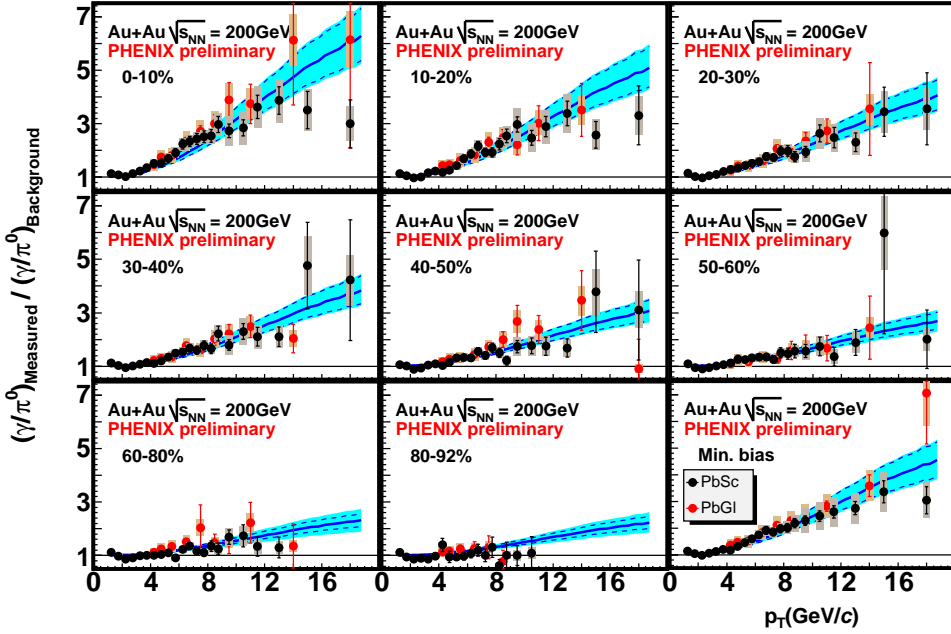


Figure 5.5. Run-4 preliminary $\frac{(N_\gamma/N^{\pi^0})_{meas}}{(N_\gamma/N^{\pi^0})_{bkg rd}}$ double ratios as a function of p_T for minimum bias and for eight centralities of Au+Au collisions at $\sqrt{s_{NN}} = 200$ GeV. PbSc and PbGl measurements are shown separately. Statistical and total errors are indicated separately on each data point by the vertical bar and shaded region, respectively. The solid curves are the ratio of pQCD predictions to the background photon yield based on the measured π^0 yield. The shaded region around the curves indicate the variation of the pQCD calculation for scale changes from $p_T/2$ to $2p_T$, plus the $\langle N_{coll} \rangle$ uncertainty.

photons was found in reconstructed virtual photons from dielectron spectra below 5 GeV [6] (as already mentioned in Sec. 1.2.1).

The different contributions to the direct photon yields can be separated using theoretical models: the fraction of the hard processes is computed with pQCD. The low momentum part of the spectrum is expected to be dominated by the thermal radiation, while the photons at higher momentum come from the hard processes.

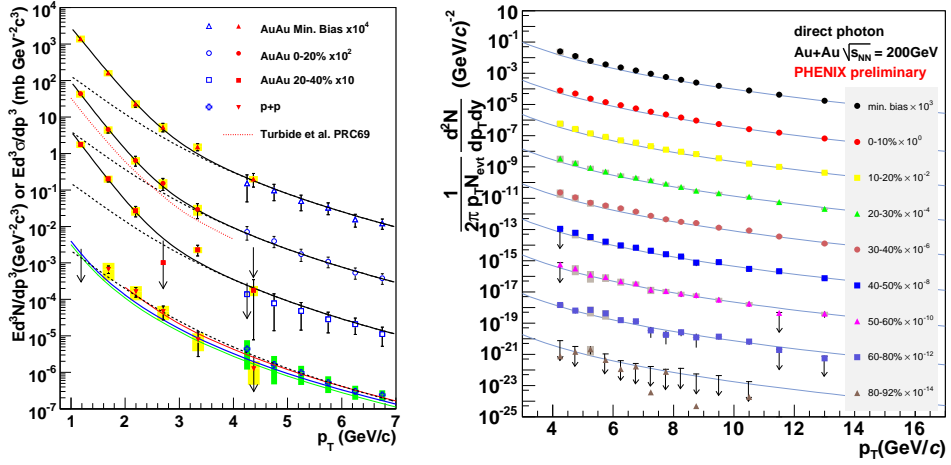


Figure 5.6. Combined PbPb+PbSc direct γ invariant yields as a function of transverse momentum for different centrality selections and minimum bias Au+Au collisions at $\sqrt{s_{NN}} = 200$ GeV. *Left:* Measurements from virtual photons (filled points) are in agreement with Run-2 measurements (open symbols), above 4 GeV/c and show a clear excess over the extrapolation to lower p_T s. The p+p results are also plotted, and do not show this excess. *Right:* Run-4 preliminary results for higher p_T values. (Error bars represent the total error. Arrows indicate measurements consistent with zero yield. The solid curves are pQCD predictions.)

systematic errors p_T	double ratio			central yield		peripheral yield	
	2 GeV	6 GeV	10 GeV	6 GeV	12 GeV	6 GeV	12 GeV
yield extraction	6%	6%	6%	8.5%	2.1%	30%	7.5%
energy scale	3%	3%	3%	22%	12%	56%	20%
off-vertex γ	2%	2%	2%	4.2%	2.1%	12%	3.8%
hadron contamination	7%	7%	7%	17%	9.5%	42%	16%
γ unfolding	9%	6.2%	5%	14%	6.8%	36%	11%
η/π^0 ratio	2%	2%	2%	3%	0.7%	10%	2.5%
merging correction	0%	0%	20%	1.5%	7%	5%	25%
$(N^\gamma/N^{\pi^0})_{bkgd}$ fit	3%	3%	3%	4.2%	1%	15%	3.7%
conversion correction	1.5%	1.5%	1.5%	4.2%	2.1%	12%	3.8%
total	13.7%	12.3%	22%	33%	18%	88%	39%

Table 5.1. Systematic errors of the direct photon yield (central and peripheral events separately) and excess double ratio (minimum bias events) measured in Run-4 $\sqrt{s_{NN}} = 200$ GeV Au+Au collisions in the PHENIX PbPb at different p_T ranges.

Chapter 6

Bose-Einstein correlations and PHENIX images

6.1 The HBT effect

Correlation between identical pions emitted from a thermalized source with similar momenta is due to the bosonic nature of the pions. The phenomenon is often referred to as Bose–Einstein correlation (BEC) [38]. The correlation functions carry important information about the space-time extent and the dynamics of the particle emitting source. R. Hanbury Brown and R. Q. Twiss used the bosonic correlation of photons to measure the angular diameter of distant stars [39]. BEC, or the HBT effect (named after the initials of the discoverers) has become an important tool in high energy physics. In most high energy heavy ion experiments there is enough statistics to measure the two- and three-particle correlation function of charged pions.

The Bose–Einstein correlation function of pion-pion pairs can be expressed in terms of the relative and the mean four-momenta, $\Delta k \equiv \Delta k^\mu = k_1^\mu - k_2^\mu$ and $K \equiv K^\mu = (k_1^\mu + k_2^\mu)/2$, respectively:

$$C(\Delta k, K) = \frac{N_2(\mathbf{k}_1, \mathbf{k}_2)}{N_1(\mathbf{k}_1)N_1(\mathbf{k}_2)}, \quad (6.1)$$

where $k_{1,2}^\mu$ are the four-momenta and $\mathbf{k}_{1,2}$ are the three-momenta of particles 1 and 2, N_1 and N_2 are the one- and two-particle invariant momentum distribution functions¹. The correlation can be related to

¹The usual $m^2 = k^2 \equiv k^\mu k_\mu = E^2 - \mathbf{k}^2$ notation is used here, where $k^\mu = (E, \mathbf{k})$ and \mathbf{k} is the 3-momentum.

Fourier transform of the one-pion emission function $S(x, K)$ as

$$\begin{aligned} C(\Delta k, K) &= 1 + \frac{|\tilde{S}(\Delta k, K)|^2}{|\tilde{S}(0, K)|^2}, \\ \tilde{S}(\Delta k, K) &= \int d^4x S(x, K) e^{i\Delta k x}. \end{aligned} \quad (6.2)$$

6.1.1 The core–halo picture

It has been shown that the source can be handled in the core–halo picture, where the “core” consists of primordially created pions and those ones coming from short-lived resonances, while the other pions, coming from more slowly decaying resonances, make the “halo” [41, 42]. The core region is resolvable by BEC, while the halo is not². In fact, the core–halo separation always depends on the experimental two-track resolution. For example in PHENIX and STAR, two tracks are separable with a momentum difference of δQ larger than 4 to 5 MeV, corresponding to a spatial separability δx that dies off at $\hbar/\delta Q \approx 40\text{-}50$ fm [43, 44]. Long tails extending to this region were recently observed by the PHENIX and NA49 collaborations at RHIC and CERN SPS energies [43, 45]. Note that these long tails are also seen in kaon imaging, while the bulk production is well described with characteristic scales of 4-6 fm [52].

The intercept parameter

In the core–halo picture [41, 42] the correlation function can be measured with the so called extrapolated intercept parameter λ_* as

$$C(\Delta k, K) = 1 + \lambda_* R_c, \quad (6.3)$$

where R_c is defined by the Fourier transform of the one-pion emission function $S_c(x, K)$ of *solely the core* as

$$R_c = \frac{|\tilde{S}_c(\Delta k, K)|^2}{|\tilde{S}_c(0, K)|^2}. \quad (6.4)$$

and the intercept parameter λ_* is derived from the *extrapolation* of the correlation value to $\Delta k = 0$, as $\lambda_* = C(0, K) - 1$. However, this

²This has been tested numerically in [40].

extrapolation does not include the correlation between halo–halo and core–halo particle pairs, supposed to be unresolvable by our detectors³.

The intercept parameter can also be expressed directly with the fraction of the core pions to the total number of pions⁴:

$$\lambda_*(m_T) = \left(\frac{N_{core}^{\pi^+}(m_T)}{N_{core}^{\pi^+}(m_T) + N_{halo}^{\pi^+}(m_T)} \right)^2 \quad (6.5)$$

where

$$N_{halo}^{\pi^+}(m_T) = N_{\omega \rightarrow \pi^+}^{\pi^+}(m_T) + N_{\eta' \rightarrow \pi^+}^{\pi^+}(m_T) + N_{\eta \rightarrow \pi^+}^{\pi^+}(m_T) + N_{K_S^0 \rightarrow \pi^+}^{\pi^+}(m_T) \quad (6.6)$$

and it is per se sensitive to the core vs. halo ratio. (In the above formulae $m_T = \sqrt{m^2 + p_T^2}$ denotes the transverse mass of the π^+ s, and the $N^{\pi^+}(m_T)$'s are the m_T distributions of the corresponding decays.) If the rotation symmetric “one-dimensional” Gaussian approximation is a valid description of the source, Eq. (6.3) yields the form

$$C(q) = 1 + \lambda e^{-|qR|^2}, \quad (6.7)$$

characterized by the invariant momentum difference $q = \sqrt{(k_1 - k_2)^2}$ and the one dimensional Gaussian radius R of the source. In this case $\lambda \equiv \lambda_*$.

The Edgeworth expansion

As λ_* is defined in Eq. (6.3) as an *extrapolation* of the experimental data to $\Delta k^\mu \rightarrow 0$, it is essential that it does not depend strongly on the method of the extrapolation. The Gaussian assumption for the shape of the source is a model hypothesis that has been shown not to be precise for certain kind of data [43]. Instead, one can choose an experimental procedure independent of theoretical assumptions, and get a description of arbitrary precision with the Edgeworth expansion by completing the Gauss shape with an infinite series in the space of Hermite polynomials [85].

³For fully thermal particle emitting sources, the exact value of intercept is 1. Generally, $\lambda_* \leq 1$ for thermal or partially coherent sources. For squeezed sources, however, $\lambda_* \geq 1$ or even $\lambda_* < 0$ is also possible.

⁴Although all the formulae here are restricted to π^+ s, they are similarly valid for π^- s.

In this case

$$C(q) = \mathcal{N} \left[1 + \lambda_E e^{-q^2 R_E^2} \left(1 + \sum_{n=3}^{\infty} \frac{\kappa_n}{n!} H_n(\sqrt{2}qR_E) \right) \right], \quad (6.8)$$

where \mathcal{N} is an overall normalization parameter, κ_n is a weight factor to the n th Hermite polynomial

$$H_n(t) = e^{t^2/2} \left(-\frac{d}{dt} \right)^n e^{-t^2/2}, \quad (6.9)$$

and R_E and λ_E are the Edgeworth radius and intercept parameters. In practice, an expansion up to the 6th order is sufficient [76]. Note that, as the even order Hermite polynomials have non-vanishing values at $t = 0$, λ_E is different from λ_* here:

$$\lambda_* = \lambda_E \left[1 + \frac{\kappa_4}{8} - \frac{\kappa_6}{48} + \dots \right]. \quad (6.10)$$

A straightforward generalization of these approximations to the three (out, side, long) dimension case is given in [86].

6.1.2 Source imaging

In the approximate case when multi-particle correlation effects are negligible, the BEC function can be well described theoretically even in the case when final state interactions (FSI) play important role. The two-particle correlation function of the pions can be calculated from the source function as follows [46]:

$$C(q) - 1 = \frac{1}{2} \int d^3\mathbf{r} (|\Phi_C(q, \mathbf{r})|^2 - 1) S_{12}(\mathbf{r}), \quad (6.11)$$

where $S_{12}(\mathbf{r})$ is the relative source function corresponding to the two-particle relative coordinate (\mathbf{r}) distribution, and $\Phi_C(q, \mathbf{r})$ is the symmetrized final state two-particle outgoing wave function. In case of Coulomb-interaction, this has an analytic form [47, 48]. With the imaging method (by inverting this integral equation) one can determine the $S_{12}(\mathbf{r})$ source function. With spherical symmetry assumed, $S_{12}(\mathbf{r})$ depends only on $r := |\mathbf{r}|$. In the followings we denote this quantity with $S(r)$.

6.2 Analysis of the heavy tail of particle emission in PHENIX

Emission source functions have been extracted from correlation functions of charged pions produced at mid-rapidity in Au+Au collisions at $\sqrt{s_{\text{NN}}} = 200$ GeV [43], using a model-independent imaging technique developed by D. Brown and P. Danielewicz [49]. The source parameters extracted from lower transverse momentum (k_{T}) pions measured in PHENIX give the indication of a long tail, which differs from that of a Gaussian distribution. This non-trivial structure needed explanation, therefore I studied the heavy tail by comparing it to two simulations based on different principles. THERMINATOR, a Monte Carlo event generator designed for studies in relativistic heavy-ion collisions is used to model and investigate the influence of resonance decays on the tail of particle emission source. It lacks the implementation of rescattering, which, as we have learnt from Hadron Rescattering Code (HRC) simulations, is a possible explanation of the power-law tail. In this section I overview the analysis of the PHENIX heavy tails with the THERMINATOR and HRC simulations, further detailed in Refs. [50, 51].

Like-sign kaon correlation data that we have measured in $\sqrt{s_{\text{NN}}} = 200$ GeV Au+Au collisions at the PHENIX experiment [52] helped to pin down the main source of the heavy tail seen in PHENIX hadron source images by clarifying that the resonance decays cannot be the sole source of the observed behavior. The angle averaged correlation functions and source images reconstructed from PHENIX pion and kaon Hanbury Brown–Twiss (HBT) measurements are summarized in Fig. 6.1.

6.2.1 Hadron rescattering

It has been shown [53, 54] that calculations based on a hadronic rescattering model agree reasonably well with experimental results on single particle spectra, elliptic flow, HBT radii in Au+Au collisions at RHIC energies. The model we use here to compare PHENIX data with is Tom Humanic’s Hadronic Rescattering Calculations. The model contains the eight most abundant resonances, simulates their complete decay chains, and takes rescattering into account.

I discuss the simulated source of charged pions in three groups, determined by time of creation. The *core* consists of the primordial

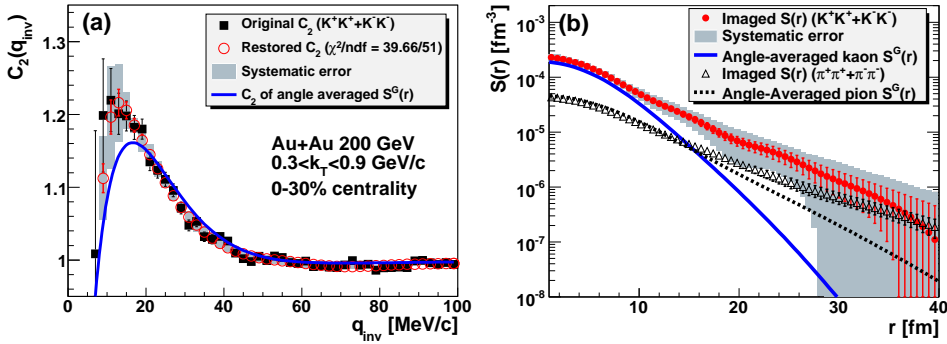


Figure 6.1. (a) (filled squares) measured Correlation function $C_2(q_{inv})$. (open circles) restored $C_2(q_{inv})$ from imaged $S(r)$, compared with (solid curve) angle-averaged Gaussian $C_2(q_{inv})$ for charged kaon pairs measured for $0.3 \text{ GeV}/c < k_T < 0.9 \text{ GeV}/c$ at 0 – 30% central Au+Au collisions at $\sqrt{s_{NN}} = 200 \text{ GeV}$. (b) (filled circle) Imaged kaon $S(r)$ compared with (solid curve) angle-averaged Gaussian $S(r)$. Error bars are statistical only and boxes indicate the total systematic errors. (open triangle) $S(r)$ for charged pion pairs for the same k_T region. For the pion $S(r)$, error bars include both statistical and systematic errors.

particles and the decay products of the short lived resonances. The secondary pion sources of long lived resonances are referred to as the *halo*, while the decay products of the $\omega(782)$ meson, partly resolvable by our detectors, are considered as a separate class (see Table 6.1).

Group	Lifetime	Components in HRC
core	$< 20 \text{ fm}/c$	primordial π^\pm , ρ , Δ , K^*
omega	$\approx 23 \text{ fm}/c$	$\omega(782)$
halo	$> 25 \text{ fm}/c$	Λ , Φ , η , η'

Table 6.1. Components of charged pion sources in the HRC simulation as grouped in this discussion.

On Fig. 6.2, note the excellent agreement between PHENIX data and HRC simulation in the central, low k_T case. The agreement is also acceptable in the full range for the peripheral low k_T case. However, HRC fails to describe the k_T dependence of the source.

Further investigations have shown that the $\omega(782)$ does not account

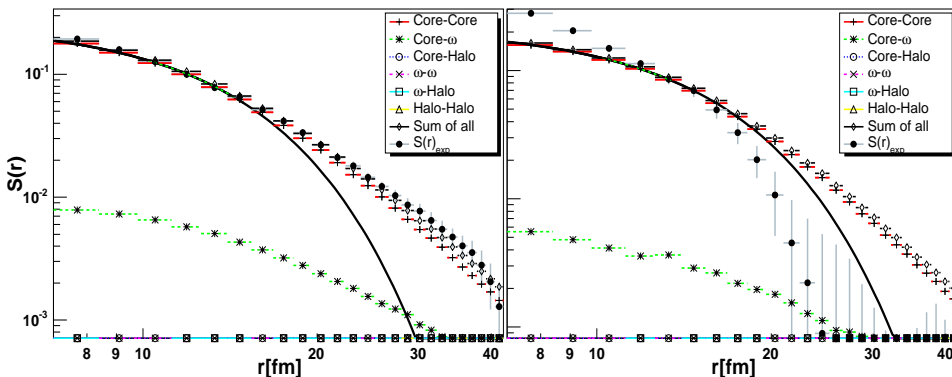


Figure 6.2. Pion pair source measured in PHENIX and HRC simulation for central (0 – 20%) collisions. *Left:* low k_T ($200 \text{ MeV} < k_T < 360 \text{ MeV}$), *right:* high k_T ($480 \text{ MeV} < k_T < 600 \text{ MeV}$). Solid dots represent data on each figure. Black crosses are simulation, while color symbols stand for different components of the simulated source as explained on the legend. The Gauss fit to $S(r < 15 \text{ fm})$ is shown as a continuous line.

for the heavy tail in the simulation. Core-core pairs themselves have a power-law tail in the $S(r)$ distribution. In the HRC, rescattering goes on until it self-quenches. The mean free path increases strongly as the system expands, and rescattering in such a time dependent mean free path system corresponds to an anomalous diffusion. Anomalous diffusion is known to lead to power-law tailed distribution, as stated by a generalization of the Central Limit Theorem [55, 56].

6.2.2 Single freeze-out with THERMINATOR

THERMINATOR—A Thermal Heavy Ion Generator [57], based on the Cracow Single Freeze-out Model [58] was used for the following simulations. In this model, freeze-out of the partonic matter occurs on a single space-time surface, governed by universal thermodynamic parameters. Particle distribution is determined by the thermodynamical equilibrium. Particles propagate freely and the decay of 385 resonances is fully implemented. In opposition to the HRC simulation, rescattering effects are neglected here.

PHENIX source simulated

THERMINATOR simulation provides a flat rapidity distribution. Several checks were done to verify that a realistic distribution and p_T spectrum of particles is generated.

Centrality can not be directly set in THERMINATOR, but through the parameters ρ_{max} and τ , where ρ_{max} stands for a radius of a boost invariant axially symmetric cylinder, while τ denotes the proper time of a simultaneous freeze-out and hadronization [59]. Although fitted parameters for the spectra of all four RHIC experiments including PHENIX were published, PHENIX p_T spectra is not well described by THERMINATOR, being primarily developed for, and tuned to STAR. Thus I used the parameters corresponding to STAR spectrum fits. This indicates that THERMINATOR might be able to show much better agreement with data with further tuning. The central data region 0 – 20% has been reproduced using simulated events from the three most central regimes in proportion to their span. The 40 – 90% regime was substituted with equal number of events simulated in the regimes of 50 – 60% and 70 – 80%.

I simulated a separate set of events for each centrality bin of 5% for central, and 10% for peripheral collisions. Then these sets were concatenated to make up the wider regimes of PHENIX data. THERMINATOR was able to reproduce the centrality dependence of the data. It is also capable to describe the k_T dependence to a much higher accuracy than HRC does, although there is a significant discrepancy at the higher k_T region, as shown on Fig. 6.3.x

It must be noted that there is a significant excess in the simulated $S(r)$ at small r values. Our studies have shown that neither the primordial nor the resonance particles are responsible for it alone, but the $r \rightarrow 0$ peak vanishes if all the core particles and the short lived ($\Gamma \geq 150\text{MeV}$) resonances are excluded from the source (see Fig.6.4). This can be explained with the freeze-out that occurs in a single surface in this model, and the lack of rescattering.

Further simulations indicate that rescattering and resonance decay create very different sources for different particles (π^\pm , K^\pm and p^\pm). THERMINATOR predicts a less heavy tail for the kaons and protons than for the pions, as observable on Fig. 6.4.

A study of direction-dependent PHENIX pion-pair source functions using THERMINATOR Blast Wave and Single Freeze-out and models

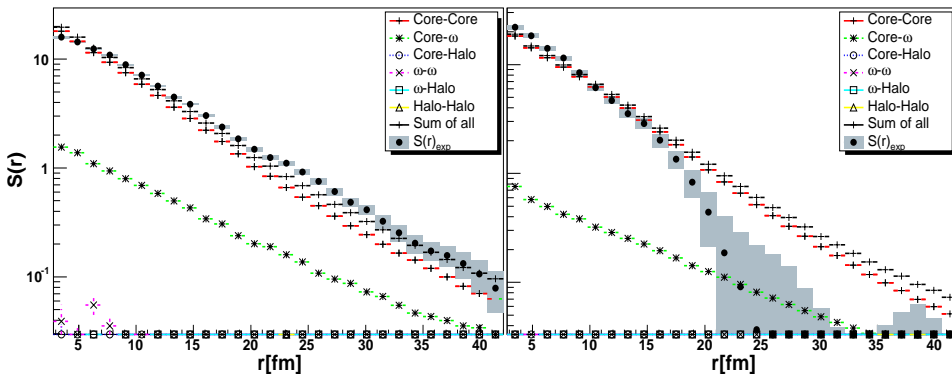


Figure 6.3. Pion pair source measured in PHENIX and THERMINATOR simulation for central ($0 - 20\%$) collisions. *Left:* low k_T ($200 \text{ MeV} < k_T < 360 \text{ MeV}$), *right:* high k_T ($480 \text{ MeV} < k_T < 600 \text{ MeV}$). Solid dots represent data on each figure. Black crosses are simulation, while color symbols stand for different components of the simulated source as explained on the legend.

has been carried out by P. Chung et al. [60] and concluded that these models, although they do well in the "sideways" and "long" directions, fail in the "outward" direction (in the terms of the Bertsch-Pratt parameterization [61]).

Results and discussion

THERMINATOR is a simple model that shows a high power in the description of particle spectra of the large heavy ion experiments. Although there is no rescattering implemented in this model, it reproduces the PHENIX image with the observed heavy power-law tail for the lower k_T events with a higher accuracy than HRC—although it still slightly over-predicts the tail for the high k_T regime, and fails for $r \rightarrow 0$ because of its inherent limitations.

The relatively good agreement including the reproduction of the long-range tail can be understood by taking into account that the high number of resonances provide us with an almost-continuum distribution of lifetimes, increasing virtually to infinity. This results in an approximate power-law-like final distribution [62] just as anomalous diffusion does [55]. However, THERMINATOR fails to describe cor-

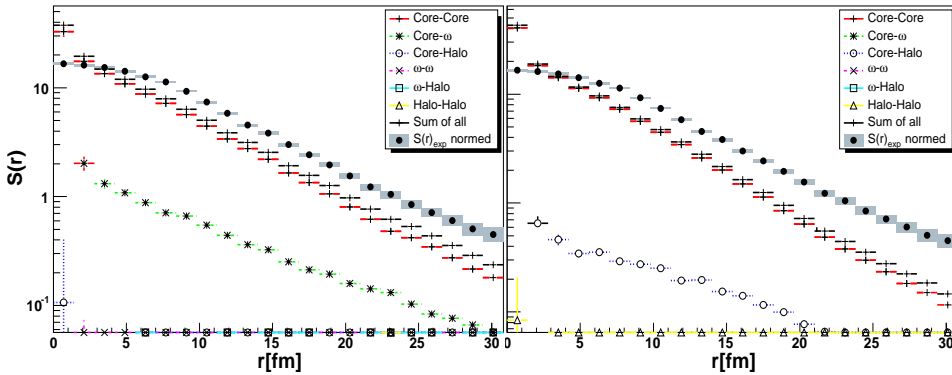


Figure 6.4. THERMINATOR simulation for central, (0 – 20%) collisions for $200 \text{ MeV} < k_T < 360 \text{ MeV}$ pions (*left*) and kaons (*right*). All are compared to PHENIX pion correlation data, represented by the solid dots. Black crosses are simulation, while color symbols stand for different components of the simulated source as explained on the legend. Mismatch at $r \rightarrow 0$ can be observed. THERMINATOR predicts a less heavy tail for the kaons and protons than for the pions. This is in sharp contrast with the HRC predictions given in [56].

rectly the intercept λ and the HBT radii R_{side} , R_{long} and R_{out} [63]. So it is questionable that resonance decays alone were sufficient to describe the experimentally seen structure of source as Bialas had proposed [62].

6.3 Conclusions

Source images of PHENIX data have been studied with two fundamentally different, simple models. Both were able to reproduce the observed one-dimensional images to a certain level, but had their limitations. The different kinematic mechanisms give similar shapes determined by the same underlying mathematical principle (a generalization of the Central Limit Theorem), and so that any of them can be a potential explanation of the measured heavy power-law tails for pions. The predictions for kaon images vs. the pion images are, however, sharply different. I summarized my findings in the following points, also citing the corresponding publications.

1. HRC simulations describe the low k_T PHENIX image, but do

not have the right k_T dependence, as the simulated $S_{12}(r)$ still has the large tail for higher k_T values, contrary to PHENIX data (Fig. 6.2). The reason for the heavy tail is that rescattering changes the mean free path and thus causes anomalous diffusion [51].

2. THERMINATOR simulations provide a reasonable reproduction of the k_T and centrality dependent behavior of the 1D PHENIX image (Fig. 6.3). The heavy tail in those simulations can be explained by the large number of resonances in that model. This produces an effect that is similar to the anomalous diffusion [51].
3. However, THERMINATOR fails to describe the direction dependently parameterized PHENIX source functions, suggesting that resonance decays alone are not sufficient to explain the measured structure of the source [51].
4. Measurement of $S_{12}(r)$ images for π^\pm , K^\pm and p^\pm can indeed make a harsh distinction between rescattering and resonance decay effects. While THERMINATOR simulations predict more long-lived resonances and therefore an even heavier tail in the kaon than in the pion case [51], PHENIX measurements show just the opposite (See Fig. 6.1). Therefore the long-lived resonances can be ruled out as a sole explanation of the heavy tail [52].

Chapter 7

A quest for the $U_A(1)$ symmetry restoration

In high energy heavy ion collisions a hot and dense medium is formed, where the $U_A(1)$ or chiral symmetry may temporarily be restored. As a consequence, the mass of the $\eta'(958)$ mesons may be reduced to its quark model value, and the abundance of η' mesons at low p_T may be enhanced by more than a factor of 10. The intercept parameter λ_* of the charged pion Bose–Einstein correlations provides a sensitive observable of the possibly enhanced η' abundance. I analyzed $\lambda_*(m_T)$ data from $\sqrt{s_{NN}} = 200$ GeV central Au+Au reactions measured at RHIC, using extensive Monte Carlo simulations based on six popular models for hadronic multiplicities. Based on the combined STAR and PHENIX dataset, and on various systematic investigations of resonance multiplicities and model parameters, I conclude that in $\sqrt{s_{NN}} = 200$ GeV central Au+Au reactions the mass of the η' meson is reduced by $\Delta m_{\eta'}^* > 200$ MeV, at the 99.9 % confidence level in the considered model class. Such a significant η' mass modification may indicate the restoration of the $U_A(1)$ symmetry in a hot and dense hadronic matter and the return of the 9th “prodigal” Goldstone boson. A similar analysis of NA44 S+Pb data at top CERN SPS energies showed no significant in-medium η' mass modification.

7.1 The η' – a special choice

In this section I briefly recapitulate the theoretical background of the η' mass modification and how it serves as a window to the field of chiral

dynamics. I also overview possible observation channels and highlight the importance of BEC measurements in high energy heavy ion collisions as a handle to access the phenomenon of the mass modification. For further details on the extrapolation techniques and on a summary of earlier results on a correlation search for partial $U_A(1)$ symmetry restoration I recommend the review paper [64]. Theoretical results and earlier experimental searches for in-medium mass modifications of hadrons were summarized recently in Ref. [65].

7.1.1 Quark model symmetries

In terms of the quark model, one can observe a spontaneous symmetry breaking of the approximate $SU(3)_L \times SU(3)_R$ symmetry, resulting in nine pseudo-Goldstone bosons, that are usually associated with the light mesons formed as u, d, s quark-antiquark bound states. This naïve picture is, however, complicated by the fact that the η' meson has a large mass of the order of 1 GeV. As early as in 1970, Kobayashi and Maskawa concluded that the large mass of the η' meson (formerly known as X) is a serious problem that is difficult to understand in a chiral $SU(3)_L \times SU(3)_R$ model with an explicit symmetry breaking term between singlet and octet states [66]. They found that the existence of an effective six-quark determinantal vertex is necessary. As shown by 't Hooft in 1976, this vertex is contained in instanton-induced quark interactions [67]. An interesting aspect of this Kobayashi-Maskawa-'t Hooft or KMT term [68] is that it can give rise to a flavor mixing in the scalar as well as in the pseudo-scalar channels. The coupling between the pseudo-scalar singlet and octet states η_0 and η_8 arises both from the $SU(3)_V$ breaking and the anomaly terms, assuming isospin symmetry. The physical η and η' mesons are given by the mixing of the η_8 and η_0 modes, and the mass of the η_0 singlet state turns out to be sensitive to the strength of the KMT vertex. An explicit calculation for the general case gives the mixing angle $\theta_\eta(m_\eta^2) = -20.9^\circ$ [68].

The η and η' mesons change their masses as a function of the temperature T , due to both the T dependence of the quark condensate, and the possible decrease of the KMT coupling constant with increasing T . The mixing angle θ_η also becomes T dependent: as the temperature increases, mixing between η and η' approximates the ideal one, and the η_0 component in the physical η' decreases. On the other hand, with increasing T , the η_0 tends to play the role of the ninth Nambu-

Goldstone boson of the $SU(3)_L \times SU(3)_R \times U_A(1)$ symmetry, and loses its mass rapidly. At low temperatures, the $U_A(1)$ part of the symmetry is broken by instantons, invoking distinct vacuum states. Tunneling between these vacuum states is only possible “at a cost”, giving extra mass to the η' meson. However, as the transition amplitude is dependent on the strong coupling constant α_s , it follows that the effect of instantons rapidly decreases with increasing energy density. This is an effective restoration of the $U_A(1)$ symmetry at finite T , first suggested in ref. [69]. Thus in high energy heavy ion collisions, where a hot and dense medium is created, the $U_A(1)$ symmetry may temporarily be restored [70–72].

In Refs. [73–75] I reported on the first (although indirect) observation of a significant reduction of the η' mass, based on an analysis of PHENIX and STAR data [76, 77] from $\sqrt{s_{NN}}=200$ GeV central Au+Au collisions at RHIC. In this chapter I overview these experimental signatures of a partial $U_A(1)$ symmetry restoration at RHIC, together with a broad analysis of systematic effects.

In thermal models, the production cross sections of the light mesons are exponentially suppressed by the mass. Since the η' mesons are heavy, by default one expects the number of η' mesons to be about two orders of magnitude less than the number of pions. However, as a consequence of the mass reduction, this suppression would be moderated, and the η' mesons would show up in an enhanced number. Once produced, the η' is expected to be decoupled from other hadronic matter, since its annihilation cross section is very small. At the same time, the low- p_T η' mesons are trapped in the medium due to energy conservation reasons, forming a “condensate” until the medium dissolves. Then the η' mesons regain their original mass, hence the enhancement will mostly appear at low p_T [70–72]. Note that the η' lifetime is much longer than the lifetime of the hot and dense medium, therefore a direct observation of the mass shift seems to be extremely difficult.

7.1.2 Signatures

A promising channel of observation is the dileptonic decay $\eta' \rightarrow \ell^+ \ell^- \gamma$, because a low- p_T η' enhancement would give extra lepton pairs to the low invariant mass region. The paper of Kapusta, Kharzeev and McLerran on the return of the prodigal Goldstone boson [71] was in fact motivated by the dilepton enhancement seen in CERN SPS

200 AGeV/c energies in S+Pb reactions. Recent interpretations of CERES [78] and NA60 data [79] indicate that the approach to a chiral symmetry restored state could proceed through resonance broadening and eventually subsequent melting, rather than by dropping masses or mass dependency or mass degeneracy between chiral partners [80]. Recent PHENIX findings also show a definite excess in the $m_{e^+e^-} \lesssim 1$ GeV dielectron invariant mass region in $\sqrt{s_{NN}} = 200$ GeV Au+Au collisions [81]. Unlike at lower beam energies, in this case the contribution from a hot hadronic phase without mass shifts seems to be insufficient to account for the enhancement seen in the data [82].

The subject of the current analysis, however, is the measurement of the η' mass using published like-sign BEC data as proposed by ref. [83]. Correlations between pions carry important information about the space-time structure of the medium created in heavy ion collisions. The widths of η and η' are $\Gamma_\eta = 1.30 \pm 0.07$ keV and $\Gamma_{\eta'} = 204 \pm 15$ keV, corresponding to large decay times: they produce pions at $c\tau_{\eta'} \cong 967$ fm and $c\tau_\eta \cong 152000$ fm, which are huge compared to the characteristic HBT radii of 4-6 fm. Among the decay channels of the η' , the $\eta' \rightarrow \eta\pi^+\pi^-$ channel has the largest branching ratio of about 45%. Furthermore, the η mesons decay into charged pions: The $\eta \rightarrow \pi^+\pi^-\pi^0$ and $\eta \rightarrow \pi^+\pi^-\gamma$ processes together have a branching ratio of approximately 27% [16]. Hence the η' will contribute to the halo of the pion source, which is accessible via intercept parameter measurements (Section 6.1.1). Later I will argue that the multiplicity of η' is directly connected to its in-medium mass. Therefore the mass reduction of the η' meson, that may be connected to a partial $U_A(1)$ restoration, is able to explain the behavior of λ_* measured in RHIC experiments. A previous analysis, based on the same idea, was carried out on NA44 data, and showed that a reduction of the $m_{\eta'}$ mass should result in a dip of the $\lambda_*(m_T)$ at low- m_T values. However, no significant signal of such a mass modification was seen in $E_{Lab} = 200$ AGeV S+Pb collisions at CERN SPS (Fig. 1 of [83]).

I have carried out a detailed systematic study of the presently available published datasets. Future high precision data points in the low- p_T region will help to reduce the uncertainties of the measurements, and hopefully will provide a more precise estimation of the η' mass reduction, compared to our current analysis.

7.1.3 RHIC datasets

In contrast to the SPS data, a low- m_T dip of the $\lambda_*(m_T)$ was measured in $\sqrt{s_{NN}} = 200$ GeV Au+Au collisions at RHIC by both the STAR and the PHENIX experiments [76, 77]. The $\lambda_*(m_T)$ points were extracted from the measured correlation function of like-sign pions, using different methods. A comparison of the measurements to the FRITIOF [84] calculation including variation of the η' mass was presented in Fig. 4. of ref. [87]. It is important to note that, although the Gaussian fit typically has 1-2% error on the λ value, this does not reflect the real error on the intercept caused by the extrapolation. For example, exponential fits yield larger values for λ than the Gaussian fits do, and the difference between λ_{Gauss} and $\lambda_{exponential}$ is larger than several (sometimes more than 5) standard deviations [88]. A reasonable range of errors can be estimated with the help of an Edgeworth fit [87]. In the detailed presentation of ref. [87] it was suggested to utilize the normalized $\lambda_*(m_T)/\lambda_*^{max}$ quantity in order to remove sensitivity to the extrapolation technique, and to reduce other systematic errors. Note that λ_*^{max} is defined as the value of the extrapolated intercept parameter in an m_T region where its value is saturated; according to simulations as well as the presently used PHENIX and STAR measurements, this corresponds to $0.5 \text{ GeV} \leq m_T \leq 0.7 \text{ GeV}$ region¹. One should also note that the $\lambda_*(m_T)$ data may depend on the goodness of the particle identification too: other particles misidentified as pions will reduce correlation and will push the measured $\lambda_*(m_T)$ data down.

The PHENIX $\lambda_*(m_T)$ dataset was derived using the Bowler-Sinyukov method [89]. STAR used a 6th order Edgeworth expansion (see Section 6.1.1) with the even order terms only, assuming that the source is a symmetric and analytic function. Here I apply the method of Ref. [85] using the values and errors of the Gaussian λ and the $\kappa_{i,n}$ Edgeworth fit parameters taken from [76] in order to compute the 6th order λ_* values using Eq. (6.10). As emphasized before, the Edgeworth λ_* gives a more realistic estimation of both the value and the error of the intercept parameter, hence of the core-halo ratio, than the Gaussian λ does.

¹Here λ_*^{max} is the $\lambda_*(m_T)$ value taken at $m_T = 0.7$ GeV, with the exception of the STAR data, where the data point at the highest $m_T = 0.55$ GeV is considered. Note that the m_T dependency of the $\lambda_*(m_T)$ measurements in the 0.5-0.7 GeV region is very weak.

Another dataset on λ_* from STAR was obtained with a Gaussian fit using the Bowler-Sinyukov method, and it shows a good agreement with the STAR Edgeworth data (Fig. 14 of [76]). I did not use this dataset in our analysis, since the error bars do not include all the relevant systematic effects, being in the order of $\delta\lambda \sim 0.001$, which is way smaller than the systematic error coming from the choice of the extrapolation. PHENIX preliminary data [87] are also shown, for comparison purposes only, as their systematic errors are not yet finalized. The datasets for λ_* are detailed in Figure 7.1 before and after normalizing with λ_*^{\max} . Each of these datasets indicate the dip of λ_* in the low- p_T region.

Given that we are interested in obtaining final errors that include all relevant systematic effects, I decided to analyze simultaneously the PHENIX final Sinyukov-corrected λ_* dataset together with the STAR Edgeworth λ_* dataset, both normalized to their λ_*^{\max} values. One can note that these two datasets are not in perfect overlap with each other, although they are consistent within their errors, and it is possible to fit both datasets simultaneously with good confidence levels. The Gaussian $\lambda(m_T)$ dataset of STAR has errors that apparently do not include systematics from the Gaussian ansatz, thus a quantitative comparison to our model was not reasonable. However, the best fits to the other datasets qualitatively agree with the Gaussian $\lambda(m_T)$ points. I have also checked that separate analysis of the STAR and PHENIX datasets yields results which are consistent with the presented results, as part of the systematic studies. However, the combined PHENIX and STAR dataset provided a more precise estimate for the allowed regions of the model parameters.

The difference between the selected PHENIX and STAR datasets possibly reflects the systematic error from different experimental conditions, for example, PHENIX data were measured in the 0-30 % centrality class, while STAR Edgeworth results were published for the 0-5 % centrality selection, and the particle identification in the two experiments is also different. These differences resulted in a systematic uncertainty of our analysis, too. These systematic errors, however, turn out to be of the order of the statistical uncertainties, while the dominant error in the estimation of the in-medium modified η' mass comes from the choice of the resonance model and its parameters. The relative systematic error from the difference in centrality selection is estimated in Section 7.3.3 to be not larger than 9.8 %.

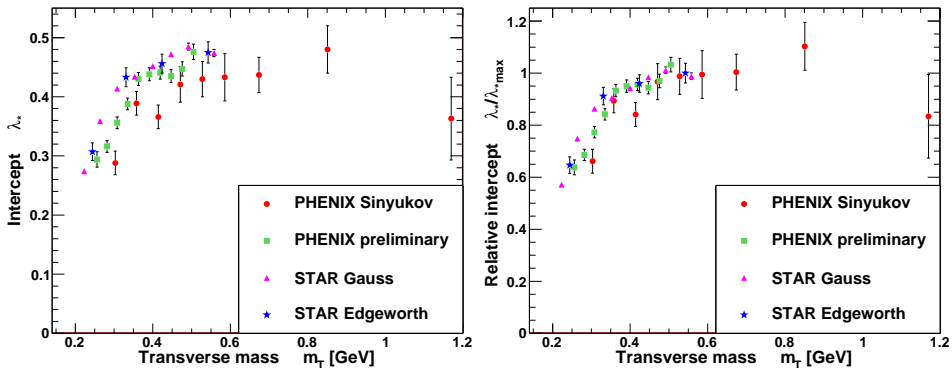


Figure 7.1. Datasets of $\lambda_*(m_T)$ (left) and $\lambda_*(m_T)/\lambda_*^{\max}$ (right) from RHIC $\sqrt{s_{NN}} = 200\text{GeV}$ like-sign pion correlation measurements. Note that the errors on the STAR Gaussian dataset (Fig. 14 of ref. [76]) are in the order of 0.001 MeV (not all systematics included), and one of the PHENIX datasets has only preliminary errors [87]. Hence we are left with the remaining two datasets when evaluating the systematic errors on $m_{\eta'}^*$. (Ref. [77], and Fig. 13 of Ref. [76] recomputed using Edgeworth expansion [75].)

7.2 Modeling and simulation

First simulations of the $U_A(1)$ restoration at SPS S+Pb collisions at $E_{Lab} = 200$ AGeV bombarding energy had predicted a dip of $\lambda_*(m_T)$ at m_T values below 0.25 GeV [83]. It was found that the depth of this dip was governed by the value of $m_{\eta'}^*$ as an input parameter for the simulations. In those simulations, the η' mesons from the condensate had been assumed to have no transverse momenta at all, resulting in a very steep hole-like structure of the low- m_T part of the $\lambda_*(m_T)$ [83]. Such an oversimplification is not adequate for the description of the dip in the RHIC data. To improve on it, I introduced an effective thermal spectrum for the η' mesons from the condensate, characterized by an inverse slope parameter B^{-1} . As I demonstrate below, this parameter B^{-1} controls the steepness of the dip of $\lambda_*(m_T)$, while $m_{\eta'}^*$ controls its depth. Also, instead of relying on a given model of resonance production (as on FRITIOF [84] in Ref. [83]), six different models were utilized in order to estimate the systematic error related to the choice of the theoretical model for resonance production. In particular, the six

models I used in the current analysis were ALCOR [90], FRITIOF [84], Kaneta *et al.* [91], Letessier *et al.* [92], Stachel *et al.* [93] and UrQMD [94]. (See Section 7.2.1 for more details on the individual models.) I also considered the AMPT 2.11 $\lambda(m_T)/\lambda^{\max}$ simulation with string melting [95] that report on a non-thermal scenario without an η' mass modification. AMPT results show an interesting, although genuinely different dropping structure of $\lambda(m_T)$ at low m_T values. Comparison of this model to the data, as tersely overviewed in [74], indicate that AMPT cannot describe these data in a statistically acceptable manner, characterized by a $\chi^2/ndf = 102/13$ corresponding to $CL = 6.8 \times 10^{-16}$. The behavior seen in AMPT can be attributed to a lower effective $\langle u_T \rangle$ of the high mass halo resonances [74, 83].

In earlier simulations in [83], the resonance production was generated by an exponential spectrum $N(m_T) = Ae^{-m_T/T_{eff}}$, the effective freeze-out temperature defined as $T_{eff} = T_{FO} + m \langle u_T \rangle^2$, with T_{FO} and $\langle u_T \rangle$ being the freeze-out temperature and the average transverse flow, respectively. This has also been generalized, and a polynomial prefactor had been introduced in order to achieve a more realistic description of the direct production of resonances. I fixed T_{FO} and $\langle u_T \rangle$ to RHIC measurements [96]. Thus the m_T distribution will follow the form of

$$N(m_T) = Cm_T^\alpha e^{-m_T/T_{eff}}, \quad (7.1)$$

where C is a normalization constant, and $\alpha = 1 - d/2$, where d is the number of spatial dimensions of the expansion (hence $1 \leq d \leq 3$ and α falls between $-1/2$ and $1/2$) [41, 97]. The choice of $\alpha = 0$ corresponds to the case of Ref. [83].

In order to compare to RHIC data at mid-rapidity, I computed the effective intercept parameter of the $\pi^+-\pi^+$ correlations, $\lambda_*(m_T)$, with the definition of Eq. (6.5). All the contributions of Eq. (6.6) to the m_T distribution were simulated in the mid-rapidity region, given by the pseudo-rapidity² cut of $|y| < 0.35$ of the PHENIX acceptance. I took into account in the systematic checks that the STAR analysis [76] used a different pseudo-rapidity cut of $|y| < 0.5$.

For each model the fractions of the particles were computed by normalizing the multiplicities to the total density

$$\rho_{total} = \rho_{core} + \rho_{halo}, \quad \rho_{halo} = \rho_\omega + \rho_{\eta'} + \rho_\eta + \rho_{K_S^0}. \quad (7.2)$$

²In this chapter, pseudo-rapidity is denoted by $y = 0.5 \ln[(|p| + p_z)/(|p| - p_z)]$ instead of η to avoid confusion with the η and η' pseudo-scalar mesons.

The halo of pion production always had the same ingredients (from the decays of the ω , η' , η and K_S^0)³, while the core was composed of all the other resonances that were available in each particular model. The charged pion m_T spectra were obtained from a complete kinematic simulation of the decays above resonances using JETSET v7.4 [98]. The estimated systematic error arising from assigning each ω decay product to the halo is given in Section 7.3.

The mechanism of the partial $U_A(1)$ restoration implies that the η' would have a decreased effective mass in the hot and dense medium [83]. The number of the created η' particles would then follow Eq. (7.1) with the modified mass and the freeze-out temperature respective to the η' mesons, and the fraction of η' mesons in the condensate is modeled with the

$$\frac{N_{\eta'}^*}{N_{\eta'}} = \left(\frac{m_{\eta'}^*}{m_{\eta'}} \right)^\alpha e^{-\frac{m_{\eta'}^* - m_{\eta'}}{T_{cond}}} \quad (7.3)$$

formula, where the T_{cond} is the temperature of the condensate.

As the escaping η' bosons are regaining their mass, they must lose momentum in order to fulfill the principle of energy conservation, i.e.

$$m_{\eta'}^{*2} + p_{T,\eta'}^{*2} = m_{\eta'}^2 + p_{T,\eta'}^2 \quad . \quad (7.4)$$

(In the above equation the quantities with an asterisk denote the properties of the in-medium η' , while the ones without an asterisk refer to the free η' . According to the kinematical setup of both PHENIX and STAR measurements [76, 77], the longitudinal component of the η' momentum is considered to be negligible here.) As a consequence, while η' bosons with $p_{T,\eta'}^* > \sqrt{m_{\eta'}^{*2} - m_{\eta'}^2}$ will follow the above distribution (with the effective mass $m_{\eta'}^*$ plugged in), the ones moving with a momentum less than this limit will be “trapped” in the medium until this medium is dissolved. Afterwards, η' -s from the condensate are given a random transverse momentum, following Maxwell-Boltzmann statistics with a characteristic temperature B^{-1} .

$$f(p_x, p_y) = \left(\frac{1}{2\pi m_{\eta'} B^{-1}} \right) e^{-\frac{p_x^2 + p_y^2}{2m_{\eta'} B^{-1}}} \quad , \quad (7.5)$$

³Other long-lived resonances, such as the ϕ meson, are checked to give a negligible contribution to the $\lambda_*(m_T)/\lambda_*^{\max}$ ratio, which translates to less than 2% uncertainty to the $m_{\eta'}^*$.

with $p_x^2 + p_y^2 = p_{T,\eta'}^2$. Note that B is a systematically varied model parameter, and its best value is determined by the analysis of the $\lambda_*(m_T)$ data.

7.2.1 Resonance models

The main source of systematic error is the choice of the resonance model. I have used a broad class of well-established resonance models in order to determine the extent of model dependence in this analysis. In this section I provide a brief description – both general and analysis specific – of the six different models used to simulate the number of each important resonance that decays into pions, as well as the number of primordial pions. The fractions of pions from different sources are compared to the total number of particles in Table 7.1. These values are fed into our simulations as an input. Note that not all core resonances are listed. With the assumption of a fixed $\langle u_T \rangle$, the $\lambda_*(m_T)$ is solely determined by the number of the halo resonances (ω , η , η' , K_S^0), and by the total number of pions. The primordial pions can replace those pions that come from fast decays without any effect on $\lambda_*(m_T)$. Generally, if a model contains a large number of exotic short lived resonances, it predicts less primordial pions.

Particles	Fractions from model						
	ALCOR	FRITIOF	Kaneta <i>et al.</i>	Letessier <i>et al.</i>	Stachel <i>et al.</i>	UrQMD	
primordial π^+	0.4910	0.2095	0.7396	0.3059	0.3333	0.2395	
short lived	ρ	0.1100	0.3058	0.0651	0.0259	0.0370	0.0045
	Δ		0.0846	0.0088	0.0080		0.0069
	K^*		0.1351	0.0124	0.0143		0.0014
	Σ		0.0153	0.0040	0.0017		0.0066
	Σ^*		0.0098	0.0054			0.0016
long lived	ω	0.1104	0.1023	0.0209	0.0233	0.0296	0.0073
	η	0.0453	0.0516	0.0602	0.0383	0.0360	0.0233
	η'	0.0067	0.0577	0.0089	0.0032	0.0031	0.0050
	K_S^0	0.0717	0.0283	0.0746	0.0601	0.0513	0.0287

Table 7.1. Resonance ratios from different models.

ALCOR [90]: Hadron multiplicities – especially for strange particles – are calculated in the framework of this algebraic coalescence rehadronization model, which counts for redistribution of quarks into hadrons for relativistic heavy-ion collisions. Resonance ratios were taken from recent calculations for the RHIC collisions [99]. Since the mass eigenstates of the strange-antistrange mesons are not directly

pinned down, the Kaneta-Xu [91] predictions were used to fix the $N_{\eta'}/N_{\eta}$ ratio for the ALCOR model.

FRITIOF [84] is a Monte Carlo program that implements the Lund string model for hadron-hadron, hadron-nucleus and nucleus-nucleus collisions. Resonance ratios were computed with the FRITIOF model by simulating of 1000 events using RHIC central Au+Au $\sqrt{s_{NN}} = 200$ GeV parameters. FRITIOF was excluded from examination when drawing the conclusions of this analysis, since it was unable to describe the STAR $\lambda_*(m_T)/\lambda_*^{\max}$ dataset, nor the combined STAR + PHENIX dataset, to a $CL > 0.1\%$ at any setup of the model parameters.

Kaneta-Xu [91]: In the case of this model, the following form of Eq. 1. of [91] was used⁴

$$\rho_i = \frac{2J_i + 1}{2\pi^2} T_{ch} m_i^2 K_2 \left(\frac{m_i}{T_{ch}} \right), \quad (7.6)$$

where m_i is the mass, J_i is the spin of the particle. $K_2(x)$ denotes the 2nd order modified Bessel function. For the sake of simplicity the temperature of the chemical equilibrium $T_{ch} = 160$ MeV, the strangeness saturation factor $\gamma^s = 1$, the quark potentials $\mu_q = 10$ MeV and $\mu_q = 0$ were considered, all in consistency with the measured PHENIX and STAR measurements in $\sqrt{s_{NN}} = 200$ GeV Au+Au collisions [2].

Letessier-Rafelski [92]: The model of these two authors studied soft hadron production in relativistic heavy ion collisions in a wide range of reaction energy, $4.8 \text{ GeV} < \sqrt{s_{NN}} < 200 \text{ GeV}$, and made predictions about yields of particles using the statistical hadronization model. Particle yields of the central events are from Table 4 of [92].

Stachel et. al [93]: This statistical “fireball” model treats the system as a grand canonical ensemble with the temperature and the baryon chemical potential as free parameters. Particle yields of the central events were taken from Sec. 2.2. Table 1 of [93].

UrQMD [94]: The Ultra-relativistic Quantum Molecular Dynamics model is a microscopic model used to simulate (ultra)relativistic heavy ion collisions in the energy range from Bevalac and SIS up to AGS, SPS and RHIC. Resonance ratios were computed with the UrQMD model by simulating 1000 events using RHIC central Au+Au $\sqrt{s_{NN}} = 200$ GeV parameters.

⁴The relative minuteness of μ_q in the referred equation guarantees that the charge factor is negligible for even those rare particles, where it is not exactly 0.

7.3 Results

I used different input models and setups to map the parameter space for a twofold goal.

- I excluded certain regions where a statistically acceptable fit to the data is not achievable, thus a lower limit could be given on the η' mass modification. I also provided the most probable value of the in-medium mass of the η' .
- In addition to the characterization of the in-medium η' mass modification, I determined the transverse momentum spectra of the η and η' mesons. These spectra may serve as controls and provide motivation for future measurements as well as an input for theoretical calculations that may go well beyond the scope of the present work.

I published these results in Ref. [73]. The analysis is briefly summarized in Ref. [74] and detailed in Ref. [75].

7.3.1 Reduction of the η' mass

Out of the six parameters of the η' spectrum and $\lambda_*(m_T)$ simulation, the two most important ones are B^{-1} and $m_{\eta'}^*$. As shown in Fig. 7.2, they directly determine the shape of the observed dip (depth and width, respectively). I considered these parameters as “fit variables”. I looked for the most probable values on a fine grid of $m_{\eta'}^*$ and B^{-1} using a simulation of the $\lambda_*(m_T)$ spectrum and then I determined the χ^2 from the fits to the data of the PHENIX and STAR measurements at each individual setup. I treated the other four parameters as “constants”, although their variation played a role when determining systematic errors. As a default setup I took the π^+ freeze-out temperature from PHENIX inverse slope parameter fit⁵ to be $T_{FO} = 177.0 \pm 1.2$ MeV [96], and I made the conservative assumption of $T_{cond} = T_{FO}$.⁶ The average

⁵Note that the values for T_{FO} and $\langle u_T \rangle$ only include the statistical errors. The systematics were taken into account in our systematic studies that involved a wide range of different predictions on T_{FO} , $100 \text{ MeV} \leq T_{FO} \leq 177 \text{ MeV}$.

⁶The temperature of the condensate majorates the freeze-out temperature. As can be seen from our systematic checks, a freeze-out temperature that is lower than the condensate temperature will move $m_{\eta'}$ downwards, i.e. towards “safety” for our conclusion.

transverse flow velocity was measured by PHENIX to be $\langle u_T \rangle = 0.48 \pm 0.07$ (in relativistic units) [96]. I cross-checked the value in simulations with a $0.40 \leq \langle u_T \rangle \leq 0.60$ scan with $\Delta \langle u_T \rangle = 0.01$ steps at the best value of $m_{\eta'}^*$ and B^{-1} , and I found that the most probable values were around $\langle u_T \rangle = 0.50$, in agreement with the PHENIX measurement. The polynomial exponent $\alpha = 0$ corresponds to a 2D expansion [41, 97], that had been proved to give a good description of data, used by PHENIX when obtaining $\langle u_T \rangle$ and T_{FO} . However the $\alpha = +1/2$ (1D) and $\alpha = -1/2$ (3D) cases were also examined as systematic checks.

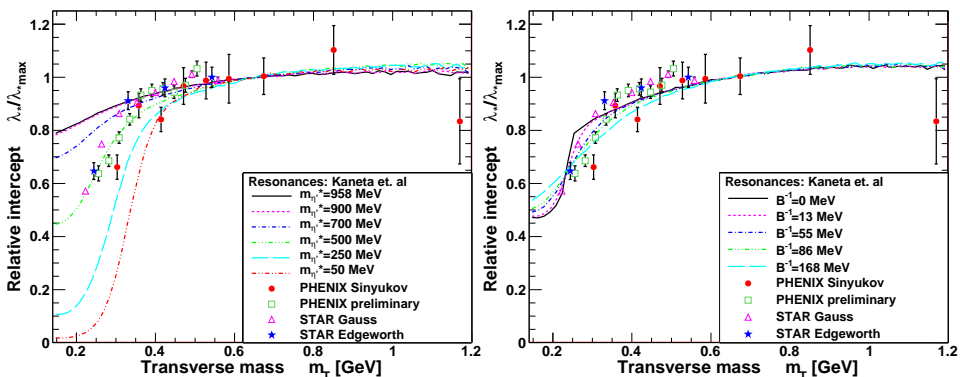


Figure 7.2. *Left:* Simulated $\lambda_*(m_T)/\lambda_*^{\max}$ spectra for different $m_{\eta'}^*$ values, B^{-1} fixed to its best fit value. *Right:* Simulated $\lambda_*(m_T)/\lambda_*^{\max}$ spectra for different B^{-1} values, $m_{\eta'}^*$ fixed to its best fit value. The resonance multiplicities of Ref. [91] and $\alpha = 0$, $T_{cond} = 177$ MeV, $T_{FO} = 177$ MeV, $\langle u_T \rangle = 0.48$ were used. All four datasets described in Sec. 7.1.3 are shown here for comparison purposes.

The (B^{-1}, m_T) plane was mapped on a grid of 21 non-equidistant steps⁷ for $0 \text{ MeV} \leq B^{-1} \leq 350 \text{ MeV}$, and by 10 MeV equidistant steps⁸ for the $10 \text{ MeV} \leq m_{\eta'} \leq 958 \text{ MeV}$ region. A good simultaneous description of PHENIX and STAR data was obtained by certain values of B^{-1} and m_T in the case of 5 out of the 6 models. In Figs. 7.3–7.7 I show the best $\lambda_*(m_T)/\lambda_*^{\max}$ fits, the results without the mass modification, and the confidence level (CL) maps on the $(m_{\eta'}^*, B^{-1})$ plain for these models. The $1\text{-}\sigma$ contours are summarized in Fig. 7.8

⁷In fact, $B^{-1/2}$ was mapped in 21 equidistant steps between 0 and 600 $\text{MeV}^{1/2}$.

⁸The $m_{\eta'}^*$ values are given with a resolution of 10 MeV throughout this chapter.

for the $\alpha = 0$ and the $\alpha = -1/2$ cases. In case of the FRITIOF model, no values of B^{-1} and $m_{\eta'}^*$ provided an acceptable fit. This model was therefore excluded from further studies. As expected, a strongly reduced η' mass results in a dip in the low- m_T part of the $\lambda_*(m_T)$ distribution (and the smaller the mass, the deeper the dip is), while B^{-1} steers the width of this dip through smearing the momentum, while the $\langle u_T \rangle$ parameter influences the overall slope of the $\lambda_*(m_T)$ spectrum at higher m_T . Such a role of $\langle u_T \rangle$ was already observed in [83], and it is not detailed here.

I computed the systematic uncertainties resulting from the lack of precise knowledge of model constants by varying these constants within the range that is given by different measurements: Spectra with values of $\alpha = -1/2$ and $\alpha = +1/2$ were investigated, as well as $T_{FO} = 100$ MeV, $T_{cond} = 140$ MeV and $T_{cond} = 220$ MeV, representing the boundaries of the theoretically or experimentally acceptable region of these parameters. Besides the choice of the model parameters, there are systematic uncertainties resulting from uncertainties on $\lambda_*(m_T)$:

- The STAR Edgeworth λ_* values were extracted from data of 0–5% centrality, compared to the 0–30% rapidity range of the PHENIX Sinyukov dataset. I estimate that this relative error does not exceed 9.8%. See details in Section 7.3.3.
- Although the ω may give part of its contribution to the tail at the resolution available in STAR and PHENIX, it was considered as part of the halo. This introduces a relative systematic error of 7% on the measured λ_* [40].
- Moving the pseudo-rapidity cutoff from $|y| < 0.36$ to $|y| < 0.50$ adds another error that is measured to be 3%.

These errors were considered independent and were added up quadratically. The relative error on $\lambda_*(m_T)/\lambda_*^{\max}$ corresponds to the same amount of relative error on $m_{\eta'}^*$ in the worst-case scenario⁹.

The best fit values and their error determinations are summarized in Table 7.2, while Table 7.3 shows the limits of acceptability, defined on the region, where $CL > 0.1\%$. The combined PHENIX and

⁹This relation was obtained from the STAR Edgeworth dataset with the Kaneta *et al.* [91] multiplicities: when lowest m_T data point was moved by 10% first up and then down, the fitted $m_{\eta'}^*$ value changed by the same relative error.

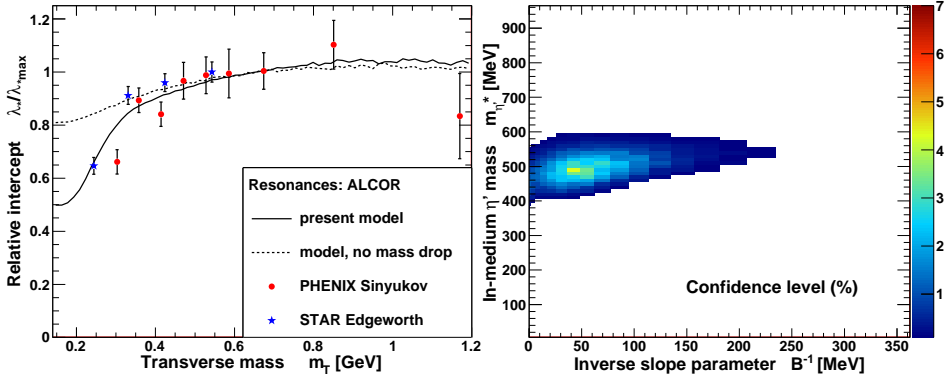


Figure 7.3. Left: $\lambda_*(m_T)/\lambda_*^{\max}$ spectrum of the PHENIX and STAR data points, in comparison with Monte Carlo simulations based on the ALCOR model [90] at parameters from the best fit ($B^{-1} = 42$ MeV, $m_{\eta'}^* = 490$ MeV), for $\alpha = 0$, $T_{cond} = 177$ MeV, $T_{FO} = 177$ MeV and $\langle u_T \rangle = 0.48$. Right: Corresponding confidence level surface on the $(B^{-1}, m_{\eta'}^*)$ plain. Only the region with acceptable fits ($CL > 0.1\%$) is shown.

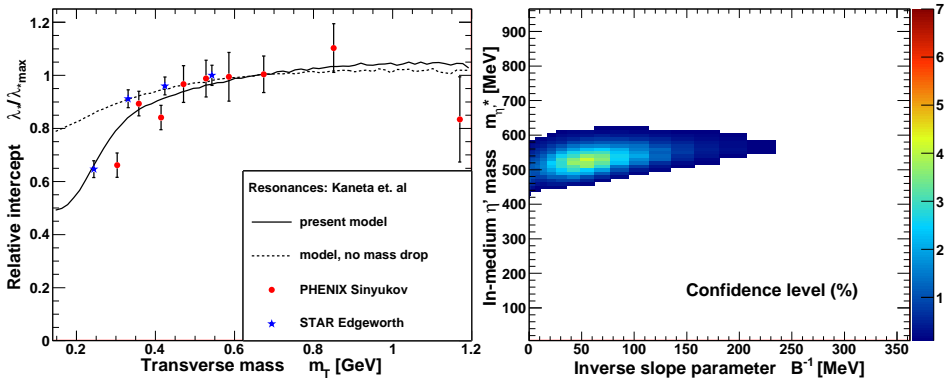


Figure 7.4. Results for the combined STAR+PHENIX dataset with resonance multiplicities from the model of Kaneta *et al.* [91]. Explanation of the panels and other parameters are the same as in Fig. 7.3. Best fit is at $B^{-1} = 55$ MeV, $m_{\eta'}^* = 530$ MeV.

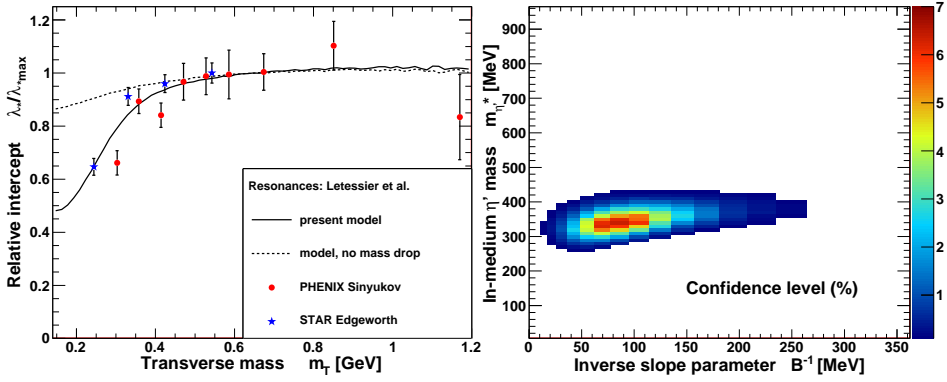


Figure 7.5. Results for the combined STAR+PHENIX dataset with resonance multiplicities from the model of Letessier *et al.* [92]. Explanation of the panels and other parameters are the same as in Fig. 7.3. Best fit is at $B^{-1} = 86$ MeV, $m_{\eta'}^* = 340$ MeV.

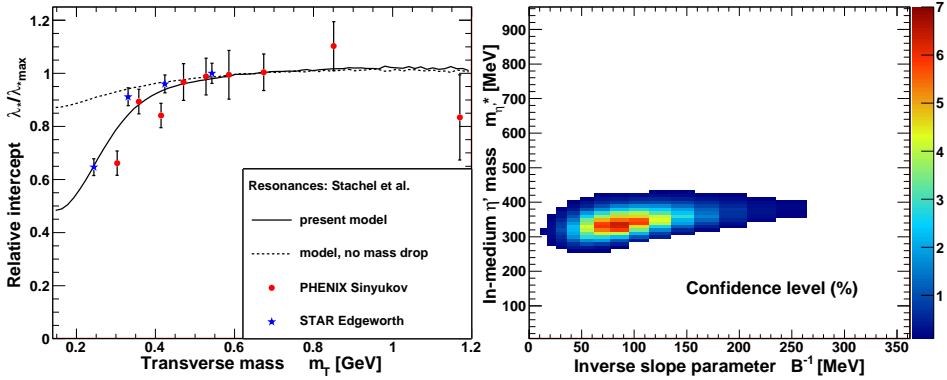


Figure 7.6. Results for the combined STAR+PHENIX dataset with resonance multiplicities from the model of Stachel *et al.* [93]. Explanation of the panels and other parameters are the same as in Fig. 7.3. Best fit is at $B^{-1} = 86$ MeV, $m_{\eta'}^* = 340$ MeV.

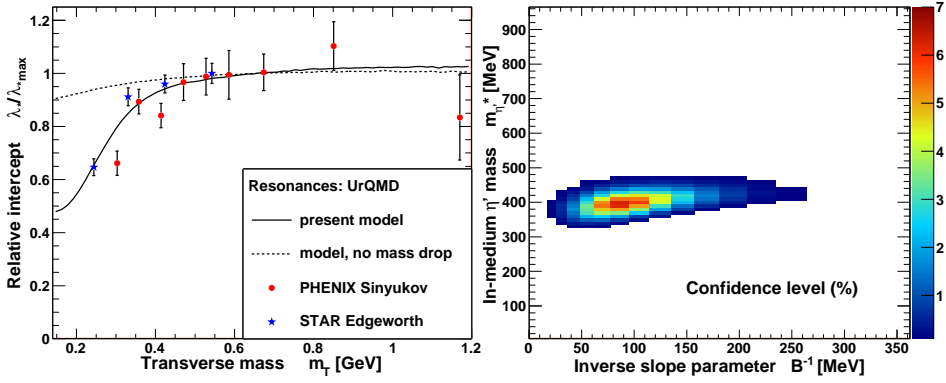


Figure 7.7. Results for the combined STAR+PHENIX dataset with resonance multiplicities from the UrQMD model [94]. Explanation of the panels and other parameters are the same as in Fig. 7.3. Best fit is at $B^{-1} = 86$ MeV, $m_{\eta^*} = 400$ MeV.

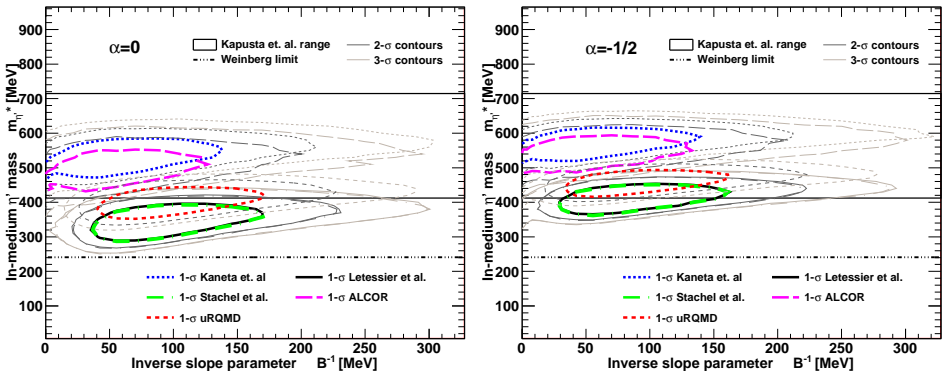


Figure 7.8. *Left:* Standard deviation contours on the (B^{-1}, m_{η^*}) plain, obtained from $\lambda_*(m_T)/\lambda_{*max}$ of MC simulations for $\alpha = 0$, $T_{FO} = T_{cond} = 177$ MeV and $\langle u_T \rangle = 0.48$, based on different chemical freeze-out models, each fitted to the PHENIX and STAR combined dataset. The framed band indicates the theoretically predicted range of 412 MeV–715 MeV [71], while the horizontal dashed-dotted line at 241 MeV indicates Weinberg's lower limit [100]. *Right:* Same for $\alpha = -1/2$.

STAR data could not be described unless a significant η' mass modification was assumed, $m_{\eta'}^* < 680$ MeV. Although this value includes the systematics from the model uncertainties, it is also subject to the uncertainties coming from the other sources listed above¹⁰. On the basis of model simulations, studies and systematic checks, I found that a description of the combined PHENIX and STAR data set is possible with $CL > 0.1\%$ only if an in-medium η' mass modification of $\Delta m_{\eta'}^* > 200$ MeV was utilized. In other words, $\Delta m_{\eta'}^* > 200$ MeV at the 99.9 % confidence level, corresponding to a more than 5- σ effect, in the considered broad model class.

7.3.2 The enhanced η' and η spectrum

The dilepton spectrum has been measured recently in minimum bias Au+Au collisions at $\sqrt{s_{NN}} = 200$ GeV, and a large enhancement was observed in the low invariant mass region $m_{ee} < 1$ GeV [10]. Low transverse mass enhancement of the η' and η production results in dilepton enhancement just in the considered kinematic range [71]. PHENIX recently reported a two-component transverse momentum spectrum in dilepton channel direct photon measurements [10]. The η' and η spectra reconstructed here may serve as an input e.g. for the simulations and evaluations of the dilepton spectra instead of the currently utilized η' spectra, based on m_T scaling and hence not providing the possibility of taking into account an η' mass reduction.

The transverse momentum spectra of the η' and η mesons extracted from the mid-rapidity BEC measurements allow for a cross-check of the $m_{\eta'}^*$ reduction scenario that is based on the non-pionic decay channels of the η' . I computed the η' and η spectra for each of the successful resonance models two different ways. First I used the original $m_{\eta'} = 958$ MeV value. The obtained spectra clearly show the m_T -scaling. Thereafter I used the reduced η' mass and the corresponding B^{-1} value that provided the best description of the data in the frame of a given resonance model. These spectra break the m_T -scaling with an additional, steeper exponential-like component over the original η' spectrum, and produce most of the η' enhancement in the low- p_T region. The original “non-enhanced” spectra were normalized to the η'

¹⁰I determined these errors at the best mass fits, and applied the same absolute value in case of the mass limits. This is a conservative method since the higher the mass value is, to the lesser extent it is influenced by the same effect.

Dataset	Model Fits to PHENIX+STAR data					Parameters		
	ALCOR [90]	Kaneta <i>et al.</i> [91]	Letessier <i>et al.</i> [92]	Stachel <i>et al.</i> [93]	UrQMD [94]	α	T_{cond}	T_{FO}
$m_{\eta'}^*$ (MeV)	490 ⁺⁶⁰ ₋₅₀	530 ⁺⁵⁰ ₋₅₀	340 ⁺⁵⁰ ₋₆₀	340 ⁺⁵⁰ ₋₆₀	400 ⁺⁵⁰ ₋₄₀	0	177	177
B^{-1} (MeV)	42	55	86	86	86			
CL (%)	4.29	4.12	6.35	6.38	6.28			
χ^2/NDF	1.83	2.07	1.72	1.71	1.72			
$m_{\eta'}^*$ (MeV)	540 ⁺⁵⁰ ₋₄₀	560 ⁺⁶⁰ ₋₃₀	410 ⁺⁴⁰ ₋₄₀	410 ⁺⁴⁰ ₋₄₀	460 ⁺⁴⁰ ₋₄₀	-0.5	177	177
B^{-1} (MeV)	55	55	86	86	86			
CL (%)	2.80	3.35	6.07	5.97	6.14			
χ^2/NDF	1.96	2.07	1.73	1.73	1.73			
$m_{\eta'}^*$ (MeV)		470	210			+0.5	177	177
B^{-1} (MeV)		55	86					
CL (%)		4.58	6.54					
χ^2/NDF		1.82	1.71					
$m_{\eta'}^*$ (MeV)		620	460			0	140	177
B^{-1} (MeV)		42	69					
CL (%)		2.26	5.86					
χ^2/NDF		2.02	1.74					
$m_{\eta'}^*$ (MeV)		440	200			0	220	177
B^{-1} (MeV)		69	104					
CL (%)		5.61	6.33					
χ^2/NDF		1.75	1.72					
$m_{\eta'}^*$ (MeV)		410	240			0	177	100
B^{-1} (MeV)		145	145					
CL (%)		1.63	1.80					
χ^2/NDF		2.11	2.09					

Table 7.2. Fitted values of the modified η' mass on the STAR+PHENIX combined dataset, for different resonance models and parameters. The FRITIOF model has $CL < 0.1\%$ and therefore it is not shown here. The statistical errors are given by the $1\text{-}\sigma$ boundaries of the fits, determined only for $m_{\eta'}^*$ and for the $\alpha = 0$ and $\alpha = -0.5$ simulations. Best $m_{\eta'}^*$ and B^{-1} parameters for various systematic checks are shown in the last 4 rows.

multiplicity¹¹ predicted by Kaneta *et al.* [91], and then the enhanced spectra was scaled relative to it. Left panel of Fig. 7.9 shows both the original, m_T -scaling spectra, and the enhanced version with $m_{\eta'}^* < m_{\eta'}$ for the resonance ratios of Ref. [91]. A comparison of enhanced η' spectra of all resonance models is given on the right panel of Fig. 7.9, and the fitted spectrum parameters are listed in Table 7.4 together with the

¹¹The normalization of the original spectra was performed the following way: First the numerical integral of the unmodified $\frac{1}{m_T} \frac{dN}{dm_T}$ distribution was computed. Then the average number of η' mesons per event was divided by this integral, and the histogram was scaled by the resulting number.

Dataset	Acceptability boundaries of model fits						Parameters		
	ALCOR [90]	FRITIOF [84]	Kaneta <i>et al.</i> [91]	Letessier <i>et al.</i> [92]	Stachel <i>et al.</i> [93]	UrQMD [94]	α	T_{cond}	T_{FO}
PHENIX	0–750	680–958	0–720	0–510	0–500	0–530	0	177	177
STAR	380–600	none	430–630	190–450	190–450	260–500			
PHENIX+STAR	380–590	none	420–620	260–430	260–430	330–470			
PHENIX	30–770	420–958	50–730	0–540	0–540	0–560	-0.5	177	177
STAR	470–630	none	500–650	300–500	300–500	360–540			
PHENIX+STAR	450–620	670–760	490–640	340–480	340–480	400–510			
PHENIX			0–690	0–450			+0.5	177	177
STAR			320–610	0–390					
PHENIX+STAR			340–590	0–390					
PHENIX			0–760	0–450			0	140	177
STAR			560–690	0–390					
PHENIX+STAR			540–680	0–360					
PHENIX			0–680	0–410			0	220	177
STAR			270–580	0–350					
PHENIX+STAR			290–560	100–320					
PHENIX			220–470	30–310			0	177	100
STAR			360–470	190–300					
PHENIX+STAR			370–440	200–280					

Table 7.3. Acceptability boundaries of the modified η' mass on the PHENIX, STAR, and the combined PHENIX+STAR datasets, for different resonance models and parameters. A fit is considered acceptable if $CL \geq 0.1\%$. FRITIOF fails completely on the STAR dataset and also on the combined PHENIX+STAR data. All the other models require an $m_{\eta'}^* \leq 640$ MeV excluding systematics. Acceptability boundaries for various systematic checks are shown in the last 4 rows.

η' enhancement factors for each particular model of resonance ratios.

Since the spectrum of the η mesons can be directly compared to measured data, it serves as a consistency check by itself. A comparison of enhanced η spectra of all resonance models is given on Fig. 7.10 (left), and the fitted spectrum parameters are listed in Table 7.5. A connection between the η' enhancement and the η enhancement can be expressed as

$$\frac{N_{\eta}^*}{N_{\eta}} = 1 + \left(\frac{N_{\eta'}^*}{N_{\eta'}} - 1 \right) \frac{N_{\eta'}}{N_{\eta}} BR(\eta' \rightarrow \eta + \pi\pi) \quad (7.7)$$

with the last term, the total η' to η branching ratio being approximately 65.7 %. For models [90–93] I also plotted the absolutely normed η spectra in Fig. 7.10 (right) compared to the measured PHENIX η spectra. It is obvious from the plot that the computed enhancement affects only the $m_T < 1$ GeV part of the η spectrum.

Considering all errors, $6.01 \leq N_{\eta'} \leq 258$ and $1.56 \leq N_{\eta} \leq 15.4$.¹²

¹²The upper bounds on $N_{\eta'}$ and N_{η} were calculated the following way: The $(B^{-1}$,

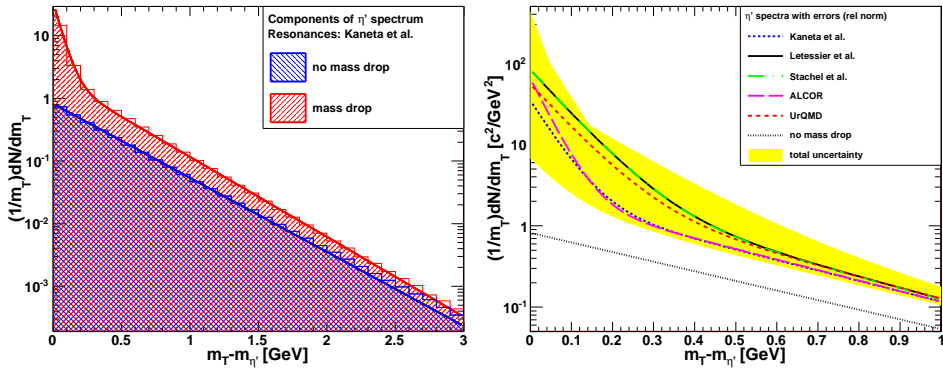


Figure 7.9. *Left:* Reconstructed m_T spectrum of the η' mesons using the resonance ratios of Ref. [91]. Lower (blue) part indicates the scenario without in-medium η' mass reduction, upper (red) part the enhancement required to describe the dip in the low m_T region of λ_* . *Right:* Comparison of reconstructed m_T spectra of the η' mesons from different models. All spectra are normalized to the η' multiplicity as given by the model of Kaneta and Xu [91], and then fitted with a double exponential. The yellow band represents the total error. The fit parameters are summarized in Table 7.4. Above $m_T - m_{\eta'} = 1$ GeV, all models result in very similar values, corresponding to an approximate m_T -scaling. This figure indicates that the violation of this m_T -scaling is model dependent, and suggests that dilepton measurements may provide additional constraints for the model builders.

Resonance model	a	b	c	d	η' enhancement
No enhancement	0.82	2.72	0 (fixed)	0 (fixed)	-
ALCOR [90]	2.30	2.98	62.4	23.5	43.4
Kaneta <i>et al.</i> [91]	2.21	2.94	32.4	18.7	25.6
Letessier <i>et al.</i> [92]	2.91	3.14	80.1	12.8	67.6
Stachel <i>et al.</i> [93]	2.85	3.13	80.0	12.8	67.6
UrQMD [94]	2.75	3.07	52.5	12.7	45.0

Table 7.4. η' enhancement and fit parameters of the spectra for different models of resonance abundances. The spectra are obtained using the most probable B^{-1} , $m_{\eta'}^*$ parameters, and then fitted with a double exponential function $y = ae^{-b(m_T - m_{\eta'})} + ce^{-d(m_T - m_{\eta'})}$. The yellow band represents the total error. The spectrum without enhancement is computed with the Kaneta *et al.* [91] resonance ratios, with $m_{\eta'}^* = m_{\eta'}$.

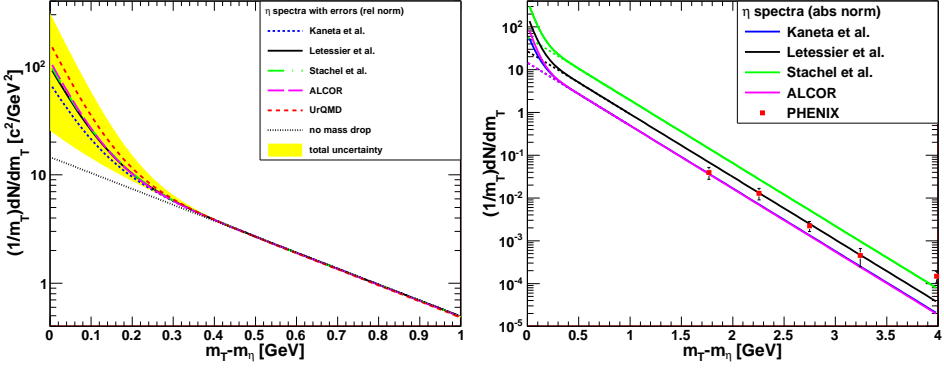


Figure 7.10. Comparison of reconstructed m_T spectra of the η mesons from different models. *Left:* All spectra are normalized to the η' multiplicity as given by the model of Kaneta and Xu [91], and then fitted with a double exponential. The fit parameters are summarized in Table 7.5. Above $m_T - m_{\eta'} = 1$ GeV, all models result in very similar values, corresponding to an approximate m_T -scaling. *Right:* Absolute normalized spectra from input models [90–93] are compared to PHENIX 200 GeV central Au+Au collision measurements.

Resonance model	a	b	c	d	η enhancement
No enhancement	14.6	3.38	0 (fixed)	0 (fixed)	-
ALCOR [90]	14.6	3.40	97.0	17.8	5.25
Kaneta <i>et al.</i> [91]	14.6	3.38	54.9	16.2	3.47
Letessier <i>et al.</i> [92]	14.6	3.38	84.1	16.9	4.75
Stachel <i>et al.</i> [93]	14.5	3.38	89.2	17.0	4.97
UrQMD [94]	14.6	3.41	148	17.9	7.49

Table 7.5. η enhancement and fit parameters of the spectra for different models of resonance abundances. The spectra are obtained using the most probable B^{-1} , $m_{\eta'}^*$ parameters, and then fitted with a double exponential function $y = ae^{-b(m_T - m_{\eta'})} + ce^{-d(m_T - m_{\eta'})}$. The spectrum without enhancement is computed with the Kaneta *et al.* [91] resonance ratios, with $m_{\eta'}^* = m_{\eta'}$.

Estimations using these enhancement factors indicate that the observed in-medium η' mass drop is indeed a promising candidate to explain this dilepton excess [74].

7.3.3 System size, energy and centrality dependence

The STAR Edgeworth $\lambda_*(m_T)$ data are given for the 0–5% most central data, while PHENIX carried out the pion correlation analysis on the 0–30% centrality range. The behavior of the $\lambda_*(m_T)$ curve is not necessarily the same for different centrality classes, resulting in a systematic error in our analysis. This effect could be estimated using the centrality dependent Gaussian λ measurement provided by STAR. The $\lambda(m_T)/\lambda_{max}$ values for the centrality classes between 0% and 30% are summarized in Fig. 7.11. As a conservative estimation, the relative error on $m_{\eta'}^*$ caused by the different centrality classes is determined to be less than 9.8%.¹³ According to this centrality and transverse mass dependent Gaussian STAR data on the intercept parameter, the depth of the low- m_T dip deepens in the case of more central collisions. This suggests that the restoration of the $U_A(1)$ symmetry is more complete in case of more central collisions. However, a quantitative analysis would require experimental data on the more relevant Edgeworth $\lambda_*(m_T)$ data in different centrality classes.

System size and energy dependence is shown on Fig. 7.11, where $\lambda(k_T)/\lambda_{max}$ values from NA44 Pb+Pb, STAR Au+Au and Cu+Cu collisions are compared. The plot indicates that the mass modification effect seems to be maximal in 200 GeV Au+Au collisions, followed by 62 GeV Au+Au collisions, 200 GeV Cu+Cu and 62 GeV Cu+Cu in that order. Although in each of the STAR cases a positive signal is apparent, we also observe the lack of saturation of $\lambda(k_T)/\lambda_{max}$ at higher

$m_{\eta'}^*$) values of all above mentioned setups of input model, α , T_{FO} , T_{cond} were considered along the $1-\sigma$ contour, and then the $m_{\eta'}^*$ value was shifted upwards with the corresponding non-model-dependent systematic error. Then the η' (or η) spectra were plotted for these $(B^{-1}, m_{\eta'}^*)$ pairs, and the one corresponding to the maximum enhancement was considered. The lower bound was computed similarly, with the $m_{\eta'}^*$ values shifted downwards and the spectra with the minimal enhancement taken. The maximal enhancement is given by Ref. [92], while the minimal is by Ref. [91]. (Ref. [84] is not considered as FRITIOF fails to describe the STAR and the combined PHENIX and STAR data sets.)

¹³This is given by the the difference of the 1st $\lambda(m_T)/\lambda_{max}$ data points of the 0–5% w.r.t. the 20–30% centrality classes.

momenta, which can be attributed to the decreasing radial flow with decreasing energy and system size. Such a dependence on the amount of the radial flow has been first pointed out in Ref. [83]. Detailed analysis of the STAR and PHENIX data set taken in 2010 at RHIC at 7.7, 11.5, 39, and 62.4 GeV energies will allow for the investigation of the onset of the observed η' mass drop effect.

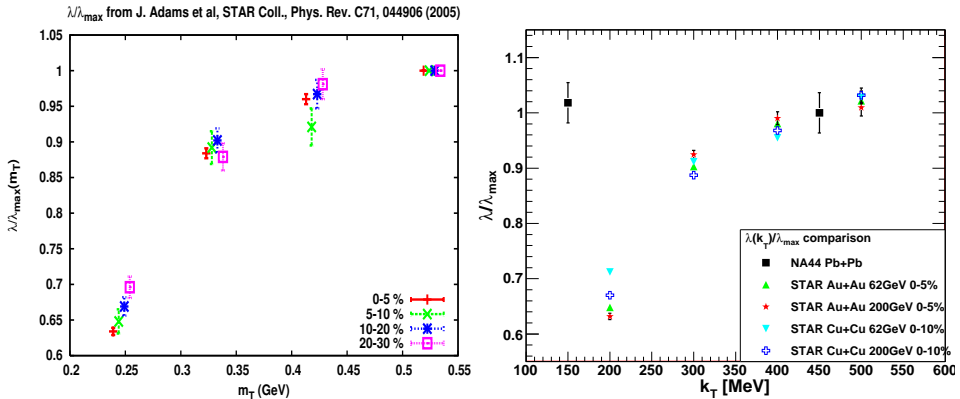


Figure 7.11. *Left:* STAR HBT Gaussian $\lambda(m_T)/\lambda_{max}$ values for different centrality classes between 0% and 30%. The points with different centralities were measured in the same m_T intervals, but are slightly shifted to left and right on this Figure for a better visibility. Note the trend that more central data correspond to a larger hole in the lowest transverse mass bin, suggesting a slightly larger in-medium η' mass decrease in more central collisions. This effect is part of the systematic errors given in the conclusions. *Right:* STAR Gaussian $\lambda(k_T)/\lambda_{max}$ values for different systems and energies, compared to SPS measurements.

7.4 Conclusion

The best simultaneous description of STAR and PHENIX HBT data is achieved with an η' mass that is dramatically reduced from 958 MeV to $340^{+50+280}_{-60-140} \pm 42$ MeV in the medium created in central Au+Au collisions at RHIC. The first error here is the statistical one from the fit, the second error is from the model and parameter choices, while the third is the systematics from the centrality selection, the resolvability of ω decay products and the pseudo-rapidity cutoff. Note that

the dominant error corresponds to the selection of the model for the hadronic multiplicities.

The best estimated value for the modified η' mass does not differ significantly from the range of 412 MeV – 715 MeV, predicted by the quark model calculations for the $U_A(1)$ symmetry restoration [71]. In fact, it is slightly below this range, but above the lower limit of $\sqrt{3}m_\pi$ by Weinberg [100]. Hence the mass reduction effect seems to be already at maximum at $\sqrt{s_{NN}} = 200$ GeV central Au+Au collisions. As a consequence, one may expect a saturation of this effect if the bombarding energy is further increased up to LHC energies of $\sqrt{s_{NN}} = 10$ TeV. In Section 7.3.3 an interesting centrality dependence of the order of 9.8 % is noted, which suggests that the in-medium η' mass drop is slightly larger in more central collisions and that more detailed centrality and transverse mass dependent measurements of the Edgeworth and other model-independent estimates of the extrapolated intercept parameter λ_* are necessary to pin down this effect. At present the centrality dependence is part of the above given 42 MeV systematic error.

Not only did I investigate the best value for the in-medium mass of η' , but also the minimum mass modification that is required to describe the data. Based on the combined STAR and PHENIX data, and from the systematic investigation of various resonance multiplicities and model parameters, it can be concluded that in $\sqrt{s_{NN}} = 200$ GeV central Au+Au reactions the mass of the η' meson is reduced by more than 200 MeV, at the 99.9 % confidence level in the considered model class [73–75]. A similar analysis of NA44 S+Pb data at top CERN SPS energies provided no evidence of an in-medium η' mass modification [83].

These positive results on a significant, indirectly observed in-medium η' mass modification, should revitalize theoretical interest in other signatures of partial $U_A(1)$ and chiral symmetry restoration in heavy ion reactions and also should be cross-checked against other observables like the enhancement of low-mass dileptons and photons in the same reactions. More detailed and more precise experimental data are needed on the intercept parameter of Bose–Einstein correlations of pions at low p_T at various bombarding energies, system sizes and centralities to fully understand the nature of partial $U_A(1)$ symmetry restoration. Detailed analyses of other decay channels of the η' and η mesons, e.g. dilepton measurements are required to confirm our observations on the onset of this effect.

Summary

RHIC operations started in 2000 and during the past decade, our understanding about the medium behavior of strong interactions radically changed. In my thesis I summarize the context and the main milestones of RHIC achievements that culminated in the official announcement of the discovery of the perfect fluid in 2005 and the strongly interacting Quark Gluon Plasma in February 2010. I give an overview of the accelerator complex, with focus on the PHENIX experiment in which I participate. I present my work in the field of high energy heavy ion collisions. I cover several subfields including Bose-Einstein correlation measurements of the bulk matter in PHENIX and connected theoretical work, as well as PHENIX measurements of soft and hard photon and hadron properties. Although these results are interesting on their own, they also provide elements to the new picture that has emerged from the 1st decade of RHIC operation.

During my PhD studies I contributed to the Experiment at several levels from detector calibration, operation, software development and maintenance to the preparation of scientific publications. The thesis points listed below summarize my most important new scientific contributions.

1. Calibration of the PHENIX Electromagnetic Calorimeter

I have calibrated the time of flight measurements in the PHENIX Electromagnetic Calorimeter for the data collected in 2005 Cu+Cu, 2006 p+p and 2007 Au+Au collisions. Prior to this calibration PHENIX used to determine the energy dependence of the timing signal with showers simulated in the detector units by laser impulses, which was not satisfactory in precision. I developed a new method that determines the time-energy dependence using solely real collision data, thus making the time of flight reconstruction more reliable. I maintained

and developed the calorimeter reconstruction software, and prepared a package for online preliminary calibration of the PbSc timing that is operational from 2006 on [22]. The results of these calibrations are used in the energy dependent nuclear modification factor measurements of neutral pions with high transverse momenta [30], among others.

2. Selection of neutral pions with stochastic cuts

I developed a method for the identification of particles in the PHENIX Electromagnetic Calorimeter, using d+Au collision data taken in 2003. This fuzzy logic based, *stochastic* cut proved to be more efficient than any previous calorimeter-based particle identification method. My method is not only useful in selecting electromagnetic particles (therefore in the reconstruction of neutral pions and direct photons), but also for selecting hadrons such as antineutrons [25]. I verified the optimality of the results with an artificial neural network analysis. I participated in the PHENIX workgroup that applied this method e.g. for determining the *neutral pion* spectra in $\sqrt{s_{NN}} = 200$ GeV Au+Au collisions [31].

3. Simulation verification and direct photon production

I have systematically analyzed the PbSc and PbGl detector response from 2002 Au+Au and 2003 d+Au collision data and carried out the corresponding *simulation verification* studies [33]. These simulations contributed significantly for the determination of the neutral pion and *direct photon* spectra created in PHENIX $\sqrt{s_{NN}} = 200$ GeV Au+Au collisions [37], published in [2].

4. PHENIX images and THERMINATOR simulations

I showed that THERMINATOR simulations, which focus on the correct handling of resonance decays, are able to reproduce the transverse momentum and centrality dependence of the one dimensional pion source observed in PHENIX $\sqrt{s_{NN}} = 200$ GeV Au+Au collisions. I pointed out that THERMINATOR is not able to describe the direction-dependently measured PHENIX source functions. This suggests that the heavy tail observed in the PHENIX pion correlation measurements cannot be explained only by resonance decays [50, 51].

The heavy, power-law-like tail seen in one-dimensional pion source functions can, however, be explained by considering the anomalous diffusion of hadrons. I pointed out that a possible comparison of the π^\pm , K^\pm and p^\pm source function shapes can differentiate between effects of resonance decays and anomalous diffusion [51]. With the PHENIX K^\pm - K^\pm correlation measurements we have shown that the power-law tail is stronger in the kaon than the pion source image, even though there are less resonances resulting in kaons. Thus we demonstrated that the main reason of the power-law tails observed in PHENIX source images cannot be the resonance decays [52].

5. Observation of an η' mass reduction in a hot, dense medium

The axial, $U_A(1)$ part of the $U(3)_L \times U(3)_R$ chiral symmetry group of the strong interaction is broken in the physical vacuum. According to theoretical considerations, however, the $U_A(1)$ symmetry is partially restored in a hot and dense medium. As a consequence, the mass of the η' meson reduces from its vacuum value of 958 MeV and takes a value near to the mass of the other pseudo-scalar mesons. I modeled this effect with thermal simulations, and I found that the like-sign pion Bose–Einstein correlation data measured in RHIC 200 GeV Au+Au collisions can be explained only if one assumes that the mass of the η' drops with at least 200 MeV at the 99.9% confidence level [73]. The most probable value is $m_{\eta'}^* = 340_{-60}^{+50} {}_{-140}^{+280} \pm 42$ MeV, where the errors are statistical, model and systematic respectively [74, 75]. I verified that the measured data was not reproducible in non-thermal models which do not assume a mass modification.

6. Spectra of the η' and η mesons in 200 GeV RHIC collisions

I determined the most probable spectra of the η' and η mesons created in the hot and dense medium. The other consequence of the symmetry restoration is that the η' and η spectra will differ from the naïve expectations. Besides the enhancement of the η' production the shape of its spectrum will also change: Low momentum η' mesons emerge in a high number, thus breaking the m_T -scaling. The spectrum of the η (one main decay product of the η') will also show a low-momentum enhancement, while its high-momentum part remains unchanged [74, 75].

Összegzés

A RHIC 2000-ben kezdte meg működését, és az elmúlt évtized során az erős kölcsönhatás közegbeli működéséről alkotott képünk gyökeresen megváltozott. Dolgozatomban az elméleti háttér ismertetésével összefoglalom a főbb RHIC eredményeket, amelyek elvezettek a tökéletes folyadék felfedezésének 2005-ös, és az erősen kölcsönható kvark–gluon plazma 2010. februári hivatalos bejelentéséhez. Ismertetem a RHIC gyorsítókomplexumot, nagy hangsúlyt fektetve a PHENIX kísérletre, amelyben részt veszek. A nagyenergiás nehézionfizika területén végzett munkám a forró maganyag Bose–Einstein korrelációs analízise, valamint a PHENIX-ben észlelt fotonok és hadronok spektrumainak meghatározására terjed ki. Bár ezen eredményeim önmagukban is érdekesek, legfőbb jelentőségük az, hogy hozzájárulnak a RHIC működése során kialakuló új összkép jobb megértéséhez.

PhD. tanulmányaim során a detektor üzemeltetésétől, kalibrációjától kezdve a kísérlet szoftverének karbantartásán és fejlesztésén keresztül a tudományos publikációk előkészítéséig a kísérleti munkának számos szintjében vettem részt. Legfontosabb új tudományos eredményeim az alábbi tézispontokban foglalom össze.

1. A PHENIX elektromágneses kaloriméterének kalibrációja

Elvégeztem a PHENIX elektromágneses kaloriméterének repülésiidő-kalibrációját a 2005. adatgyűjtési időszak $\text{Cu}+\text{Cu}$, a 2006. év $p+p$ és a 2007. év $\text{Au}+\text{Au}$ ütközéseire. Az időjel energiafüggését a PHENIX kísérletben korábban a detektoregységekbe juttatott lézimpulzusokkal szimulált záporok segítségével határoztuk meg, azonban ez nem volt kiélegítő pontosságú. Kifejlesztettem egy módszert, amely az idő–energia függést valós ütközések adataiból határozza meg, ezzel megbízhatóbbá téve a részecskék repülési idejének rekonstrukcióját. Továbbfejlesztettem és karbantartottam a kaloriméter rekonstrukciós szoftvercső-

magját, és létrehoztam egy az adatgyűjtés során azonnal lefutó, előzetes kaloriméter-kalibrációt készítő szoftvert, amely a 2006. évtől kezdve üzemel [22]. A kalibráció eredményét többek között a nagy transzverzális impulzusú semleges pionok nukleáris módosulási tényezőjére jellemző energiafüggés meghatározásában használtuk fel [30].

2. Semleges pionok szelekciója sztochasztikus vágással

Kifejlesztettem egy a PHENIX kísérlet elektromágneses kaloriméterében észlelt részecskék azonosítására irányuló, a fuzzy logikán alapuló módszert a 2003-as évben mért d+Au ütközések adatai alapján. Ez az ún. *sztochasztikus vágás* minden korábbinál hatékonyabbnak bizonyult. A módszerem az elektromágnesesen kölcsönható részecskék azonosításán (így a semleges pionok és a direkt fotonok spektrumának mérésén) túl hadronok, pl. antineutronok kiválasztására is alkalmas [25]. Az eredmény optimális voltát mesterséges neurális hálós analízissel ellenőriztem. Részt vettem annak a PHENIX munkacsoportnak a tevékenységében, amelyik ezt a módszert a $\sqrt{s_{NN}} = 200$ GeV-es Au+Au ütközéseiben észlelt *semleges pionok* spektrumának meghatározására alkalmazta [31].

3. A szimuláció verifikációja és a direkt fotonok spektruma

Elvégeztem a PHENIX ólom-szcintillátor és ólomüveg kaloriméteréből származó válaszjelek szisztematikus analízisét a 2002-es évben mért Au+Au ütközések adatain a vonatkozó *szimulációk verifikációját* [33]. Ezzel lényegesen hozzájárultam a PHENIX $\sqrt{s_{NN}} = 200$ GeV-es Au+Au ütközéseiben észlelt semleges pionok és a *direkt fotonok* spektrumainak meghatározásához [37], amiket a [2] hivatkozásban publikáltunk.

4. PHENIX források és THERMINATOR szimulációk

Megmutattam, hogy a rezonanciabomlások helyes kezelésére fókuszáló THERMINATOR szimulációk segítségével a PHENIX egydimenziós pionforrás-leképezésének transzverzális impulzustól és centralitástól való függése reprodukálható. A forráseloszlás hatványfüggvény-jellegű lecsengését ezekben szimulációkban a különböző bomlásidejű rezonanciák eloszlásával lehet megmagyarázni. Megmutattam továbbá, hogy a THERMINATOR nem képes leírni az irányfüggően mért PHENIX

forrásfüggvényeket. Ez arra utal, hogy a rezonanciák bomlásai önmagukban nem adnak kielégítő magyarázatot a forrás tapasztalt szerkezetére [50, 51].

Az egydimenziós pion-forrásfüggvények hatványfüggvényszerű lecsengését a rezonanciákon kívül a hadronok anomális diffúziójának figyelembe vétele segítségével is értelmezni lehet. Észrevettem, hogy a π^\pm , K^\pm és p^\pm forrásfüggvények közti eltérések különbséget tehetnek az anomális diffúzióból és a rezonanciabomlásból származó hatások között. A PHENIX K^\pm - K^\pm korrelációs mérésében kimutattuk, hogy a kaonok forrásfüggvényében a lecsengő rész súlya nagyobb, mint a pionokéban, holott kaonokra kevesebb rezonancia bomlik. Ezzel megmutattuk, hogy nem a lassan bomló rezonanciák okozzák a forrásfüggvény hatványfüggvény-jellegű lecsengését [51, 52].

5. Az η' mezon forró, sűrű közegben való tömegcsökkenése

A fizikai vákuumban az erős kölcsönhatás $U(3)_L \times U(3)_R$ királis szimmetriacsoportjának axiális, $U_A(1)$ része sérül. Elméleti megfontolások szerint azonban sűrű, forró közegben az $U_A(1)$ szimmetria részben helyreáll, aminek következménye, hogy az η' mezon tömege a 958 MeV-es vákuumbeli értékéről a többi pszeudoskalár mezon tömegének közelébe csökkenhet. Termikus szimulációk segítségével modelleztem ezt az effektust, és megállapítottam, hogy a RHIC 200 GeV-es arany-arany ütközéseiben mért adatok egy széles modellosztály keretein belül csak úgy magyarázhatóak, ha az η' mezonok tömege legalább 200 MeV-vel lecsökken [73], 99.9% konfidenciaszint mellett. A legvalószínűbb érték $m_{\eta'}^* = 340_{-60}^{+50} {}_{-140}^{+280} \pm 42$ MeV (A hibák rendre statisztikus, modellfeltevésen alapuló, illetve egyéb szisztematikus hibák.) [74, 75]. Ellenpróbaként ellenőriztem, hogy nem termikus, tömegcsökkenés nélküli szimulációk az adatokat nem reprodukálják.

6. Az η' és az η mezonok spektrumai a RHIC ütközéseiben

Meghatároztam a forró, sűrű közegben keletkező η és η' mezonok legvalószínűbb spektrumát. A szimmetria helyreállításának másik következménye ugyanis az η' és η mezonok spektrumának megváltozása a naiv várakozásokhoz képest. Amellett, hogy a reakcióban keletkező η' mezonok darabszáma megnövekszik, a spektrum alakja is megváltozik: az m_T -skálázást megtörő, kis impulzusú η' -k jelennek meg nagy számban [74, 75].

Acknowledgments

Here I would like to say thank you for all those without whom I could not have managed to write this PhD thesis.

On the first place my advisors Gábor Dávid and Tamás Csörgő. I got to know Gábor in Debrecen in 2003, and soon we started to work together. I got so much support from him, both personal and professional, and he taught me to collaborate in a large experiment. I met Tamás in BNL, and we began to work on a pion correlation topic when I applied to the RMKI a couple of months later. His knowledge and positive attitude proved to be a real treasure for me.

I must thank János Sziklai, my informal consultant whose wisdom helped a lot when I faced tough situations, and whose personality gave me a lot of inspiration.

I must also recognize the members of the PHENIX group, especially my closer colleagues Péter Tarján, József Imrek, Máté Csanád, Márton Nagy and Márton Vargyas (as for the Hungarian team), as well as Eduard Kistenev, Takao Sakaguchi and Kensuke Okada (from the Photon/EMCal groups). I could always count on Péter Raics, my project leader in Debrecen, a fantastic and helpful man.

I am also thankful to my RMKI colleagues. In particular to Dezső Horváth, the person who started me in the field of particle physics as my M.Sc. advisor and who also made a huge effort in reading and revising this thesis. To György Wolf and to Árpád Lukács for valuable discussions and advises.

I owe a thank to my old friends Gábor Orosz and Péter Biró together with Károly Makónyi and the local folks for their warm help and good advises regarding this thesis.

Last but not least I am the most grateful to my family: my wife Kata, my parents, and my sister Vera, who all supported me through all the (sometimes really difficult, sometimes just normal) times.

Bibliography

- [1] E. V. Shuryak, “Quantum chromodynamics and the theory of superdense matter”, Phys. Rept. **61**, 71 (1980).
- [2] K. Adcox *et al.* [PHENIX Collaboration], “Formation of dense partonic matter in relativistic nucleus-nucleus collisions at RHIC: Experimental evaluation by the PHENIX collaboration”, Nucl. Phys. A **757**, 184 (2005).
- [3] J. Adams *et al.* [STAR Collaboration], “Experimental and theoretical challenges in the search for the quark gluon plasma: The STAR Collaboration’s critical assessment of the evidence from RHIC collisions”, Nucl. Phys. A **757**, 102 (2005).
- [4] B. B. Back *et al.* [PHOBOS Collaboration], “The PHOBOS perspective on discoveries at RHIC”, Nucl. Phys. A **757**, 28 (2005).
- [5] I. Arsene *et al.* [BRAHMS Collaboration], “Quark gluon plasma and color glass condensate at RHIC? The Perspective from the BRAHMS experiment”, Nucl. Phys. A **757**, 1 (2005).
- [6] A. Adare *et al.* [PHENIX Collaboration], “Enhanced production of direct photons in Au+Au collisions at $\sqrt{s_{NN}} = 200$ GeV and implications for the initial temperature,” Phys. Rev. Lett. **104**, 132301 (2010).
- [7] K. Adcox *et al.* [PHENIX Collaboration], “Suppression of hadrons with large transverse momentum in central Au+Au collisions at $\sqrt{s_{NN}} = 130$ GeV”, Phys. Rev. Lett. **88**, 022301 (2002).
- [8] S. S. Adler *et al.* [PHENIX Collaboration], “Absence of suppression in particle production at large transverse momentum in $\sqrt{s_{nn}} = 200$ GeV d + Au collisions,” Phys. Rev. Lett. **91**, 072303 (2003).

-
- [9] “Future Science at the Relativistic Heavy Ion Collider”, BNL-77334-2006-IR (2006),
<http://www.bnl.gov/physics/rhicIIscience>.
- [10] A. Adare *et al.* [PHENIX Collaboration], “Detailed Measurement Of The e^+e^- Pair Continuum In p+p And Au+Au Collisions At $\sqrt{s_{nn}} = 200$ Gev And Implications For Direct Photon Production,” Phys. Rev. C **81**, 034911 (2010).
- [11] “‘Perfect’ Liquid Hot Enough to be Quark Soup – Protons, neutrons melt to produce ‘quark-gluon plasma’ at RHIC,” BNL News Release No. 10-1074, 2/15/2010.
- [12] K. Adcox *et al.* [PHENIX Collaboration], “PHENIX detector overview,” Nucl. Instrum. Meth. A **499** (2003) 469.
- [13] K. Ikematsu *et al.*, “A Start-Timing Detector for the Collider Experiment PHENIX at RHIC-BNL”, Nucl. Instr. and Meth. A **411** (1998) 238-248.
- [14] C. Adler *et al.*, “The RHIC zero degree calorimeters”, Nucl. Instr. and Meth. A. **470** (2001) 488.
- [15] M. Aizawa *et al.* [PHENIX Collaboration], “PHENIX central arm particle ID detectors”, Nucl. Instr. and Meth. A. **499** (2003) 508.
- [16] C. Amsler *et al.* [Particle Data Group], “Review of Particle Physics”, Phys. Lett. **B667**, 1 (2008) and 2009 partial update for the 2010 edition.
- [17] K. Adcox *et al.*, “Construction and performance of the PHENIX pad chambers”, Nucl. Instr. and Meth. A. **497** (2003) 263.
- [18] L. Aphecetche *et al.* [PHENIX Collaboration], “PHENIX calorimeter”, Nucl. Instr. and Meth. A. **499** (2003) 521.
- [19] Rene Brun *et al.*, “ROOT: An Object-Oriented Data Analysis Framework”, <http://root.cern.ch/>.
- [20] “EMCal Documentation and Tutorials (2000-2007),”
<http://www.phenix.bnl.gov/WWW/emcal/documentation>

- [21] P. Tarján, “Neutral Pion Production in High Energy Heavy Ion Collisions at the PHENIX Experiment”, Ph.D. thesis, University of Debrecen, 2010.
- [22] R. Vértési, G. Dávid, T. Csörgő “EMCal ToF Calibration and Slewing Effects in Year 5 Cu+Cu, Year 6 p+p and Year 7 Au+Au collisions”, PHENIX Technical Note 428, 2008/06/30.
- [23] X. N. Wang and M. Gyulassy, “HIJING: A Monte Carlo model for multiple jet production in p+p, p+A and A+A collisions”, Phys. Rev. D **44**, 3501 (1991).
- [24] E. Kistenev *et al.*, “PHENIX PbSc Electromagnetic Calorimeter: Results of Test Beam Studies”, Proceedings of the Fifth International Conference on Calorimetry in High Energy Physics World Scientific (1994) 211-223.
- [25] R. Vértési, G. Dávid, “Charge Veto and Antibaryon Cuts in the EMCal,” PHENIX Hadron Physics Working Group talk, 2004/02/27.
- [26] Genevieve Orr *et al.*, “Introduction to Neural Networks”, <http://www.willamette.edu/~gorr/classes/cs449/intro.html>.
- [27] J. Schwindling and B. Mansoulié, “MLPfit: a tool for Multi-Layer Perceptrons”, <http://schwind.web.cern.ch/schwind/MLPfit.html>.
- [28] H. Robbins and S. Monro, “A Stochastic Approximation Method”, Ann. Math. Statist. **22**, 400 (1951).
- [29] S. S. Adler *et al.* [PHENIX Collaboration], “Suppressed π^0 production at large transverse momentum in central Au+Au collisions at $\sqrt{s_{NN}} = 200$ GeV,” Phys. Rev. Lett. **91**, 072301 (2003).
- [30] A. Adare *et al.* [PHENIX Collaboration], “Onset of π^0 Suppression Studied in Cu+Cu Collisions at $\sqrt{s_{NN}} = 22.4, 62.4, \text{ and } 200$ GeV,” Phys. Rev. Lett. **101**, 162301 (2008).
- [31] A. Adare *et al.* [PHENIX Collaboration], “Suppression pattern of neutral pions at high transverse momentum in Au+Au collisions at $\sqrt{s_{NN}} = 200$ GeV and constraints on medium transport coefficients,” Phys. Rev. Lett. **101**, 232301 (2008).

-
- [32] S. S. Adler *et al.* [PHENIX Collaboration], “Common suppression pattern of η and π^0 mesons at high transverse momentum in Au+Au collisions at $\sqrt{s_{NN}} = 200$ GeV,” *Phys. Rev. Lett.* **96**, 202301 (2006).
- [33] G. Dávid, T. Sakaguchi, R. Vértési, “Simulation Verification in the EMCal PbSc Shower Characteristics of Hadrons,” PHENIX Analysis Note 330, 2004/10/11.
- [34] S. S. Adler *et al.* [PHENIX Collaboration], “Centrality dependence of direct photon production in $\sqrt{s_{NN}} = 200$ GeV Au + Au collisions,” *Phys. Rev. Lett.* **94**, 232301 (2005).
- [35] T. Peitzmann and M. H. Thoma, “Direct photons from relativistic heavy ion collisions,” *Phys. Rept.* **364**, 175 (2002).
- [36] G. Dávid for the PHENIX Collaboration, “Direct Photons at RHIC,” *34th International Conference on High Energy Physics, Philadelphia*, (2008), [arXiv:0810.0872](https://arxiv.org/abs/0810.0872) [nucl-ex].
- [37] T. Isobe, G. Dávid, T. Sakaguchi, B. Sahlmüller, H. Hamagaki, R. Vértési, J. Imrek, “Measurement of direct photon spectra with PbSc EMCal in $\sqrt{s_{NN}} = 200$ GeV Au+Au Collisions at Run4,” PHENIX Analysis Note 490, 2006/04/13.
- [38] G. Goldhaber, S. Goldhaber, W. Y. Lee and A. Pais, *Phys. Rev.* **120**, 300 (1960).
- [39] R. Hanbury Brown and R. Q. Twiss, “A Test Of A New Type Of Stellar Interferometer On Sirius”, *Nature* **178**, 1046 (1956).
- [40] S. Nickerson, T. Csörgő and D. Kiang, “Testing the core-halo model on Bose-Einstein correlation functions,” *Phys. Rev. C* **57**, 3251 (1998).
- [41] T. Csörgő, B. Lörstad and J. Zimányi, “Bose-Einstein correlations for systems with large halo,” *Z. Phys. C* **71**, 491 (1996).
- [42] J. Bolz, U. Ornik, M. Plumer, B. R. Schlei and R. M. Weiner, “Interferometry of pions and kaons in high-energy collisions,” *Phys. Lett. B* **300**, 404 (1993).

- [43] S. S. Adler *et al.* [PHENIX Collaboration], “Evidence for a long-range component in the pion emission source in Au + Au collisions at $\sqrt{s_{NN}} = 200$ -GeV,” *Phys. Rev. Lett.* **98**, 132301 (2007).
- [44] M. Sumbera [STAR Collaboration], “Selected results on strong and Coulomb-induced correlations from the STAR experiment,” *Braz. J. Phys.* **37**, 925 (2007).
- [45] C. Alt *et al.* [NA49 Collaboration], “Three-Dimensional two-pion source image from Pb+Pb Collisions at $\sqrt{s_{NN}} = 17.3$ GeV: New constraints for source breakup dynamics,” *Phys. Lett. B* **685**, 41 (2010).
- [46] S. E. Koonin, “Proton Pictures Of High-Energy Nuclear Collisions”, *Phys. Lett. B* **70**, 43 (1977).
- [47] A. Messiah, “Quantum Mechanics. Vol. 2”, De Gruyter, Berlin (1979).
- [48] E. O. Alt, T. Csörgő B. Lörstad and J. Schmidt-Sørensen, “Coulomb and core/halo corrections to Bose-Einstein N-particle correlations”, *Proceedings of Tihany 2000, From e+ e- to heavy ion collisions* 564-571.
- [49] D. A. Brown et al., “Imaging of sources in heavy ion reactions”, *Phys. Lett. B* **398**, 252 (1997).
- [50] M. Csanád, T. Csörgő, M. I. Nagy, R. Vértési, “Analyzing heavy tails in pion source function,” PHENIX Analysis Note 527, 2006/11/02.
- [51] R. Vértési for the PHENIX Collaboration, “THERMINATOR simulations and PHENIX images of a heavy tail of particle emission in 200 GeV Au+Au collisions,” *Proceedings of 23rd Winter Workshop on Nuclear Dynamics, Big Sky, Montana, USA* (EP Systema, Budapest, 2007).
- [52] S. Afanasiev *et al.* [PHENIX Collaboration], “Kaon interferometric probes of space-time evolution in Au+Au collisions at $\sqrt{s_{NN}} = 200$ GeV,” *Phys. Rev. Lett.* **103**, 142301 (2009).

-
- [53] T. J. Humanic, “Comparison of hadronic rescattering calculations of elliptic flow and HBT with measurements from RHIC,” Nucl. Phys. A **715**, 641 (2003).
- [54] T. J. Humanic, “Effects of non-causal artifacts in a hadronic rescattering model for RHIC collisions,” Phys. Rev. C **73**, 054902 (2006).
- [55] R. Metzler and J. Klafter, “The random walk’s guide to anomalous diffusion: a fractional dynamics approach,” Physics Reports **339**, 1-77.
- [56] M. Csanád, T. Csörgő and M. Nagy, “Anomalous diffusion of pions at RHIC,” Braz. J. Phys. **37**, 1002 (2007).
- [57] A. Kisiel, T. Taluc, W. Broniowski and W. Florkowski, Comput. Phys. Commun. **174**, 669 (2006).
- [58] W. Broniowski and W. Florkowski, “Explanation of the RHIC p_T -spectra in a thermal model with expansion,” Phys. Rev. Lett. **87**, 272302 (2001).
- [59] A. Baran, W. Broniowski and W. Florkowski, “Description of the particle ratios and transverse-momentum spectra for various centralities at RHIC in a single-freeze-out model,” Acta Phys. Polon. B **35**, 779 (2004).
- [60] P. Danielewicz, “Analysis of Emission Shapes,” *Proceedings of 23rd Winter Workshop on Nuclear Dynamics, Big Sky, Montana, USA* (EP Systema, Budapest, 2007).
- [61] S. Pratt, “Coherence and coulomb effects on pion interferometry,” Phys. Rev. D **33**, 72 (1986).
- [62] A. Bialas, “Intermittency and the Hanbury-Brown-Twiss effect,” Acta Phys. Polon. B **23**, 561 (1992).
- [63] W. Florkowski, W. Broniowski, A. Kisiel and J. Pluta, “Pion correlations in hydro-inspired models with resonances,” Acta Phys. Polon. B **37**, 3381 (2006).
- [64] T. Csörgő, “Particle interferometry from 40-MeV to 40-TeV,” Heavy Ion Phys. **15**, 1 (2002).

- [65] R. S. Hayano and T. Hatsuda, “Hadron properties in the nuclear medium,” arXiv:0812.1702 [nucl-ex].
- [66] M. Kobayashi and T. Maskawa, “Chiral symmetry and η -X mixing,” Prog. Theor. Phys. **44**, 1422 (1970).
- [67] G. ’t Hooft, “Computation of the quantum effects due to a four-dimensional pseudoparticle,” Phys. Rev. D **14**, 3432 (1976) [Erratum-ibid. D **18**, 2199 (1978)].
- [68] T. Kunihiro, “X Meson aka η' and Kobayashi-Maskawa-’t Hooft Six-quark Vertex – $U_A(1)$ Anomaly and Generalized Nambu-Jona-Lasinio Model –,” Prog. Theor. Phys. **122**, 255 (2009).
- [69] R. D. Pisarski and F. Wilczek, “Remarks On The Chiral Phase Transition In Chromodynamics,” Phys. Rev. D **29**, 338 (1984).
- [70] T. Kunihiro, “Effects Of The $U_A(1)$ Anomaly On The Quark Condensates And Meson Properties At Finite Temperature,” Phys. Lett. B **219**, 363 (1989).
- [71] J. I. Kapusta, D. Kharzeev and L. D. McLerran, “The Return Of The Prodigal Goldstone Boson,” Phys. Rev. D **53**, 5028 (1996).
- [72] Z. Z. Huang and X. N. Wang, “Partial U(1)A restoration and η enhancement in high-energy heavy ion collisions,” Phys. Rev. D **53**, 5034 (1996).
- [73] R. Vertesi, T. Csorgo and J. Sziklai, “Significant in-medium reduction of the mass of η' mesons in $\sqrt{s_{NN}} = 200$ GeV Au+Au collisions,” Nucl. Phys. A **830**, 631C (2009).
- [74] T. Csorgo, R. Vertesi and J. Sziklai, “Indirect observation of an in-medium η' mass reduction in $\sqrt{s_{NN}} = 200$ GeV Au+Au collisions,” Phys. Rev. Lett. **105**, 182301 (2010).
- [75] R. Vertesi, T. Csorgo and J. Sziklai, “Significant in-medium η' mass reduction in $\sqrt{s_{NN}} = 200$ GeV Au+Au collisions at RHIC,” e-print: [arXiv:0912.0258 [nucl-ex]] (Submitted to PRC).
- [76] J. Adams *et al.* [STAR Collaboration], “Pion interferometry in Au + Au collisions at $\sqrt{s_{NN}} = 200$ GeV,” Phys. Rev. C **71**, 044906 (2005).

-
- [77] S. S. Adler *et al.* [PHENIX Collaboration], “Bose-Einstein correlations of charged pion pairs in Au + Au collisions at $\sqrt{s_{NN}} = 200$ GeV,” *Phys. Rev. Lett.* **93**, 152302 (2004).
- [78] A. Marin *et al.* [CERES Collaboration], “Dilepton measurements with CERES,” *PoS C* **POD07**, 034 (2007).
- [79] E. Scomparin [NA60 Collaboration], “Dilepton measurements with NA60,” *PoS C* **POD07**, 033 (2007).
- [80] I. Tserruya, “Quark matter 2005: Experimental conference summary,” *Nucl. Phys. A* **774**, 415 (2006).
- [81] S. Afanasiev *et al.* [PHENIX Collaboration], “Enhancement of the dielectron continuum in $\sqrt{s_{NN}} = 200$ GeV Au+Au collisions,” e-print: [arXiv:0706.3034 [nucl-ex]].
- [82] A. Drees, “Dileptons and Photons at RHIC Energies,” *Nucl. Phys. A* **830**, 435C (2009)
- [83] S. E. Vance, T. Csörgő and D. Kharzeev, “Partial U(A)(1) restoration from Bose-Einstein correlations,” *Phys. Rev. Lett.* **81**, 2205 (1998).
- [84] B. Nilsson-Almqvist and E. Stenlund, “Interactions Between Hadrons And Nuclei: The Lund Monte Carlo, Fritiof Version 1.6,” *Comput. Phys. Commun.* **43**, 387 (1987).
- [85] T. Csörgő and S. Hegyi, “Model independent shape analysis of correlations in 1, 2 or 3 dimensions,” *Phys. Lett. B* **489**, 15 (2000).
- [86] H. C. Eggers and P. Lipa, “HBT shape analysis with q-cumulants,” *Braz. J. Phys.* **37**, 877 (2007).
- [87] M. Csanád [PHENIX Collaboration], “Measurement and analysis of two- and three-particle correlations,” *Nucl. Phys. A* **774**, 611 (2006) and the corresponding talk.
- [88] S. Hegyi and T. Csörgő, “Edgeworth expansion of Bose-Einstein correlation functions,” *Budapest 1992, Proceedings, Relativistic heavy ion collisions 47-51* (Preprint KFKI-1993-11/A).

- [89] Yu. Sinyukov, R. Lednicky, S. V. Akkelin, J. Pluta and B. Erasmus, “Coulomb corrections for interferometry analysis of expanding hadron systems,” *Phys. Lett. B* **432**, 248 (1998).
- [90] T. S. Biro, P. Levai and J. Zimanyi, “Alcor: A Dynamic Model For Hadronization,” *Phys. Lett. B* **347**, 6 (1995).
- [91] M. Kaneta and N. Xu, “Centrality dependence of chemical freeze-out in Au + Au collisions at RHIC,” e-print: [arXiv:nucl-th/0405068].
- [92] J. Letessier and J. Rafelski, “Hadron production and phase changes in relativistic heavy ion collisions,” *Eur. Phys. J. A* **35**, 221 (2008)
- [93] S. A. Bass *et al.*, “Last call for RHIC predictions,” *Nucl. Phys. A* **661**, 205 (1999)
- [94] M. Bleicher *et al.*, “Relativistic hadron hadron collisions in the ultra-relativistic quantum molecular dynamics model,” *J. Phys. G* **25**, 1859 (1999)
- [95] Z. W. Lin, C. M. Ko, B. A. Li, B. Zhang and S. Pal, “A multi-phase transport model for relativistic heavy ion collisions,” *Phys. Rev. C* **72**, 064901 (2005).
- [96] S. S. Adler *et al.* [PHENIX Collaboration], “Identified charged particle spectra and yields in Au + Au collisions at $\sqrt{s_{NN}} = 200$ GeV,” *Phys. Rev. C* **69**, 034909 (2004)
- [97] T. Csörgő and B. Lörstad, “Bose-Einstein Correlations for Three-Dimensionally Expanding, Cylindrically Symmetric, Finite Systems,” *Phys. Rev. C* **54**, 1390 (1996).
- [98] T. Sjostrand, “Pythia 5.7 And Jetset 7.4: Physics And Manual,” arXiv:hep-ph/9508391.
- [99] P. Lévai, “Strange hadron ratios from quark coalescence at RHIC and LHC”, *J. Phys. G* **35**, 044041 (2008).
- [100] S. Weinberg, “The U(1) Problem,” *Phys. Rev. D* **11**, 3583 (1975).

Acronyms

ADC	analog–digital converter
ANN	artificial neural network
BBC	Beam–Beam Counter
BEC	Bose–Einstein correlation
BNL	Brookhaven National Laboratory
EMCal	Electromagnetic Calorimeter
FEM	front–end electronics module
HBT	Hanbury Brown–Twiss
HPSS	High Performance Storage System
HRC	Hadron Rescattering Code
MIP	minimum ionizing particle
PbGl	lead glass
PbSc	lead scintillator
PHENIX	Pioneering High Energy Nuclear Interaction eXperiment
PID	particle identification
PMT	photomultiplier tube
pQCD	perturbative QCD
RHIC	Relativistic Heavy Ion Collider
QCD	quantum chromodynamics
QGP	quark–gluon plasma
sQGP	strongly interacting quark–gluon plasma
STAR	Solenoid Tracker At RHIC
TDC	time–digital converter
ToF	time of flight
ZDC	Zero Degree Calorimeter